

High-resolution observations
of the solar
photosphere and chromosphere



DISSERTATION
zur
Erlangung des Doktorgrades
der
Fakultät für Mathematik und Physik
der
Albert-Ludwigs-Universität Freiburg

vorgelegt von

Friedrich Wöger

aus
Köln
2006

Dekan: Prof. Dr. Jörg Flum
Referent: Prof. Dr. Oskar von der Lühe
Koreferent: Prof. Dr. Gregor Herten
Tag der mündlichen Prüfung: 7. März 2007

In the context of this thesis the following articles have been published:

Refereed Journals

- Wöger, F., Wedemeyer-Böhm, S., Schmidt, W., and von der Lüche, O., 2006:
Observation of a short-lived pattern in the solar chromosphere,
Astronomy & Astrophysics, 459, L9–L12

Conference proceedings and other publications

- Reardon, K., Casini, R., Cavallini, F., Tomczyk, S., Rouppe van der Voort, L., Van Noort, M., Woeger, F., Socas Navarro, H. and IBIS Team, 2006:
High Resolution Spectropolarimetry of Penumbra Formation with IBIS,
AAS/Solar Physics Division Meeting
- Wöger, F., Wedemeyer-Böhm, S., Schmidt, W., von der Lüche, O., 2005:
High resolution time series of narrowband Ca II K image in the chromosphere,
ASP Conference Series, accepted
- Wöger, F., Berkefeld, T., Soltau, D., 2003:
Comparison of Methods for Fried Parameter Estimation,
Astronomische Nachrichten, Astronomical Notes, Supplementary Issue, Vol. 324, 22.
- Mikurda, K.; von der Lüche, O.; Wöger, F., 2003:
Solar Imaging with an Extended Knox-Thompson Technique,
Astronomische Nachrichten, Astronomical Notes, Supplementary Issue, Vol. 324, 112.

Abstract

Observations of the sun are almost always impaired by the turbulent motion of air in Earth's atmosphere. The turbulence would limit the theoretical resolution of modern large telescopes to that of amateur telescopes without additional tools. Today however, high-resolution data of the Sun are necessary to investigate its small-scale structure. This structure is likely to be connected to the radially outward increasing temperature distribution of the solar atmosphere.

An introduction into further details of this topic that has also been the motivation for this work is presented in Chapt. 1. A theory of atmospheric turbulence that builds the basis for several results of this work is described in Chapt. 2. Here, two modern tools to enhance the resolution of ground based observations are reviewed, on the one hand adaptive optics (AO) systems and on the other hand speckle interferometry. Until recently, these two techniques were only used separately. In Chapt. 3 the necessary modifications for analytical models of transfer functions are developed that include the changes made by an AO system to the incoming wave front, thus making a combination of AO systems and speckle interferometry possible. The models were compared to measured data using different techniques, and a good agreement was found. In order to apply speckle interferometry to the observational data acquired for this work, a computer program package was developed that can reduce vast amount of data within a reasonable time in a parallel way (App. A).

Speckle interferometry needs very shortly exposed data in order to compute a reconstruction. However, a part of the data observed for this work had to be exposed rather long because of technical problems, making the use of this reconstruction technique impossible. This motivated the development of an algorithm to estimate instantaneous point spread functions from speckle reconstructions. The point spread functions permit the deconvolution of the long exposed data making use of well known techniques. The algorithm is developed in Chapt. 4, along with a presentation of an examination of usability.

In Chapt. 5 the observational data that were reduced using the algorithms developed in the course of this work were analyzed. It was found that bright points within the chromospheric network are correlated both spatially and temporally to those in the photospheric network. The phenomena appear to overlay

almost vertically. The ratio of their radii is $\langle R_{\text{chrom. BP}}/R_{\text{phot. BP}} \rangle = 3.0$ with a standard deviation of 0.7. The analysis of life times of structures within the chromosphere revealed that network and inter-network regions can be separated more accurately using a life time rather than the commonly used intensity criterion. The combination of high spectral and spatial resolution within this dataset revealed the existence of an up to now undetected pattern of granular size in the chromospheric inter-network that evolves too rapidly (with time scales of ≈ 53 s) to be reversed granulation. This finding supports recent models of the non-magnetic solar chromosphere that could explain this pattern as signature of propagating and interacting shock waves that are excited in the photosphere as an acoustic phenomenon. This is supported by the detailed investigation of the solar oscillations in the chromospheric network and inter-network that shows that the main contributions to the 3 min oscillations in the chromosphere can be attributed to the inter-network. The chromospheric network mainly contributes to 5 min oscillations, which are typical for the photosphere.

Zusammenfassung

Beobachtungen der Sonne werden fast immer durch die turbulenten Luftbewegungen in der Erdatmosphäre beeinträchtigt, welche die theoretische Auflösung moderner Großteleskope ohne weitere Hilfsmittel auf die von Amateurteleskopen beschränken würde. Heutzutage jedoch sind hoch auflösende Daten der Sonne nötig, um die kleinskaligen Strukturen zu untersuchen, welche wahrscheinlich ursächlich für den nach außen hin ansteigenden radialen Temperaturverlauf in der Sonnenatmosphäre sind.

Eine Einführung in weitere Details dieser Thematik, welche auch die Motivation für diese Arbeit war, wird in Kapitel 1 gegeben. Eine Theorie der atmosphärischen Turbulenz, welche die Grundlage für verschiedene Ergebnisse dieser Arbeit bildet, wird in Kapitel 2 dargestellt. Hier werden auch zwei moderne Hilfsmittel zur Verbesserung der Auflösung von erdgebundenen Beobachtungen besprochen, einerseits adaptive Optik (AO) und andererseits Speckle Interferometrie. Bis vor kurzem wurden diese Techniken lediglich separat verwendet. In Kapitel 3 werden die notwendigen Modifikationen für analytische Modelle von Transferfunktionen erarbeitet, welche die Änderungen einer einfallenden Wellenfront durch eine beliebig gut korrigierende AO berücksichtigen und somit eine Kombination von AO und Speckle Interferometrie ermöglichen. Die Modelle wurden auf unterschiedliche Weisen mit gemessenen Daten verglichen, und eine gute Übereinstimmung konnte festgestellt werden. Zur Anwendung der Speckle Interferometrie auf die für diese Arbeit beobachteten Daten wurde ein Programmpaket entwickelt, welches die anfallenden großen Datenmengen innerhalb kurzer Zeit parallel verarbeitet (Anhang A).

Speckle Interferometrie benötigt sehr kurz belichtete Daten für eine Rekonstruktion. Bei den für diese Arbeit notwendigen Sonnenbeobachtungen musste jedoch aus technischen Gründen ein Teil der Daten zu lang belichtet werden, um sie mit dieser Technik verarbeiten zu können. Dies motivierte die Entwicklung eines Algorithmus, mit dessen Hilfe aus einer Speckle Rekonstruktion instantane Punktverbreiterungsfunktionen geschätzt werden können, welche die nachträgliche Entfaltung der zu lang belichteten Bilddaten mit bekannten Techniken ermöglichen. Der Algorithmus sowie dessen Überprüfung und Anwendbarkeit wird in Kapitel 4 beschrieben.

In Kapitel 5 wurden die mit den in dieser Arbeit entwickelten Algorithmen verarbeiteten Daten analysiert. Dabei ergab sich, dass Bright Points im chromosphärischen Netzwerk räumlich und zeitlich stark mit solchen im photosphärischen Netzwerk korreliert sind, und diese beiden Phänomene fast vertikal übereinanderliegen. Eine Vermessung zeigte, dass das Größenverhältnis ihrer Radien $\langle R_{\text{chrom. BP}}/R_{\text{phot. BP}} \rangle = 3.0$ beträgt, mit einer Standardabweichung von 0.7. Bei der Analyse der auftretenden Lebenszeiten von Strukturen in der Chromosphäre ergab sich, dass eine Trennung von Netzwerk und Inter-Netzwerk basierend auf einem Zeitkriterium genauer ist als, wie bislang üblich, die Verwendung eines Intensitätskriteriums. Aufgrund der Kombination von hoher räumlicher und spektraler Auflösung der verarbeiteten Beobachtungsdaten stellte sich heraus, dass im Inter-Netzwerk der Chromosphäre ein bislang unentdecktes Muster existiert, welches sich sehr schnell entwickelt (mit Zeitskalen von ≈ 53 s) und von granularer Größe ist, und bei welchem es sich nicht um inverse Granulation handelt. Dies passt zu neueren Modellen der nicht-magnetischen solaren Chromosphäre, welches das Muster als die Signatur von propagierenden und sich überlagernden Schockwellen beschreibt, welche in der Photosphäre akustisch angeregt werden. Dies wird durch die differenzierte Untersuchung der solaren Oszillationen im Netzwerk und Inter-Netzwerk unterstützt, welche zeigt, dass die Hauptbeiträge zu den chromosphärischen 3 min Oszillationen dem Inter-Netzwerk zuzuordnen sind; das chromosphärische Netzwerk weist hauptsächlich Beiträge zu Oszillationen mit Perioden von 5 min auf, welche eher der Photosphäre zuzuordnen sind.

Contents

| | | |
|----------|---|-----------|
| 1 | Introduction | 1 |
| 2 | High-resolution techniques for solar observations | 7 |
| 2.1 | The theory of incoherent imaging systems | 8 |
| 2.2 | The turbulence of the atmosphere | 11 |
| 2.2.1 | The Kolmogorov theory of turbulence | 11 |
| 2.2.2 | The influence on an optical system | 12 |
| 2.3 | Adaptive optics | 14 |
| 2.4 | Speckle interferometry | 18 |
| 2.4.1 | Amplitude reconstruction | 19 |
| 2.4.1.1 | The Labeyrie method | 19 |
| 2.4.1.2 | Atmospheric transfer functions | 21 |
| 2.4.2 | Fried parameter estimation | 22 |
| 2.4.3 | Phase reconstruction | 23 |
| 2.4.3.1 | Extended Knox-Thompson | 24 |
| 2.4.3.2 | Triple correlation | 26 |
| 2.5 | Conclusion | 27 |
| 3 | Speckle interferometry using adaptive optics corrected data | 29 |
| 3.1 | Long exposure transfer function of an arbitrary adaptive optics system | 30 |
| 3.2 | Speckle transfer function of an arbitrary adaptive optics system . | 33 |
| 3.3 | Field dependency | 36 |
| 3.4 | Algorithm for the integration of the transfer functions | 37 |
| 3.5 | Results | 38 |

CONTENTS

| | | |
|----------|--|------------|
| 3.5.1 | Computational results | 38 |
| 3.5.2 | Comparison to observed transfer functions | 43 |
| 3.5.3 | Speckle imaging of solar data | 44 |
| 3.6 | Conclusions | 45 |
| 4 | PSF reconstruction and image deconvolution | 49 |
| 4.1 | Reconstruction of the PSF from a speckle reconstruction | 50 |
| 4.1.1 | Tests on simulated data | 52 |
| 4.2 | Deconvolution using the maximum entropy method | 54 |
| 4.3 | Application to observational data | 58 |
| 4.4 | Conclusions | 61 |
| 5 | The connection of photosphere and chromosphere | 63 |
| 5.1 | Introduction | 63 |
| 5.2 | Fine structure in the photosphere | 65 |
| 5.3 | Fine structure in the chromosphere | 68 |
| 5.4 | Observations and data reduction | 70 |
| 5.5 | Data analysis | 72 |
| 5.5.1 | Separation of network and inter-network | 72 |
| 5.5.2 | Morphology | 75 |
| 5.5.2.1 | Separation and analysis of G-band and CaIIK network bright points | 75 |
| 5.5.2.2 | Short-lived pattern in the inter-network | 79 |
| 5.5.3 | Oscillations | 83 |
| 5.5.4 | Correlation with the photosphere | 87 |
| 5.5.4.1 | Distance between maxima in intensity | 88 |
| 5.5.4.2 | Individual case 1: network fine-structure | 91 |
| 5.5.4.3 | Individual case 2: inter-network fine-structure | 91 |
| 5.6 | Conclusion | 96 |
| 6 | Conclusions | 99 |
| | Nomenclature | 104 |

CONTENTS

| | | |
|----------|--|------------|
| A | Code comparison and performance | 105 |
| A.1 | Parallelization | 106 |
| A.2 | Convergence properties | 106 |
| A.2.1 | Code performance | 110 |
| B | Zernike polynomials | 113 |
| | References | 124 |

CONTENTS

Chapter 1

Introduction

Up to today, our Sun poses many riddles to us, even though it is an average star consisting of hydrogen ($\sim 73\%$) and helium ($\sim 25\%$) mainly. On a closer look, far from being homogeneous, it shows a lot of activity within different layers (see Fig. 1.1). In the core of the Sun, energy is produced via nuclear fusion processes that transform hydrogen to helium. Within the radiation zone, this energy is transferred merely by radiation outwards up to the convection zone. In this layer, the energy is transported via convective motion of material. This movement sets in because the temperature gradient induced by the heat input at the bottom of the convection zone and the cooling at the photosphere causes a density stratification, with lower densities at the bottom than at the surface. This leads to an unstable situation because of buoyancy forces due to Sun's gravitation, and a perturbation leads to thermal convection. The layers of the solar atmosphere are photosphere, chromosphere and corona. The photosphere is the easiest to observe: it emits the vast majority of the light. The geometrically higher chromosphere and corona are a little bit more difficult to be detected, as their emission at wavelengths visible to the human eye is much less intense than that of the photosphere. In fact, they were detected first during solar eclipses, where the bright solar disc was obscured by the Moon. A detailed look at single isolated layers can further the knowledge by reducing the complexity of the modeling problem to a certain degree. While there has been much progress in the understanding and modeling of the photosphere, other layers are hardly understood, partly because observations of these layers are very difficult (like those

1. INTRODUCTION

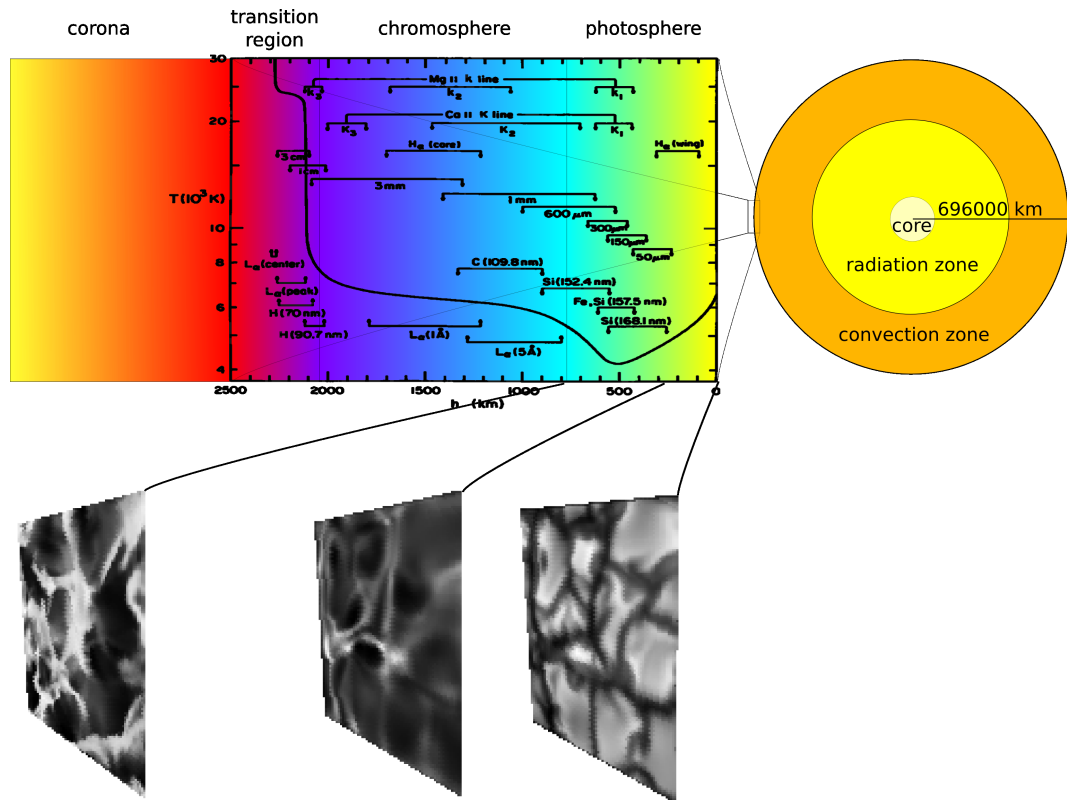


Figure 1.1: The Sun is usually divided into layers: core, radiation zone, convection zone, photosphere, chromosphere and corona. The temperature distribution in the last three layers is indicated as the solid curve in the plot (height increasing from right to left, after [Vernazza et al. \(1981\)](#)). The images below show modeled intensities at the indicated heights (courtesy of S. Wedemeyer-Böhm).

below the visual 'surface' of the Sun, e.g. the convection zone) and partly because the numerical modeling is simply impossible when trying to consider all relevant properties (as is the case for the chromosphere and corona). Ultimately, one cannot neglect the influence of the layers on each other, making full three-dimensional models absolutely necessary to understand and predict the behavior of solar activity.

One of the biggest mysteries in solar physics is the temperature stratification of the solar atmosphere with height; it has been known for a long time from the emission in chromospheric and coronal spectral lines, that indeed these two layers are much *hotter* than the photosphere, the geometrically underlying 'surface' of the Sun. In order to understand this behavior, the mechanisms for energy generation (photosphere), transport (chromosphere and transition region) and dissipation (corona) need to be explained. While it is clear, that the source of the energy must be magneto-convection and flux emergence, the physical processes which are involved in the transport are still largely unknown (e.g. [Marsch, 2006](#)).

The work of [Vernazza *et al.* \(1981\)](#), for example, establishes a semi-empirical one-dimensional temperature model for a static solar atmosphere. It shows that the temperature at the continuum photosphere is the well known black-body temperature of 5778 K and then first drops with height until it reaches a minimum at roughly 500 km. The following temperature increase steepens throughout the chromosphere; the temperature finally reaches 10^6 K in the corona (see graph in [Fig. 1.1](#)). What could be an explanation for this behavior?

The research of this question has focused on the small-scale structure in the photosphere and chromosphere in recent years. When observing the Sun from Earth, however, the small scale structure of these regions is seldom detected well, even though the telescopes theoretically have a diameter big enough to resolve structures of less than 100 km in size on the Sun. The reason is Earth's turbulent atmosphere that degrades the image quality. This has been known for a long time (Sir Isaac Newton was already aware of this fact). The first solution that comes to mind, space telescopes, are not always an option because of the high expenses and their inflexibility. In the last century much effort and research has been invested to find ways for ground-based telescopes to overcome the effects of the atmosphere. Several of them have been proved to be powerful and are being

1. INTRODUCTION

used at telescopes throughout the world, like adaptive optics systems that reduce the effects in-situ or post-facto image reconstruction techniques.

This thesis is related to the question of morphology and dynamical behavior of the small scale structure seen in photosphere and chromosphere, and whether there is a close connection between them. An answer to these questions could help to understand the physical processes behind the energy transport upwards to the corona. In order to be able to resolve the relevant structures in spite of Earth's atmosphere, a computer package for post-facto reconstruction of images was to be written for parallel processing in order to handle the necessary large amount of data within a short time. Furthermore, the computer program had to take into account the influence of an adaptive optics system on measurements, because such a system was used during the observations which were carried out for this thesis. This made a modification of models for the atmospheric transfer functions necessary because these are used during the reconstruction process. However, it was clear that an important part of the dataset could not be processed by this program because they would not fulfill the condition of being shortly exposed, which means exposure times of about 10 ms and less. For this data, an algorithm was to be developed that allows a reconstruction of such data using deconvolution algorithms.

In Chapt. 2, a short introduction to the theory behind adaptive optics and speckle interferometry is presented. Chapter 2 also builds the basis for Chapt. 3, which makes the combination of adaptive optics and speckle interferometry possible through a modification of analytical models for the transfer functions that are used for the speckle reconstruction process. In Chapt. 4, a new algorithm for the estimation of the point spread function, a function that describes an optical system, is presented. This algorithm eventually allows the reconstruction of data using deconvolution algorithms. Chapter 5 presents the observed data which was processed using the algorithms described throughout this work in order to reach the highest possible resolution. In this section the data was analyzed with respect to the morphology, dynamics and correlation of the fine structure encountered in photosphere and chromosphere. The last Chapt. 6 draws conclusions and gives a small outlook on future work to be done. An analysis of the performance of

the image reconstruction package, which is based on speckle interferometry and which was written in the course of this work, can be found in [App. A](#).

1. INTRODUCTION

Chapter 2

High-resolution techniques for solar observations

When looking at an object in the sky with a large earthbound telescope, the observer soon realizes that the theoretical spatial resolution of the instrument is almost never reached. The reason is the turbulent motion of air in the atmosphere. The Reynolds number, which provides a criterion to determine whether a flow is turbulent or not, is approximately

$$\text{Re} = \frac{v_{\text{avg}} \cdot l}{\nu} \approx 10^5, \quad (2.1)$$

using an average velocity $v_{\text{avg}} = 1$ m/s, a characteristic size for an eddy in motion of $l = 10$ m and the kinematic viscosity of air $\nu = 1.5 \times 10^{-5}$ m²/s. The Reynolds number is high enough to ensure that the flow is turbulent in the vast majority of cases (Roggemann *et al.*, 1997, and references therein), causing random variations of the index of refraction. Just before a light wave of a distant object impinges the atmosphere, it has a planar surface of constant phase, also called *wavefront*. While passing Earth's atmosphere, the wavefront is corrugated by random variation of the optical path length which is caused by local, turbulence induced changes of the index of refraction. The physical consequence of the nonplanarity of the wave entering the telescope is an optical aberration in the focal plane that degrades the spatial resolution.

Several approaches have been made to reduce the atmospheric effects. Space

2. HIGH-RESOLUTION TECHNIQUES FOR SOLAR OBSERVATIONS

bound observations are most favorable, but also most expensive and inflexible in setup. Most of the modern ground-based telescopes use adaptive optics (AO) systems. These optical systems measure the wavefront corrugation in-situ and try to compensate it in real time by means of a phase correcting device. In most cases, this device is an adaptive mirror that takes on the inverse form of the corrugation. Additionally, post-facto image reconstruction techniques have been developed that restore the image of the object by means of algorithms that estimate the atmospheric turbulence.

In this Chapter, the physical theory of the atmospheric motion and its influence on an optical system is briefly discussed (Sect. 2.1 and 2.2). This is necessary to understand the principles behind an AO system (Sect. 2.3) and the post-facto image reconstruction procedure focused on in this work, speckle reconstruction (Sect. 2.4). Furthermore, the theory is used extensively in Chapt. 3.

2.1 The theory of incoherent imaging systems

The propagation of light through (turbulent) media and diffracting optics in telescopes can be described by a scalar diffraction theory, since the observed wavelengths are mostly much smaller than the aperture of the telescope and the observational plane is many wavelengths away from the diffracting plane (Roggemann, 1996). Light waves whose propagation direction is parallel to the viewing direction of the telescope are called *on-axis*, all others *off-axis* (see Fig. 2.1). If the source of the light is spatially incoherent, which is the case for thermal emitters like the Sun and stars in general, the combination of atmosphere and telescope can be described as linear system. In this case, the *on-axis* signal response in the focal plane, i.e. on the detector, is the convolution of the true source intensity and a function describing the response of the optical system to an incoming impulse (in optics commonly referred to as point spread function, PSF). The Fourier transform of the PSF, the optical transfer function (OTF), is generally a complex quantity. Like the PSF, the OTF describes the system completely. It depends on the pupil function $W(\vec{r})$, which, in the simplest case of a telescope without any

2.1 The theory of incoherent imaging systems

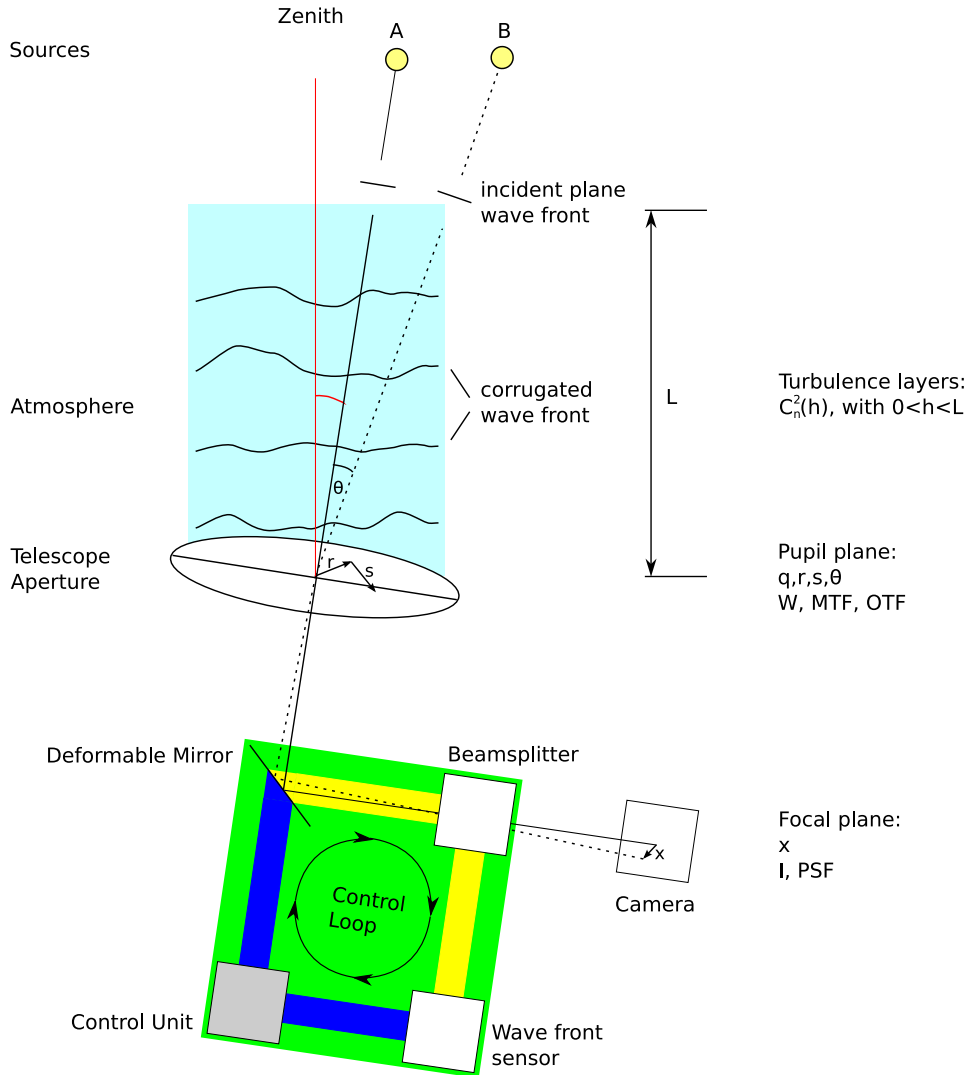


Figure 2.1: A sketch of the geometry and variables used throughout this work (lengths are not in scale). On-axis light (from source A) travels along the solid line, whereas off-axis light (from source B) travels along the dashed line. An incident plane wave front gets corrugated while traveling through several turbulent layers in the atmosphere (blue). The light enters the telescope in the pupil plane and is detected in the focal plane. The red arc designates the zenith distance ζ . An Adaptive Optics system (green) can be used to correct the wave front (see Sect. 2.3).

2. HIGH-RESOLUTION TECHNIQUES FOR SOLAR OBSERVATIONS

aberrations, is

$$W(\vec{r}) = \begin{cases} \frac{1}{\pi} & \text{if } |\vec{r}| \leq D/2 \\ 0 & \text{if } |\vec{r}| > D/2 \end{cases}, \quad (2.2)$$

where D is the diameter of the aperture and \vec{r} is a position in the pupil plane. In general, $W(\vec{r})$ is complex. The OTF is the autocorrelation of the pupil function

$$\text{OTF}(\vec{s}) = \int d\vec{r} W(\vec{r} - \frac{1}{2}\vec{s})W^*(\vec{r} + \frac{1}{2}\vec{s}), \quad (2.3)$$

where $*$ denotes complex conjugation. Thus the optical system can be described by $W(\vec{r})$ or either one of the functions PSF and OTF. As long as the PSF does not depend on a particular viewing angle (isoplanatic conditions), the intensity I at any position \vec{x} (*on- and off-axis*) on the detector can be obtained by

$$I(\vec{x}) = (O \otimes \text{PSF})(\vec{x}), \quad (2.4)$$

where \otimes indicates the convolution of object O with PSF . The convolution theorem states that in the Fourier domain

$$\tilde{I}(\vec{s}) = \tilde{O}(\vec{s}) \cdot \text{OTF}(\vec{s}). \quad (2.5)$$

The coordinate \vec{s} is related to the conjugated coordinate of \vec{x} , the spatial frequency \vec{f} , $[\vec{f}] = \text{m}^{-1}$, in the following way:

Let $f_c = D/(\lambda f_e)$ denote the theoretical cutoff frequency of the telescope in m^{-1} , where f_e is its effective focal length and λ is the observed wavelength. In the rest of this thesis, it will be assumed without loss of generality that $f_e = 1$. Then the normalized coordinate \vec{q} is defined as

$$\vec{q} = \vec{f}/f_c, \quad \text{with } 0 < |\vec{q}| < 1. \quad (2.6)$$

The coordinate \vec{s} can then be defined by

$$\vec{s} = \vec{q} \cdot D. \quad (2.7)$$

This definition simplifies the calculations later on. From now on, the variable \vec{x} will be used as coordinate in the focal plane, whereas \vec{r} , \vec{s} and \vec{q} are always

related to coordinates in the pupil plane, unless otherwise denoted (see Fig. 2.1).

2.2 The turbulence of the atmosphere

2.2.1 The Kolmogorov theory of turbulence

The Kolmogorov theory of turbulence is based on the assumption that the kinetic energy of a turbulent flow is transferred from large spatial scales (L_0 , outer scale) to smaller ones (l_0 , inner scale), and is homogeneous and isotropic at the small spatial scales. The inner scale is the limit where the Reynolds number falls below some critical value, the flow stops its turbulent movement and the kinetic energy dissipates into heat. While l_0 for air in the atmosphere is of the size of millimeters, L_0 is highly variable. There is some evidence that it is at least several meters, but it can reach several hundred meters (Roggemann *et al.*, 1997). The following calculations are true for the inertial subrange, the regime of

$$1/L_0 < \kappa < 1/l_0, \text{ with } \kappa = 2\pi/l, \quad (2.8)$$

only. In a stationary state the rate of energy input (through wind or radiation) needs to be equal to the dissipated energy. This implies that velocity fluctuations at any spatial scale may only depend on the spatial scale l and energy transport rate per unit mass ϵ . In one dimension, through a dimensional analysis ($[\epsilon] = \text{N m}/(\text{s kg})$), this leads to

$$v \propto \epsilon^{1/3} \cdot \kappa^{-1/3}. \quad (2.9)$$

Considering that kinetic energy is proportional to v^2 , the total energy in the interval $[\kappa, \kappa + d\kappa]$ can be obtained by squaring equation (2.9) and integrating the result:

$$\Phi(\kappa)d\kappa \propto \kappa^{-2/3} \rightarrow \Phi(\kappa) \propto \kappa^{-5/3}. \quad (2.10)$$

$\Phi(\kappa)$ is the spatial power spectrum of energy fluctuations for one dimension. The extension of the one dimensional case to three dimensions in the homogeneous and isotropic case is given by

$$\Phi(\kappa) = 4\pi\kappa^2\Phi(\vec{\kappa}) \rightarrow \Phi(\vec{\kappa}) \propto \kappa^{-11/3}. \quad (2.11)$$

2. HIGH-RESOLUTION TECHNIQUES FOR SOLAR OBSERVATIONS

The details of this calculation as well as constant of proportionality can be found in [Tatarskii \(1971\)](#).

2.2.2 The influence on an optical system

The influence of the atmosphere on the imaging quality of an optical system originate from inhomogeneities of the index of refraction due to temperature fluctuations. Pressure fluctuations are equalized with the speed of sound and thus can be neglected. "Conservative passive additives", i.e. physical quantities of the air that do not change the dynamics of the turbulence (like temperature¹ and thus the refractive index) behave statistically in the same way as the velocities ([Tatarskii, 1971](#), pp. 59-67). This is expressed in

$$\Phi_n(\kappa) = 0.033C_n^2(h)\kappa^{-11/3} \quad (2.12)$$

where $\Phi_n(\kappa)$ is the Kolmogorov spectrum of the index of refraction ([Tatarskii, 1971](#), pp. 74-76). The quantity $C_n^2(h)$ is called refractive index structure constant and is – despite of its misleading name – quite variable, especially with height above the telescope h . $C_n^2(h)$ characterizes the strength of the refractive-index fluctuations. It depends strongly on the geographical location and also varies from day to night ([Roggemann, 1996](#)).

It is convenient to introduce the structure function $\mathcal{D}_n^{h=z_0}(\vec{r})$ of the index of refraction at height z_0 :

$$\mathcal{D}_n^{h=z_0}(\vec{r}) = \langle |n(\vec{r}_1) - n(\vec{r}_1 + \vec{r})|^2 \rangle \quad (2.13)$$

$$= 2[\mathcal{Cov}_n(0) - \mathcal{Cov}_n(\vec{r})] \quad (2.14)$$

where $\langle \cdot \rangle$ is the notation for the statistical expectation operator and \mathcal{Cov}_n is the covariance of $n(\vec{r})$ at height z_0 . As long as $|\vec{r}|$ is not excessively large, the structure function of a non stationary random field neglects large scale inhomogeneities which are not interesting in this context. This is in contrast to the correlation function which is sensitive to inhomogeneities of all scales.

¹Buoyancy can be neglected.

2.2 The turbulence of the atmosphere

$\mathcal{C}ov_n(\vec{r})$ and power spectral density $\Phi_n(\vec{r})$ both build a Fourier pair (Goodman, 1985). With equation (2.14) it can thus be shown that

$$\mathcal{D}_n^{h=z_0}(\vec{r}) = 2 \int d\vec{\kappa} [1 - \cos(\vec{\kappa} \cdot \vec{r})] \Phi_n(\vec{\kappa}) = C_n^2(h) r^{2/3}, \quad (2.15)$$

for regions where $C_n^2(h)$ is constant.

A refractive-index fluctuation $n(\vec{r}, z)$ in a thin turbulence layer of thickness δz would translate into a phase variation of the plane wavefront via $\varphi(\vec{r}) = k \int_{z_0}^{z_0+\delta z} dz n(\vec{r}, z)$, where $k = 2\pi/\lambda$ is the wave number. From this, it is clear that the structure function of index of refraction and phase structure function must be tied closely together. Integrating equation (2.15) over all fluctuations in the atmosphere along the line-of-sight yields $\mathcal{D}_\varphi(\vec{r})$, the structure function for the phase of the wavefront. The derivation has been reported first in Fried (1966) and was restated many times with the result of (here after Roddier (1981))

$$\begin{aligned} \mathcal{D}_\varphi(\vec{r}) &= \langle |\varphi(\vec{r}_0) - \varphi(\vec{r}_0 + \vec{r})|^2 \rangle \\ &= 2 \left[\frac{24}{5} \Gamma\left(\frac{6}{5}\right) \right]^{5/6} \left(\frac{|\vec{r}|}{r_0} \right)^{5/3} \approx 6.88 \left(\frac{|\vec{r}|}{r_0} \right)^{5/3} \end{aligned} \quad (2.16)$$

where

$$r_0 = \left[0.423 k^2 \sec(\zeta) \int dh C_n^2(h) \right]^{-3/5} \quad (2.17)$$

Here, ζ is the zenith distance (see Fig. 2.1). The quantity r_0 is called Fried parameter and is the spatial coherence length of the atmosphere. It can be interpreted as the maximum diameter of a telescope that would still deliver diffraction limited data under the given atmospheric conditions. In other words, the atmosphere reduces the resolution of a telescope with diameter D from λ/D to λ/r_0 , if $r_0 < D$ which is almost always the case for big telescopes.

r_0 is proportional to $k^{-6/5}$ and thus $\lambda^{6/5}$, indicating that observations in the near infrared are not as much affected by the atmosphere as those in the UV. From r_0 one can quite easily calculate the correlation time in the atmosphere under the assumption of the validity of *Taylor's frozen-flow hypothesis* which states that over short time intervals the index of refraction fluctuation remains

2. HIGH-RESOLUTION TECHNIQUES FOR SOLAR OBSERVATIONS

fixed except for translation with uniform transverse (wind-)velocity \vec{v} . For typical values of $|\vec{v}| = 10$ m/s and $r_0 = 10$ cm (at $\lambda = 500$ nm) one gets a correlation time of $\tau_0 = r_0/|\vec{v}| = 10$ ms. In the future, "short exposed" is used in the sense that the exposure time of the image is about or less than the correlation time of the atmosphere, and is capable of freezing a realization of the atmospheric turbulence. The term "long exposed" will indicate that the exposure time was much longer than τ_0 , which leads to a greatly reduced resolution in the image.

The atmosphere also introduces amplitude variations of the electromagnetic wave $\Psi(\vec{r}) = \Psi_0(\vec{r}) \exp(i\phi(\vec{r})) = \exp(l(\vec{r}) + i\phi(\vec{r}))$, where $l(\vec{r})$ is called the log-amplitude and can be treated very similar to the phase. The effect in the focal plane caused by amplitude variations, called scintillation, is the more obvious the smaller the aperture of the imaging system; looking at the sky at night with the naked eye, scintillation causes the twinkle of the stars. For modern telescopes with apertures larger than 50cm, one can assume that the *near field* approximation holds true, i.e.

$$D^2 \gg \lambda \mathcal{L}, \quad (2.18)$$

where \mathcal{L} denotes the propagation path length through the turbulent medium, and safely ignore amplitude fluctuations (Roddier, 1981). Fried (1966) showed, that in this case the wave structure function is equal to the phase structure function:

$$\mathcal{D}(\vec{r}) = \mathcal{D}_l(\vec{r}) + \mathcal{D}_\phi(\vec{r}) = \mathcal{D}_\phi(\vec{r}) \quad (\text{near field case}). \quad (2.19)$$

2.3 Adaptive optics

Adaptive optics have been suggested a long time ago (Babcock, 1953). The concept includes the sensing of the wavefront distortions introduced by Earth's atmosphere in-situ and correcting them in real-time within a control loop (see Fig. 2.1, green part).

The sensing of the wavefront corrugation is ideally done on-axis, i.e. in the direction of the object observed (source A in Fig. 2.1). In night time astronomy, the object of interest often is not bright enough to measure the aberrated wavefront. In cases like this, a bright source (reference star B or "lockpoint") in the vicinity

of the object is facilitated to measure the wavefront distortion. However, this method is only effective as long as reference and observed star are not separated by a viewing angle larger than the isoplanatic angle

$$\theta_{\text{ISO}} = 0.341 \cos(\zeta) \frac{r_0}{h}, \quad (2.20)$$

where only one dominant layer at height h above the telescope was assumed here. The reason is that the light waves of sources A and B propagate along different paths through the turbulent atmosphere. Thus the wavefront is corrugated differently and a correction of the phase is valid for the reference source only, and not for the object of interest. A more detailed description can be found in [Hardy \(1998\)](#).

In order to overcome this problem, the concept of multi-conjugate adaptive optic systems has been proposed (e.g. [Beckers, 1988](#)). It extends the phase correction to additional turbulent atmospheric layers at different heights above the telescope. From the definition of θ_{ISO} it is clear that a high altitude turbulence layer reduces the isoplanatic angle while low altitude layers only contribute aberrations that are constant over the whole field-of-view and do not introduce anisoplanatism ($\theta_{\text{ISO}} \rightarrow \infty$). Thus, correcting the strongest turbulence layers at high heights promises to increase θ_{ISO} . A fully functional system has yet to be presented although a few MCAO systems have successfully been tested at solar telescopes ([Berkefeld *et al.* \(2006\)](#), [Rimmele *et al.* \(2006\)](#)).

Classical adaptive optics systems as suggested by Babcock use only one wavefront sensor and only one deformable mirror in a control loop to correct the wavefront aberration introduced by the atmosphere as well as static and quasi static degradations because of imperfections of the optical system (i.e. telescope) itself. These aberrations are often measured in Zernike polynomials (see [App. B](#)). As orthonormal functions on a circle they are convenient for all optical elements with annular aperture, and their lowest orders are well known aberrations like defocus, astigmatism and coma.

For a long time, the major problem of AO systems was to sense the aberrations and adjust the phase correcting device at a frequency high enough to concur in the correlation time of the atmospheric phase aberration, which, as noted before, is

2. HIGH-RESOLUTION TECHNIQUES FOR SOLAR OBSERVATIONS

usually in the millisecond regime. The first prototypes of AO systems for night-time observations were built at military facilities in the 1970s (Hardy, 1998). Solar AO systems are computationally more complex and have been introduced to various telescopes since the mid 1990s.

Even though the advances in this field have been tremendous, no AO system will ever be capable to correct atmospherically induced wavefront distortions completely. There are many reasons which include limited bandwidth, limited number of degrees of freedom, finite spatial sampling of the wavefront by the wavefront sensor, and noise. Furthermore, analysis of recorded wavefront sensor data shows that the correction degrades with Zernike higher mode number, paying tribute to the shorter correlation times of small scale aberrations.

In this thesis, the definition of a new entity is presented as

$$\hat{\beta}_i = 1 - \sqrt{\frac{\sigma_{i,\text{on}}^2}{\sigma_{i,\text{off}}^2}}, \quad (2.21)$$

where $\sigma_{i,\text{off}}^2$ is the variance of the i -th Zernike mode without AO correction, and $\sigma_{i,\text{on}}^2$ the one with activated AO system. This entity is a measure for the performance of correction of certain Zernike modes. Theoretically, $\hat{\beta}_i$ can take on values between $-\infty \leq \hat{\beta}_i \leq 1$, $\forall i \geq 2$. If $\hat{\beta}_i = 1$ for a certain Zernike mode i , this mode was completely corrected by the system. A value of $0 < \hat{\beta}_i < 1$ indicates a partial correction of mode i . In case that $\hat{\beta}_i = 0$, the i -th mode was not corrected by the system at all. A negative value of a specific $\hat{\beta}_i$ indicates an increased variance of mode i , meaning that the mode was not corrected but amplified by the AO system. This can happen if the AO system's bandwidth is much too small to concur with the correlation time of the atmosphere. Throughout the rest of this work, it is assumed that $-1 \leq \hat{\beta}_i \leq 1$, $\forall i \geq 2$ – the use of an AO system that amplifies Zernike mode variances by more than a factor of 4 is simply unpractical.

In Fig. 2.2, the performance of the Kiepenheuer Adaptive Optics System (KAOS) (von der Lühe *et al.*, 2003) is compared to that of the system of the National Solar Observatory (Rimmele *et al.*, 2004), both of which are AO systems for solar observations. As a low-order system, KAOS is able to partially correct up to 27 Zernike polynomials, whereas the NSO system was designed as high-order

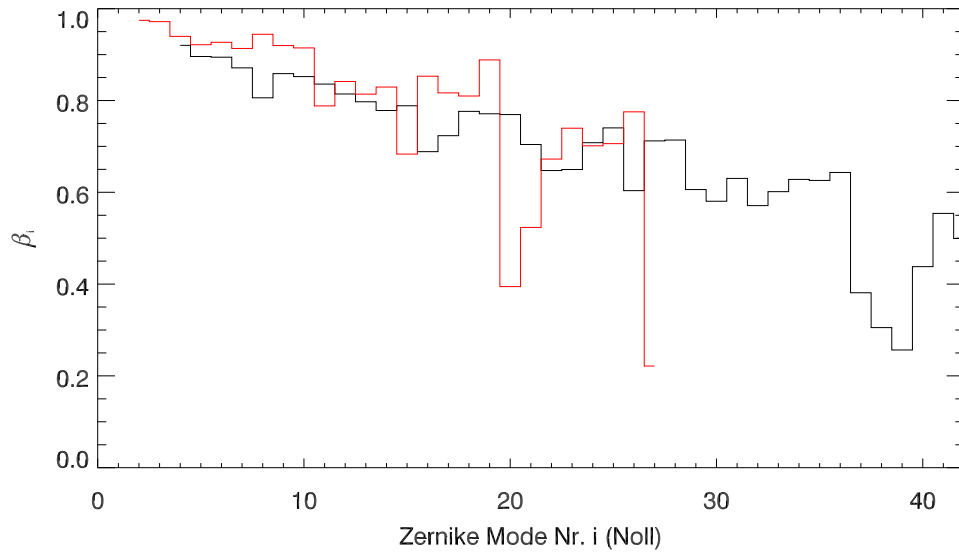


Figure 2.2: Suppression of Zernike modes for two different solar AO systems: KAOS installed in the Vacuum Tower Telescope at the Observatorio del Teide on Tenerife, Spain (red) and the system installed by the National Solar Observatory in the Dunn Solar Telescope in New Mexico, USA (black). Both show a similar behavior: the higher the Zernike mode number, the worse their suppression.

2. HIGH-RESOLUTION TECHNIQUES FOR SOLAR OBSERVATIONS

system and can correct more than 40 modes. Additionally to the decreasing performance with increasing Zernike mode number, both systems correct certain modes of the same radial order with different performance. The reason is that the spatial sampling of the wavefront sensor is often not sufficient to resolve all modes with the same accuracy. The measure for performance $\hat{\beta}_i$ is dependent on Fried's parameter r_0 . The performance decreases with decreasing r_0 , because the wavefront cannot be measured anymore. Owing to the fact that the curves in Fig. 2.2 were measured under different seeing conditions, there is no conclusive information on what system shows better performance.

2.4 Speckle interferometry

Speckle interferometry is a method of removing the effects of the wavefront distortion caused by the atmosphere post-facto, i.e. after the data was acquired, using many short-exposed images observed within a time interval in which the object has not changed. As discussed above, short-exposed images are capable of freezing in the realization of the atmosphere at the instant the image was acquired. A statistical analysis of the Fourier transforms of many such images allows the reconstruction of one image that is not degraded by atmospheric effects; static aberrations of the telescope, however, will still be present. One can think of this as an averaging process, where the non-stationary information is averaged out while the static information is retained.

Suppose that one observes an object with a telescope of infinite aperture in space (i.e. without atmospheric aberrations). The Fourier transform of the recorded image $O(\vec{x})$ can be written as

$$\tilde{O}(\vec{s}) = A_O(\vec{s}) + iB_O(\vec{s}) = R_O(\vec{s}) \exp[i\psi_O(\vec{s})], \quad (2.22)$$

where

$$R_O(\vec{s}) = \sqrt{A_O^2(\vec{s}) + B_O^2(\vec{s})} = |\tilde{O}| \text{ and } \psi_O(\vec{s}) = \arctan \frac{B_O(\vec{s})}{A_O(\vec{s})}. \quad (2.23)$$

In reality, earthbound observations of an object in the sky lead to the recording

of an image $I(\vec{x})$ in the focal plane of the telescope. The result of its Fourier transform may be written as

$$\tilde{I}(\vec{s}) = A_I(\vec{s}) + iB_I(\vec{s}) = R_I(\vec{s}) \exp[i\psi_I(\vec{s})], \quad (2.24)$$

where $R_I(\vec{s})$ and $\psi_I(\vec{s})$ can be expressed in the same way as above. In general, both the value of Fourier amplitude $R_I(\vec{s})$ and that of Fourier phase $\psi_I(\vec{s})$, are changed by the optical system 'atmosphere and telescope' and not equal to $R_O(\vec{s})$ and $\psi_O(\vec{s})$. The aim of a recovery process must be the estimation of $R_O(\vec{s})$ and $\psi_O(\vec{s})$ from observed images $I(\vec{x})$.

Speckle interferometric algorithms usually recover the object's Fourier amplitude (Sect. 2.4.1) separately from the phase (Sect. 2.4.3). The phase reconstruction is independent of the observed source, i.e. is equally valid for stars and the surface of the Sun, whereas the amplitude recovery needs to be adjusted for solar observations. Once Fourier amplitudes and phases have been reconstructed, they are combined and then retransformed to obtain the 'true' object intensity, $O(\vec{x})$.

2.4.1 Amplitude reconstruction

This section deals with the recovery of the Fourier amplitude of an object that was observed from Earth. In Sect. 2.4.1.1, the fundamental approach is introduced to recover $R_O(\vec{s})$ as defined in equation (2.23). This motivates the need for atmospheric transfer functions (Sect. 2.4.1.2) and a robust way of estimating Fried's parameter r_0 (Sect. 2.4.2) if images of an extended source like the solar surface are to be reconstructed. In the following sections, all quantities related to I can be measured from observed data.

2.4.1.1 The Labeyrie method

Labeyrie (1970) was the first to suggest the use of averaged Fourier amplitudes from a series of short-exposed images to retrieve near diffraction limited object information. He analyzed the object by merely taking into account the average power spectra of N observed images, which include independent realizations of

2. HIGH-RESOLUTION TECHNIQUES FOR SOLAR OBSERVATIONS

the atmosphere. Starting from equation (2.5) the mathematical interpretation is

$$\langle |\tilde{I}_a(\vec{s})|^2 \rangle_N = |\tilde{O}(\vec{s})|^2 \cdot \langle |\text{OTF}_a(\vec{s})|^2 \rangle_N, \quad (2.25)$$

where $\tilde{I}_a(\vec{s})$ denotes the Fourier transform of the a -th observed short-exposed image ($1 < a < N$), and $\langle \cdot \rangle_N$ is the average over all N images. It is immediately clear that a division in the Fourier domain should recover the power spectrum (and thus Fourier amplitudes) of the 'true' object:

$$|\tilde{O}(\vec{s})|^2 = \frac{\langle |\tilde{I}_a(\vec{s})|^2 \rangle_N}{\langle |\text{OTF}_a(\vec{s})|^2 \rangle_N}, \quad (2.26)$$

This allowed the derivation of object properties that were beyond the resolution limit set by the atmosphere through the use of many short-exposed images. A few points have to be mentioned here:

- The analysis of the power spectrum ignores the images' Fourier phases. Thus, the analysis is limited to sources which have Fourier phases with a center of symmetry, like single or double star systems.
- The knowledge of $\langle |\text{OTF}_a(\vec{s})|^2 \rangle_N$, also called speckle transfer function, is vital for the amplitude reconstruction. In night astronomy usually an unresolved reference star is observed simultaneously with the object to naturally provide the PSF and thus the OTF.

Solar observations unfortunately do not provide reference point sources. When using speckle interferometry on solar data, a model including telescope properties and atmospheric turbulence needs to be created for $\langle |\text{OTF}(\vec{s})|^2 \rangle$. Additionally, it has to be noted that the OTF strongly depends on r_0 , a fact that has been ignored until now because of simplicity. Thus, the knowledge of Fried's parameter is necessary to recover the Fourier amplitude of an extended source according to equation (2.26).

The derivation of the models for the atmospheric transfer functions is given in the following, so that Fourier amplitudes of solar images can be obtained by equation (2.26).

2.4.1.2 Atmospheric transfer functions

It is convenient to start with equation (2.3). At this point, considering the phase fluctuations introduced by the atmosphere, one needs to assume that $W(\vec{r})$ is complex. The complex part which describes any phase aberration from $W(\vec{r})$ (be it static due to imperfect optics or random due to the atmosphere) can be separated, and one can rewrite the equation:

$$OTF(\vec{s}) = \int d\vec{r} W(\vec{r} + \frac{1}{2}\vec{s}) W(\vec{r} - \frac{1}{2}\vec{s}) \exp[i(\varphi(\vec{r} + \frac{1}{2}\vec{s}) - \varphi(\vec{r} - \frac{1}{2}\vec{s}))], \quad (2.27)$$

and $W(\vec{r})$ is now defined again as in equation (2.2). The important transfer functions for optical systems which image through the turbulent atmosphere will now be presented.

Long exposure transfer function

In case the exposure is taken over a time interval which is much longer than the correlation time of the atmospheric turbulence, one starts with equation (2.27) and needs to calculate

$$\begin{aligned} \langle OTF(\vec{s}) \rangle &= \langle \int d\vec{r} W(\vec{r} + \frac{1}{2}\vec{s}) W(\vec{r} - \frac{1}{2}\vec{s}) \\ &\quad \cdot \exp[i(\varphi(\vec{r} + \frac{1}{2}\vec{s}) - \varphi(\vec{r} - \frac{1}{2}\vec{s}))] \rangle \end{aligned} \quad (2.28)$$

$$\begin{aligned} &= \int d\vec{r} W(\vec{r} + \frac{1}{2}\vec{s}) W(\vec{r} - \frac{1}{2}\vec{s}) \\ &\quad \cdot \langle \exp[i(\varphi(\vec{r} + \frac{1}{2}\vec{s}) - \varphi(\vec{r} - \frac{1}{2}\vec{s}))] \rangle \end{aligned} \quad (2.29)$$

$$\begin{aligned} &= \int d\vec{r} W(\vec{r} + \frac{1}{2}\vec{s}) W(\vec{r} - \frac{1}{2}\vec{s}) \\ &\quad \cdot \exp[-\frac{1}{2} \langle \{ (\varphi(\vec{r} + \frac{1}{2}\vec{s}) - \varphi(\vec{r} - \frac{1}{2}\vec{s})) \}^2 \rangle] \end{aligned} \quad (2.30)$$

$$\begin{aligned} &= \int d\vec{r} W(\vec{r} + \frac{1}{2}\vec{s}) W(\vec{r} - \frac{1}{2}\vec{s}) \\ &\quad \cdot \exp[-\frac{1}{2} \mathcal{D}_\varphi(\vec{s})] \end{aligned} \quad (2.31)$$

The step from equations (2.29) to (2.30) uses $\langle \exp(ix) \rangle = \exp(-\frac{1}{2}\langle x^2 \rangle)$ for a Gaussian distributed random variable x with zero mean. The definition of the phase structure function appears in the exponent in equation (2.30). With equation (2.16), one thus gets (2.31). Looking at equation (2.31) more closely

2. HIGH-RESOLUTION TECHNIQUES FOR SOLAR OBSERVATIONS

shows that the exponential term is independent of the integration variable. Thus $\langle OTF(\vec{s}) \rangle$ can be seen as the product of an instrumental (integral) and an atmospheric transfer function (exponential term). This result has been reported first by [Fried \(1966\)](#).

Speckle transfer function

The speckle transfer function $\langle |OTF(\vec{s})|^2 \rangle$ is the squared transfer function of a mean short exposed image. Short exposed in this context means that the exposure time is about the correlation time of the atmosphere or shorter. Starting again with equation (2.27), it is easy to see that the speckle transfer function is a four dimensional integral:

$$\begin{aligned} \langle |OTF(\vec{s})|^2 \rangle &= \int d\vec{r} \int d\vec{r}' W(\vec{r} + \frac{1}{2}\vec{s}) W(\vec{r} - \frac{1}{2}\vec{s}) W(\vec{r}' + \frac{1}{2}\vec{s}) W(\vec{r}' - \frac{1}{2}\vec{s}) \\ &\cdot \langle \exp[i\{(\varphi(\vec{r} + \frac{1}{2}\vec{s}) - \varphi(\vec{r} - \frac{1}{2}\vec{s})) - (\varphi(\vec{r}' + \frac{1}{2}\vec{s}) - \varphi(\vec{r}' - \frac{1}{2}\vec{s}))\}] \rangle \end{aligned} \quad (2.32)$$

The integral can be simplified very similar to the long exposure transfer function. Introducing $\Delta\vec{r} = \vec{r} - \vec{r}'$, the result is ([Korff, 1973](#)):

$$\begin{aligned} \langle |OTF(\vec{s})|^2 \rangle &= \int d\vec{r} \int d\vec{r}' W(\vec{r} + \frac{1}{2}\vec{s}) W(\vec{r} + \frac{1}{2}\vec{s}) W'(\vec{r} + \frac{1}{2}\vec{s}) W'(\vec{r} + \frac{1}{2}\vec{s}) \\ &\cdot \exp[-\mathcal{D}(\vec{s}) - \mathcal{D}(\Delta\vec{r}) + \frac{1}{2}\{\mathcal{D}(\Delta\vec{r} + \vec{s}) + \mathcal{D}(\Delta\vec{r} - \vec{s})\}]. \end{aligned} \quad (2.33)$$

The speckle transfer function is of fundamental importance for the estimation of the Fourier amplitudes of solar images using equation (2.26).

2.4.2 Fried parameter estimation

In Sect. 2.4.1.2, the derivation for transfer functions under given atmospheric conditions were modeled. Each transfer function, be it for a long or a short exposure, depends on Fried's parameter r_0 (defined in equation (2.17)). The knowledge of r_0 is thus essential for choosing the correct speckle transfer function in equation (2.26). A wrongly applied transfer function leads to photometric errors which will falsify measurements of solar properties such as the rms-contrast of the solar granulation. However, the estimation of r_0 is not an easy task and many methods for its measurement have been suggested in the field of astronomy.

In solar physics, the most common way to retrieve the r_0 from image data is via the computation of the spectral ratio which is defined as (Von der L u e, 1984)

$$\epsilon(\vec{s}, r_0) = \frac{|\tilde{O}(\vec{s})|^2 \cdot |\langle \text{OTF}_a(\vec{s}, r_0) \rangle_N|^2}{|\tilde{O}(\vec{s})|^2 \cdot \langle |\text{OTF}_a(\vec{s}, r_0)|^2 \rangle_N} = \frac{|\langle \text{OTF}_a(\vec{s}, r_0) \rangle_N|^2}{\langle |\text{OTF}_a(\vec{s}, r_0)|^2 \rangle_N} = \frac{|\langle \tilde{I}_a \rangle_N|^2}{\langle |\tilde{I}_a|^2 \rangle_N}. \quad (2.34)$$

For clarity, the dependency of OTF_a on r_0 is explicitly stated. As always, $\tilde{I}_a(\vec{s})$ is the Fourier transform of the a -th observed image. If one assumes azimuthal symmetry of $W(\vec{r})$ and no static aberrations, the spectral ratio depends only on $s = |\vec{s}|$. In this case

$$\epsilon(s, r_0) = \frac{\text{Long Exposure Transfer Function}^2(s, r_0)}{\text{Speckle Transfer Function}(s, r_0)} \quad (2.35)$$

Based on the results of Sect. 2.4.1.2, a precomputed table of model functions computed for equidistant frequency values s and many values of r_0 is used for the estimation of r_0 . Model and measurement $|\langle \tilde{I}_a \rangle_N|^2 / \langle |\tilde{I}_a|^2 \rangle_N$ of the spectral ratio are compared in one dimension, the best fit giving the value of r_0 .

In this work, the fitting algorithm was changed from the algorithm described by Von der L u e (1984) to a direct fit at each frequency point of the model to measured data using the sum of their squared differences as error metric. Additionally, at each frequency point, the squared difference was weighted with the variance of the measured spectral ratio. The fit is done with two iterations, going from a coarse to a fine grid of r_0 using bilinear interpolation (for s and r_0), and finally estimating r_0 from the minimum of a parabolic fit to the squared differences (see Fig. 3.7 for some examples).

2.4.3 Phase reconstruction

In this section, the principles of phase reconstruction using speckle interferometry is explained. This is the process in which the object's phase $\psi_O(\vec{s})$ defined in equation (2.23) is estimated. With

$$P^{n,m}(\vec{u}_1, \dots, \vec{u}_n, \vec{v}_1, \dots, \vec{v}_m) = \langle \tilde{I}_a(\vec{u}_1) \cdots \tilde{I}_a(\vec{u}_n) \cdot \tilde{I}_a^*(\vec{v}_1) \cdots \tilde{I}_a^*(\vec{v}_m) \rangle_N \quad (2.36)$$

2. HIGH-RESOLUTION TECHNIQUES FOR SOLAR OBSERVATIONS

one can define the average polyspectrum of order $n + m$, where \vec{u}_k and \vec{v}_l are two-dimensional frequency coordinates and $\langle \cdot \rangle_N$ designates the average over N polyspectra. The use of polyspectra in the problem of phase recovery is motivated by the assumption that phase aberrations induced by atmospheric turbulence follow Gaussian statistics with zero mean. Polyspectra of order equal to two and higher are capable to preserve the phase information of the signal (Nikias & Raghuveer, 1987, and references therein) (the power spectrum, even though it can be understood as a special case of a polyspectrum of second order, is an exception). Thus, the mean polyspectrum will retain only the phase information that is constant while random fluctuations as those induced by the atmosphere average out.

After the first attempts of Labeyrie (1970) to compensate the atmosphere in the Fourier domain (see Sect. 2.4.1), the idea to analyze the Fourier coefficients using averaged polyspectra was quickly picked up by others. Four years later, Knox & Thompson (1974) were the first to introduce phase averaging using the cross-spectrum, which is also a polyspectrum of second order. An extension to this method was proposed by Ayers *et al.* (1988). A more general approach was suggested by Weigelt (1977) and Lohmann *et al.* (1983) who extended the averaging to $P^{2,1}$, a polyspectrum of third order which is also known as bispectrum. The implemented methods of phase reconstruction will be briefly reviewed in the following.

2.4.3.1 Extended Knox-Thompson

The deeper reason for the successful application of speckle interferometry lies within the transfer function of the averaging process. The polyspectrum of second order $P^{1,1}$ can be expressed slightly different when making a change of variables in equation (2.36) from $\vec{u}_1 = \vec{s}$ and $\vec{v}_1 = \vec{s} - \vec{\delta}$. Then, starting with equation (2.5), one can compute the average cross-spectrum of Fourier transform $\tilde{I}(\vec{s})$

$$C(\vec{s}, \vec{\delta}) = \tilde{O}(\vec{s})\tilde{O}^*(\vec{s} - \vec{\delta}) \cdot \langle \text{OTF}_a(\vec{s})\text{OTF}_a^*(\vec{s} - \vec{\delta}) \rangle_N = \langle \tilde{I}_a(\vec{s})\tilde{I}_a^*(\vec{s} - \vec{\delta}) \rangle_N \quad (2.37)$$

from N short-exposed images $I_a(\vec{x})$, $1 < a < N$, that were taken within a time interval in which the object does not change. Knox & Thompson (1974)

2.4 Speckle interferometry

showed that, as long as the modulus of the shift $\delta = |\vec{\delta}|$ is not larger than the seeing limit in the Fourier domain, r_0/λ , the *Knox-Thompson transfer function* $\langle \text{OTF}(\vec{s})\text{OTF}^*(\vec{s} - \vec{\delta}) \rangle$ remains non-zero and finite up to the diffraction limit in the Fourier space, D/λ . A detailed analysis of the transfer function can be found in [Von der Lühe \(1988\)](#). Most importantly for the phase reconstruction process, the Knox-Thompson transfer function is a real entity and thus does not introduce a phase bias. For this reason, it is possible to neglect the transfer function itself and reconstruct the object phase by evaluating the normalized cross-spectrum

$$\|C(\vec{s}, \vec{\delta})\| = \frac{C(\vec{s}, \vec{\delta})}{|C(\vec{s}, \vec{\delta})|} = \frac{\tilde{O}(\vec{s})\tilde{O}^*(\vec{s} - \vec{\delta})}{|\tilde{O}(\vec{s})\tilde{O}^*(\vec{s} - \vec{\delta})|}. \quad (2.38)$$

The object phase recovery from the cross-spectrum $\|C(\vec{s}, \vec{\delta})\|$ involves a recursive and an iterative step. For the phase recovery process, the value at the frequency origin needs to be given as start value; this is equivalent to setting the average intensity in the image. Usually this value is set to the complex number (1,0) or the value of $(\sqrt{C(0,0)}, 0)$; the phase at frequency origin is always zero. The original algorithm was implemented with *just two* orthogonal shifts $\vec{\delta}$. The extended algorithm ([Ayers et al., 1988](#)) uses *all available* shifts up to the seeing limit. Let

$$\Delta = \{\vec{\delta} : 0 < |\vec{\delta}| \leq r_0/\lambda\} \quad (2.39)$$

be the set of admissible shift vectors $\vec{\delta}$. From the frequency origin outwards the phase at frequency \vec{s} is then estimated recursively by computing

$$\|\tilde{O}(\vec{s})\| = \left\langle \frac{\|C(\vec{s}, \vec{\delta})\|}{\|\tilde{O}^*(\vec{s} - \vec{\delta})\|} \right\rangle_{\Delta \cap \{\vec{\delta} : 0 \leq |\vec{s} - \vec{\delta}| < |\vec{s}|\}} \quad (2.40)$$

Once each point in the frequency domain has been assigned a phase value, the phase errors are iteratively reduced using a successive over-relaxation scheme:

$$\|\tilde{O}(\vec{s})\| = \left\langle \frac{\|C(\vec{s}, \vec{\delta})\|}{\|\tilde{O}^*(\vec{s} - \vec{\delta})\|} \right\rangle_{\Delta} \quad (2.41)$$

The algorithmic details are described in [Mikurda & Von Der Lühe \(2006\)](#).

2. HIGH-RESOLUTION TECHNIQUES FOR SOLAR OBSERVATIONS

2.4.3.2 Triple correlation

Knox & Thompson's idea can be generalized, which make the procedure insensitive to a total image shift, and thus more robust. A restricted polyspectrum of third order, $P^{2,1}$, is utilized. The restriction is expressed in the new definition of the variables in equation (2.36): with $\vec{u}_1 = \vec{u}$, $\vec{u}_2 = \vec{v}$ and $\vec{v}_1 = \vec{u} + \vec{v}$ it can be seen that the dimensionality of the polyspectrum of third order is reduced from six to four. With this, the average bispectrum is defined as

$$B(\vec{u}, \vec{v}) = \langle \tilde{I}_a(\vec{u}) \tilde{I}_a(\vec{v}) \tilde{I}_a^*(\vec{u} + \vec{v}) \rangle_N \quad (2.42)$$

Following the steps in Sect. 2.4.3.1, one can define the *speckle masking transfer function* in analogy to the Knox-Thompson transfer function. This transfer function remains finite, non-zero and real up to the diffraction limit for any combination of \vec{u} and \vec{v} within the diffraction limit (Lohmann *et al.* (1983), and in further detail Von der L u e (1985)), which is in contrast to the Knox-Thompson case where there was a boundary to $\vec{\delta}$ (see equation (2.39)). The normalized average bispectrum can then be written as

$$\|B(\vec{u}, \vec{v})\| = \frac{\tilde{O}(\vec{u}) \tilde{O}(\vec{v}) \tilde{O}^*(\vec{u} + \vec{v})}{|\tilde{O}(\vec{u}) \tilde{O}(\vec{v}) \tilde{O}^*(\vec{u} + \vec{v})|}. \quad (2.43)$$

In complete analogy to the Knox-Thompson case one can estimate the phase if an assumption about the phase around the frequency origin is made. Again, one can set the phases to zero or to the mean values, which, because they are the lowest frequencies, are usually unaffected by seeing. The latter has certain advantages for extended sources like the solar surface. Denoting the set of admissible vectors as

$$\Pi = \{\vec{u}, \vec{v} : |\vec{u}| \leq D/\lambda \wedge |\vec{v}| \leq D/\lambda \wedge |\vec{u} + \vec{v}| \leq D/\lambda\} \quad (2.44)$$

the object's phase can be restored recursively by

$$\|\tilde{O}(\vec{v})\| = \left\langle \frac{\|B(\vec{u}, \vec{v})\|}{\|\tilde{O}(\vec{u})\| \|\tilde{O}^*(\vec{u} + \vec{v})\|} \right\rangle_{\Pi \cap \{\vec{u}, \vec{v} : |\vec{u}| < |\vec{v}| \wedge |\vec{u} + \vec{v}| < |\vec{v}|\}} \quad (2.45)$$

The recursive approach only uses a subset of the available average bispectrum values. Additionally to the common recursive approach, an iterative weighted least-squares approach (Matson, 1991) was implemented. Matson showed that the reconstruction of the object's phase, seen as the solution of a weighted least-squares problem, leads to the expression for the object's phase at frequency \vec{v}

$$\begin{aligned} \|O(\vec{v})\| = & \sum_{\vec{u} \neq \vec{v}} w(\vec{u}, \vec{v}) \left[\frac{\|B(\vec{u}, \vec{v})\|}{\|O(\vec{u})\| \|O^*(\vec{u} + \vec{v})\|} \right] + \sum_{\vec{u} = \vec{v}} 4w(\vec{u}, \vec{v}) \left[\frac{\|B(\vec{u}, \vec{v})\|}{\|O^*(\vec{u} + \vec{v})\|} \right]^{1/2} \\ & + \sum_{\vec{u}, \vec{v}} w(\vec{u}, \vec{v} - \vec{u}) \left[\frac{\|B(\vec{u}, \vec{v} - \vec{u})\|}{\|O(\vec{u})\| \|O(\vec{v} - \vec{u})\|} \right]^* . \end{aligned} \quad (2.46)$$

Here, $w(\vec{u}, \vec{v})$ are the weights, which is usually the signal-to-noise ratio of the bispectrum at the particular frequencies. The first two sums come from solving equation (2.43) for $\|O(\vec{u})\|$ and $\|O(\vec{v})\|$, the last one from solving it for $\|O(\vec{u} + \vec{v})\|$ and making a change of variables from \vec{v} to $\vec{v} - \vec{u}$. All previously calculated average bispectrum values are used. However, it can be seen that because the solutions are coupled, the solution for the whole phase spectrum needs to be found iteratively.

2.5 Conclusion

Earth's atmosphere, while having undisputed advantages for the living creatures on its surface, is the main cause of image degradation when observing extra-terrestrial objects. The reason is the deformation of a plane wavefront as emitted by the observed source because of variations of the refractive index in the turbulent layers of the atmosphere. Several techniques have been suggested to reduce or eliminate the degradation. These fall into two categories, which are on the one hand, adaptive optics (AO) systems that correct the wavefront in-situ in real-time at the telescope, and on the other hand, post-facto image reconstruction techniques based on the theory of atmospheric turbulence. In general, any AO compensation is only partial and valid for a small field-of-view motivating further techniques to obtain data which resolve the object up to the diffraction limit of the telescope. Speckle interferometry is a promising candidate of image post-processing in combination with AO corrected data. Thus, in the course of

2. HIGH-RESOLUTION TECHNIQUES FOR SOLAR OBSERVATIONS

this work a computer program based on the theory of speckle interferometry described in this Chapter was written for parallel processing in ANSI-C (App. A) in order to reconstruct images with a resolution limited only by the diffraction of the telescope.

However, in order to use speckle interferometry in combination with AO corrected data, the transfer functions derived in Sect. 2.4.1 need to be modified. An approach to such a modification will be presented in the following Chapter.

Chapter 3

Speckle interferometry using adaptive optics corrected data

In order to use speckle interferometry in combination with AO systems, new models for the transfer functions (Sect. 2.4.1) need to be prepared. This can be achieved by either simulating the adaptive optics system in detail (Puschmann & Sailer, 2006), or by extending existing models. In this chapter, the theory for the latter approach is developed. In order to do so, two things have to be taken into account.

The new transfer functions have to take into account an adaptive optical system of arbitrary performance. This becomes obvious by looking at the definition of the atmospheric transfer functions: the wavefront corrugation enters the convolution integral as atmospheric phase terms φ (see equation (2.27)). In its effort to flatten the wavefront, the AO reduces the phase terms, but does not zero them because of its imperfect correction. This reduction must be taken into account in equation (2.27). The values of $\hat{\beta}_i$ (equation (2.21)) provide useful estimators for the quality of the reduction and serve as input parameters for the models.

On the other hand, there is the need to account for anisoplanatism in the atmosphere which is amplified by an AO system. The correction of an AO is valid only within an angular distance from the viewing angle of the wavefront sensor that is smaller than the isoplanatic angle (see equation (2.20)). Again, this must be expressed as an increasing phase term with increasing viewing angle in equation (2.27). The modeling of transfer functions including the off-axis correction of

3. SPECKLE INTERFEROMETRY USING ADAPTIVE OPTICS CORRECTED DATA

the AO becomes especially important when observing extended sources like the solar surface, where the field-of-view often extends over an angle which is many times that of the isoplanatic angle.

In what follows, both the long exposure transfer function (Sect. 3.1) and the speckle transfer function (Sect. 3.2) have been remodeled for the data obtained with an arbitrary AO system. An approach to take into account the off-axis correction of an AO system is presented in Sect. 3.3. In Sect. 3.5, the results of the new models are presented.

3.1 Long exposure transfer function of an arbitrary adaptive optics system

Following the calculations of [J. Y. Wang \(1978\)](#), one starts with equation (2.27) and takes into account an adaptive optics correction of the lowest N Zernike modes. This would cause a phase difference of $\phi(\vec{r})$ to the pure atmospheric phase aberrations $\varphi(\vec{r})$ and the convolution integral becomes

$$S(\vec{s}) = \int d\vec{r} W(\vec{r} + \frac{1}{2}\vec{s}) W(\vec{r} - \frac{1}{2}\vec{s}) \cdot \exp[i\{(\varphi(\vec{r} + \frac{1}{2}\vec{s}) - \phi(\vec{r} + \frac{1}{2}\vec{s})) - (\varphi(\vec{r} - \frac{1}{2}\vec{s}) - \phi(\vec{r} - \frac{1}{2}\vec{s}))\}]. \quad (3.1)$$

One can expand the phase terms into basis functions $F_i(\vec{r})$, in this case Zernike polynomials, and obtain

$$\varphi(\vec{r}) = \sum_{i=2}^{\infty} a_i F_i(\vec{r}) \quad (3.2)$$

for the atmospheric phase and, introducing a set of parameters β_i which describes the efficiency with which each polynomial is corrected by the AO system,

$$\phi(\vec{r}) = \sum_{i=2}^N \beta_i a_i F_i(\vec{r}) \quad (3.3)$$

for the correcting phase. Here i indicates the Zernike index in the notation of [Noll \(1976\)](#) and a_i its coefficient of atmospheric turbulence (for a given Fried parameter) for the i -th Zernike polynomial.

3.1 Long exposure transfer function of an arbitrary adaptive optics system

The significance of the parameter set β_i , for which one can assume (see Sect. 2.3 for an explanation)

$$-1 < \beta_i < 1, \quad i = 2, \dots, N, \quad (3.4)$$

is best illustrated by the following examples. In case of $\beta_i = 0 \forall i = 2, \dots, N$, there is no correction of an adaptive optics system. The model reduces to equation 2.31. In case of $\beta_i = 1 \forall i = 2, \dots, N$, the adaptive optics system corrects the first N Zernike modes completely and the model represents the solution by [J. Y. Wang \(1978\)](#). The parameter set allows to model for each Zernike mode separately the efficiency with which the mode is corrected by the AO system. In case of $\exists i : \beta_i < 0$ the i -th mode is not corrected but amplified by the system. This allows for the modeling of an *off-axis* correction if the correlation coefficient of the Zernikes over the field-of-view is known. This will be elaborated further in Sect. 3.3.

To obtain the long exposure transfer function (LTF), one needs to calculate $\langle S(\vec{s}) \rangle$. It is convenient to introduce an abbreviation of the argument of a function \mathcal{F}

$$\mathcal{F}^+ = \mathcal{F}(\vec{r} + \frac{1}{2}\vec{s}) \text{ and } \mathcal{F}^- = \mathcal{F}(\vec{r} - \frac{1}{2}\vec{s}). \quad (3.5)$$

Taking the average of $S(\vec{s})$ in equation (3.1) and sorting the terms delivers

$$\langle S(\vec{s}) \rangle = \int d\vec{r} W^+ W^- \cdot \langle \exp[i\{(\varphi^+ - \varphi^-) - (\phi^+ - \phi^-)\}] \rangle, \quad (3.6)$$

with the notation described above.

With the use of the conventional assumption that $\varphi - \langle \varphi \rangle$ and $\phi - \langle \phi \rangle$ are Gaussian distributed random variables with zero mean¹. In this case the equality $\langle \exp[ix] \rangle = \exp[-\frac{1}{2}\langle x^2 \rangle]$ holds, and one can write

$$\langle S(\vec{s}) \rangle = \int d\vec{r} W^+ W^- \cdot \langle \exp[i\{(\varphi^+ - \langle \varphi \rangle) - (\varphi^- - \langle \varphi \rangle) - (\phi^+ - \langle \phi \rangle) + (\phi^- - \langle \phi \rangle)\}] \rangle$$

¹This assumption means that each coefficient of the Zernike expansion of the turbulence is Gaussian itself.

3. SPECKLE INTERFEROMETRY USING ADAPTIVE OPTICS CORRECTED DATA

$$\begin{aligned}
&= \int d\vec{r} W^+ W^- \\
&\quad \cdot \exp\left[-\frac{1}{2}\{(\varphi^+ - \langle\varphi\rangle) - (\varphi^- - \langle\varphi\rangle) - (\phi^+ - \langle\phi\rangle) + (\phi^- - \langle\phi\rangle)\}^2\right] \\
&= \int d\vec{r} W^+ W^- \\
&\quad \cdot \exp\left[-\frac{1}{2}\{(\varphi^+ - \varphi^-)^2 + (\phi^+ - \phi^-)^2 - 2(\varphi^+ - \varphi^-)(\phi^+ - \phi^-)\}\right]
\end{aligned} \tag{3.7}$$

In equation (2.16) the structure function was defined to $\mathcal{D}(|\vec{s}|) = \langle(\varphi^+ - \varphi^-)^2\rangle$, and one arrives at

$$\begin{aligned}
\langle S(\vec{s}) \rangle &= \int d\vec{r} W^+ W^- \\
&\quad \cdot \exp\left[-\frac{1}{2}\mathcal{D}(\vec{s}) - \frac{1}{2}\langle(\phi^+ - \phi^-)^2\rangle + \langle(\varphi^+ - \varphi^-)(\phi^+ - \phi^-)\rangle\right]
\end{aligned} \tag{3.8}$$

Let

$$\phi^+ = \sum_{i=2}^N \beta_i a_i F_i^+ \quad \phi^- = \sum_{i=2}^N \beta_i a_i F_i^- \tag{3.9}$$

$$\varphi^+ = \sum_{i=2}^{\infty} a_i F_i^+ \quad \varphi^- = \sum_{i=2}^{\infty} a_i F_i^-. \tag{3.10}$$

Then

$$T(\vec{r}, \vec{s}) = \langle[\varphi^+ - \varphi^-][\phi^+ - \phi^-]\rangle - \frac{1}{2}\langle[\phi^+ - \phi^-]^2\rangle \tag{3.11}$$

$$= \sum_{i=2}^N \sum_{i'=2}^N \beta_{i'} \langle a_i a_{i'} \rangle (F_i^+ - F_i^-)(F_{i'}^+ - F_{i'}^-) \tag{3.12}$$

$$+ \sum_{i=N+1}^{\infty} \sum_{i'=2}^N \beta_{i'} \langle a_i a_{i'} \rangle (F_i^+ - F_i^-)(F_{i'}^+ - F_{i'}^-) \tag{3.13}$$

$$- \frac{1}{2} \sum_{i=2}^N \sum_{i'=2}^N \beta_i \beta_{i'} \langle a_i a_{i'} \rangle (F_i^+ - F_i^-)(F_{i'}^+ - F_{i'}^-) \tag{3.14}$$

$$= \sum_{i=2}^N \sum_{i'=2}^N \beta_{i'} \left(1 - \frac{1}{2}\beta_i\right) \langle a_i a_{i'} \rangle (F_i^+ - F_i^-)(F_{i'}^+ - F_{i'}^-) \tag{3.15}$$

3.2 Speckle transfer function of an arbitrary adaptive optics system

$$+ \sum_{i=N+1}^{\infty} \sum_{i'=2}^N \beta_{i'} \langle a_i a_{i'} \rangle (F_i^+ - F_i^-) (F_{i'}^+ - F_{i'}^-) \quad (3.16)$$

The first summand in equation (3.11) was expanded into two double sums (3.12), (3.13). The terms (3.12), (3.14) were then combined into (3.15), to simplify the calculation. The atmospheric covariances $\langle a_i a_{i'} \rangle$ of the Zernike polynomials were calculated first by Noll (1976). Defining

$$K(\vec{r}, \vec{s}) = \sum_{i=2}^N \sum_{i'=2}^N \beta_{i'} (1 - \frac{1}{2} \beta_i) \langle a_i a_{i'} \rangle (F_i^+ - F_i^-) (F_{i'}^+ - F_{i'}^-) \quad (3.17)$$

$$L(\vec{r}, \vec{s}) = \sum_{i=N+1}^{\infty} \sum_{i'=2}^N \beta_{i'} \langle a_i a_{i'} \rangle (F_i^+ - F_i^-) (F_{i'}^+ - F_{i'}^-) \quad (3.18)$$

one gets for the long exposure transfer function under partial AO correction:

$$\langle S(\vec{s}) \rangle = \int d\vec{r} W^+ W^- \cdot \exp[-\frac{1}{2} \mathcal{D}(\vec{s}) + K(\vec{r}, \vec{s}) + L(\vec{r}, \vec{s})] \quad (3.19)$$

The terms $K(\vec{r}, \vec{s})$ and $L(\vec{r}, \vec{s})$ describe the influence of the AO system on this transfer function and can be separated from the atmospheric phase term. This can be seen when comparing the long exposure transfer function of an arbitrarily correcting adaptive optics system in equation (3.19) with its equivalent without correction in equation (2.31).

3.2 Speckle transfer function of an arbitrary adaptive optics system

The Speckle Transfer Function (STF) is defined as $\langle |S(\vec{s})|^2 \rangle$. It describes the squared transfer function of a mean short exposed image under given atmospheric conditions. Expanding the notation in equation (3.5) to primed variables

$$\mathcal{F}'^+ = \mathcal{F}(r^{\vec{j}} + \frac{1}{2} \vec{s}) \text{ and } \mathcal{F}'^- = \mathcal{F}(r^{\vec{j}} - \frac{1}{2} \vec{s}), \quad (3.20)$$

3. SPECKLE INTERFEROMETRY USING ADAPTIVE OPTICS CORRECTED DATA

one gets

$$\begin{aligned} \langle |S(\vec{s})|^2 \rangle &= \int d\vec{r} \int d\vec{r}' W^+ W^- W'^+ W'^- \\ &\cdot \langle \exp[i\{(\varphi^+ - \phi^+) - (\varphi^- - \phi^-) - (\varphi'^+ - \phi'^+) + (\varphi'^- - \phi'^-)\}] \rangle, \end{aligned} \quad (3.21)$$

similar to equation (3.7). One can generally state that

$$\langle |S(\vec{s})|^2 \rangle = \int d\vec{r} \int d\vec{r}' W^+ W^- W'^+ W'^- \cdot \langle T1 \rangle. \quad (3.22)$$

For ease of illustration, $\langle T1 \rangle$ is treated separately. Using all assumptions and results from Sect. 3.1, one gets

$$\begin{aligned} \langle T1 \rangle &= \langle \exp[(\varphi^+ - \varphi^-) - (\varphi'^+ - \varphi'^-) - (\phi^+ - \phi^-) + (\phi'^+ - \phi'^-)] \rangle \\ &= \exp[-\frac{1}{2} \langle \{(\varphi^+ - \varphi^-) - (\varphi'^+ - \varphi'^-) - (\phi^+ - \phi^-) + (\phi'^+ - \phi'^-)\}^2 \rangle] \\ &= \exp[-\frac{1}{2} \langle (\varphi^+ - \varphi^-)^2 + (\varphi'^+ - \varphi'^-)^2 + (\phi^+ - \phi^-)^2 + (\phi'^+ - \phi'^-)^2 \\ &\quad + 2\{ -((\varphi^+ - \varphi^-)(\varphi'^+ - \varphi'^-)) \\ &\quad \quad -(\varphi^+ - \varphi^-)(\phi^+ - \phi^-) + (\varphi^+ - \varphi^-)(\phi'^+ - \phi'^-) \\ &\quad \quad +(\varphi'^+ - \varphi'^-)(\phi^+ - \phi^-) - (\varphi'^+ - \varphi'^-)(\phi'^+ - \phi'^-) \} \\ &\quad -(\phi^+ - \phi^-)(\phi'^+ - \phi'^-) - (\phi'^+ - \phi'^-)(\phi^+ - \phi^-) \rangle] \end{aligned} \quad (3.23)$$

With a small calculation it can be verified that

$$\begin{aligned} \langle (\varphi^+ - \varphi^-)(\varphi'^+ - \varphi'^-) \rangle &= \frac{1}{2} \langle -(\varphi^+ - \varphi'^+)^2 + (\varphi^+ - \varphi'^-)^2 \\ &\quad +(\varphi^- - \varphi'^+)^2 - (\varphi^- - \varphi'^-)^2 \rangle \\ &= -\mathcal{D}(\Delta\vec{r}) + \frac{1}{2} \{ \mathcal{D}(\Delta\vec{r} + \vec{s}) + \mathcal{D}(\Delta\vec{r} - \vec{s}) \} \end{aligned} \quad (3.24)$$

and with $\Delta\vec{r} = \vec{r} - \vec{r}'$, one can write

$$\begin{aligned} \langle T1 \rangle &= \exp[-\{ \mathcal{D}(\vec{s}) + \frac{1}{2} \langle (\phi^+ - \phi^-)^2 \rangle + \frac{1}{2} \langle (\phi'^+ - \phi'^-)^2 \rangle \\ &\quad + \mathcal{D}(\Delta\vec{r}) - \frac{1}{2} (\mathcal{D}(\Delta\vec{r} + \vec{s}) + \mathcal{D}(\Delta\vec{r} - \vec{s})) \\ &\quad - \langle (\varphi^+ - \varphi^-)(\phi^+ - \phi^-) \rangle + \langle (\varphi^+ - \varphi^-)(\phi'^+ - \phi'^-) \rangle \} \end{aligned}$$

3.2 Speckle transfer function of an arbitrary adaptive optics system

$$\begin{aligned}
& + \langle (\varphi'^+ - \varphi'^-)(\phi^+ - \phi^-) \rangle - \langle (\varphi'^+ - \varphi'^-)(\phi'^+ - \phi'^-) \rangle \\
& - \frac{1}{2} \langle (\phi^+ - \phi^-)(\phi'^+ - \phi'^-) \rangle - \frac{1}{2} \langle (\phi'^+ - \phi'^-)(\phi^+ - \phi^-) \rangle] \\
\end{aligned} \tag{3.25}$$

$$\begin{aligned}
= & \exp[-\mathcal{D}(\vec{s}) - \mathcal{D}(\Delta\vec{r}) + \frac{1}{2} \{ \mathcal{D}(\Delta\vec{r} + \vec{s}) + \mathcal{D}(\Delta\vec{r} - \vec{s}) \} \\
& - \frac{1}{2} \langle (\phi^+ - \phi^-)^2 \rangle + \langle (\varphi^+ - \varphi^-)(\phi^+ - \phi^-) \rangle \\
& - \frac{1}{2} \langle (\phi'^+ - \phi'^-)^2 \rangle + \langle (\varphi'^+ - \varphi'^-)(\phi'^+ - \phi'^-) \rangle \\
& + \frac{1}{2} \langle (\phi^+ - \phi^-)(\phi'^+ - \phi'^-) \rangle - \langle (\varphi^+ - \varphi^-)(\phi'^+ - \phi'^-) \rangle \\
& + \frac{1}{2} \langle (\phi'^+ - \phi'^-)(\phi^+ - \phi^-) \rangle - \langle (\varphi'^+ - \varphi'^-)(\phi^+ - \phi^-) \rangle] \\
\end{aligned} \tag{3.26}$$

$$\begin{aligned}
= & \exp[-\mathcal{D}(\vec{s}) - \mathcal{D}(\Delta\vec{r}) + \frac{1}{2} \{ \mathcal{D}(\Delta\vec{r} + \vec{s}) + \mathcal{D}(\Delta\vec{r} - \vec{s}) \} \\
& + K(\vec{r}, \vec{s}) + L(\vec{r}, \vec{s}) + K(\vec{r}', \vec{s}) + L(\vec{r}', \vec{s}) \\
& - \tilde{K}(\vec{r}, \vec{r}', \vec{s}) - \tilde{L}(\vec{r}, \vec{r}', \vec{s}) - \tilde{K}(\vec{r}', \vec{r}, \vec{s}) - \tilde{L}(\vec{r}', \vec{r}, \vec{s})] \\
\end{aligned} \tag{3.27}$$

where now

$$\tilde{K}(\vec{r}, \vec{r}', \vec{s}) = \sum_{i=2}^N \sum_{i'=2}^N \beta_{i'} (1 - \frac{1}{2}\beta_i) \langle a_i a_{i'} \rangle (F_i^+ - F_i^-) (F_{i'}^+ - F_{i'}^-) \tag{3.28}$$

$$\tilde{L}(\vec{r}, \vec{r}', \vec{s}) = \sum_{i=N+1}^{\infty} \sum_{i'=2}^N \beta_{i'} \langle a_i a_{i'} \rangle (F_i^+ - F_i^-) (F_{i'}^+ - F_{i'}^-) \tag{3.29}$$

were introduced in the same way as in Sect. 3.1. The speckle transfer function of an arbitrarily compensating adaptive optics system is thus

$$\begin{aligned}
\langle |S(\vec{s})|^2 \rangle = & \int d\vec{r} \int d\vec{r}' W^+ W^- W'^+ W'^- \\
& \cdot \exp[-\mathcal{D}(\vec{s}) - \mathcal{D}(\Delta\vec{r}) + \frac{1}{2} \{ \mathcal{D}(\Delta\vec{r} + \vec{s}) + \mathcal{D}(\Delta\vec{r} - \vec{s}) \} \\
& + K(\vec{r}, \vec{s}) + L(\vec{r}, \vec{s}) + K(\vec{r}', \vec{s}) + L(\vec{r}', \vec{s}) \\
& - \tilde{K}(\vec{r}, \vec{r}', \vec{s}) - \tilde{L}(\vec{r}, \vec{r}', \vec{s}) - \tilde{K}(\vec{r}', \vec{r}, \vec{s}) - \tilde{L}(\vec{r}', \vec{r}, \vec{s})]. \\
\end{aligned} \tag{3.30}$$

In the case of $\beta_i = 0 \forall i = 2, \dots, N$, i.e. no correction, this function reduces to equation (2.33).

3. SPECKLE INTERFEROMETRY USING ADAPTIVE OPTICS CORRECTED DATA

3.3 Field dependency

As was seen in Sect. 2.3, the correction of an AO system is valid only within the isoplanatic angle. Once the field-of-view covers a larger angle, the correction reduces and could even amplify the atmospheric effects (see Sect. 2.3). Decomposing the atmospheric turbulence into Zernike polynomials allows the calculation of the spatial decorrelation coefficient of each polynomial separately. Using a one-layer turbulence model the coefficients can be calculated for different viewing angles as well as Zernike polynomials. The product of the resulting correlation coefficients (normalized to viewing angle $\gamma = 0$) and the β_i give an estimate for the correction by the AO system at the specific viewing angle.

For a viewing angle γ one can show (G. Molodij, 1997) that

$$\langle a_j(\gamma)a_j(0) \rangle = 3.895(n+1)(\alpha)^{-\frac{5}{3}} \frac{\int_0^{\mathcal{L}} dh C_n^2(h) I_{n,m}(2\gamma h/D)}{\int_0^{\mathcal{L}} dh C_n^2(h)} \quad (3.31)$$

with n and m being the radial and azimuthal Zernike degree respectively, C_n^2 the refractive-index structure constant of the turbulence at height h , \mathcal{L} being the propagation path length through the atmosphere and

$$I_{n,m}(x) = s_{n,m} \int_0^\infty d\kappa (\kappa)^{-14/3} J_{n+1}^2(\kappa) (J_0(\kappa x) + k_j J_{2m}(\kappa x)) \quad (3.32)$$

where

$$k_j = \begin{cases} 0, & \text{if } m = 0 \\ (-1)^j, & \text{if } m \neq 0 \end{cases} \quad s_{n,m} = \begin{cases} 1, & \text{if } m = 0 \\ (-1)^{n-m}, & \text{if } m \neq 0 \end{cases} \quad (3.33)$$

Eventually, if normalized to the values at viewing angle $\gamma = 0$ (which are identical to the coefficients in Noll (1976), $\langle a_j(0)a_j(0) \rangle = \langle a_j a_j \rangle$) one gets

$$\frac{\langle a_j(\gamma)a_j(0) \rangle}{\langle a_j(0)a_j(0) \rangle} = \frac{\int_0^{\mathcal{L}} dh C_n^2(h) I_{n,m}(2\gamma h/D)}{\int_0^{\mathcal{L}} dh C_n^2(h) I_{n,m}(0)}. \quad (3.34)$$

Because only one turbulence layer was assumed, the function $C_n^2(h)$ does not need to be modeled specifically.

3.4 Algorithm for the integration of the transfer functions

The product of the calculated sets of decorrelation factors and the performance parameters β_i are the input parameters for the calculation of the STFs. This yields functions which model the anisoplanatic effects introduced by an AO system.

3.4 Algorithm for the integration of the transfer functions

The integrals appearing in this Chapter were calculated using Monte Carlo integration algorithms. Using a pseudo random number generator these algorithms allow high dimensional integrals to be numerically solved. An estimate for a n-dimensional integral

$$I = \int du f(u) = \int d^n x f(x_1, \dots, x_n) \quad (3.35)$$

is given by

$$E = \frac{1}{N} \sum_{i=1}^N f(u_i). \quad (3.36)$$

Because of the law of large numbers

$$\lim_{N \rightarrow \infty} \frac{1}{N} \sum_{i=1}^N f(u_i) = I. \quad (3.37)$$

The error estimate of the Monte Carlo integration is independent of the dimension of the integral. It can be shown that the error of the estimate is inversely proportional to \sqrt{N} , thus indicating a slow convergence of the algorithm. In order to overcome this problem several techniques have evolved.

Carefully chosen random numbers can minimize the variance of the resultant value. While *stratified sampling* divides the integration space into subspaces using different number of points within each subspace, *importance sampling* changes the probability density function of the random numbers to be as close to the integrand's absolute values as possible in order to reduce the variance of the estimates for the integral.

3. SPECKLE INTERFEROMETRY USING ADAPTIVE OPTICS CORRECTED DATA

In addition, adaptive Monte Carlo methods have evolved in order to change the subspaces and the number of points therein as well as the probability density function with each iteration of the algorithm according to the integrand's dominant contributions. A widely known algorithm of this kind is the VEGAS algorithm by [Lepage \(1978\)](#) which was used for the calculation here. It is implemented in the freely available GNU Scientific Library ([GSL, 2006](#)).

The integrals appearing in equations (3.19) and (3.30) were calculated for each frequency point $q = |\vec{s}|/D$ (see equations (2.7) and (2.6)) separately for fixed values of α and sets of β_i allowing for easy parallelization. The integration at each frequency point was calculated over several iterations with at least 15000 random numbers each. The results had an acceptable error estimate even though the variance got worse with decreasing α values.

3.5 Results

The results of the calculations as well as speckle reconstructions which have been obtained with the STF's from the theory are presented here.

3.5.1 Computational results

The transfer functions were modeled for the Kiepenheuer-Institut adaptive optics system (KAOS). The parameters β_i (equation (3.4)) were, as approximation, set equal to the values of $\hat{\beta}_i$ (equation (2.21)) that were extracted from wavefront sensor data. The strength of the atmospheric turbulence has an effect on the performance of an adaptive optics system. This effect has *not* been modeled in the results presented here. Different viewing angles were included in the models as described in Sect. 3.3. All used values for β_i are displayed in Fig. 3.1. In Figures 3.2, 3.3 and 3.4, the models for various seeing conditions as well as field angles are presented. The models show the expected behavior:

1. The better the seeing, the higher the high-frequency tails of the transfer functions.

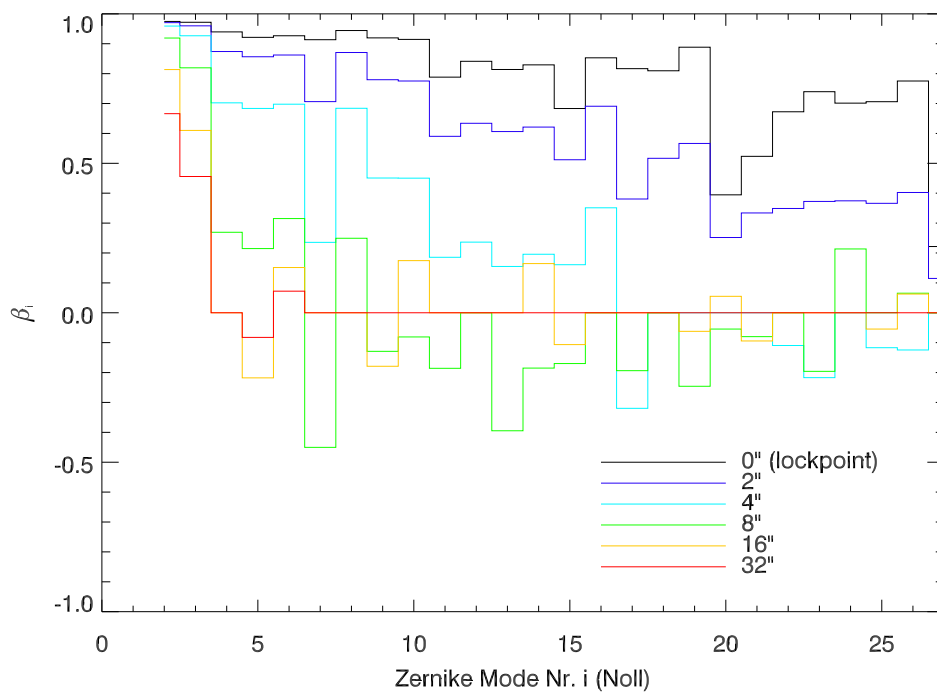


Figure 3.1: The β_i values as used for the modeling of transfer functions for KAOS. The solid curve represents the result of the evaluation of KAOS' wave front sensor data (see Sect. 2.3). The other curves were calculated by the multiplication of the solid curve with the correlation coefficients as calculated in Sect. 3.3

3. SPECKLE INTERFEROMETRY USING ADAPTIVE OPTICS CORRECTED DATA

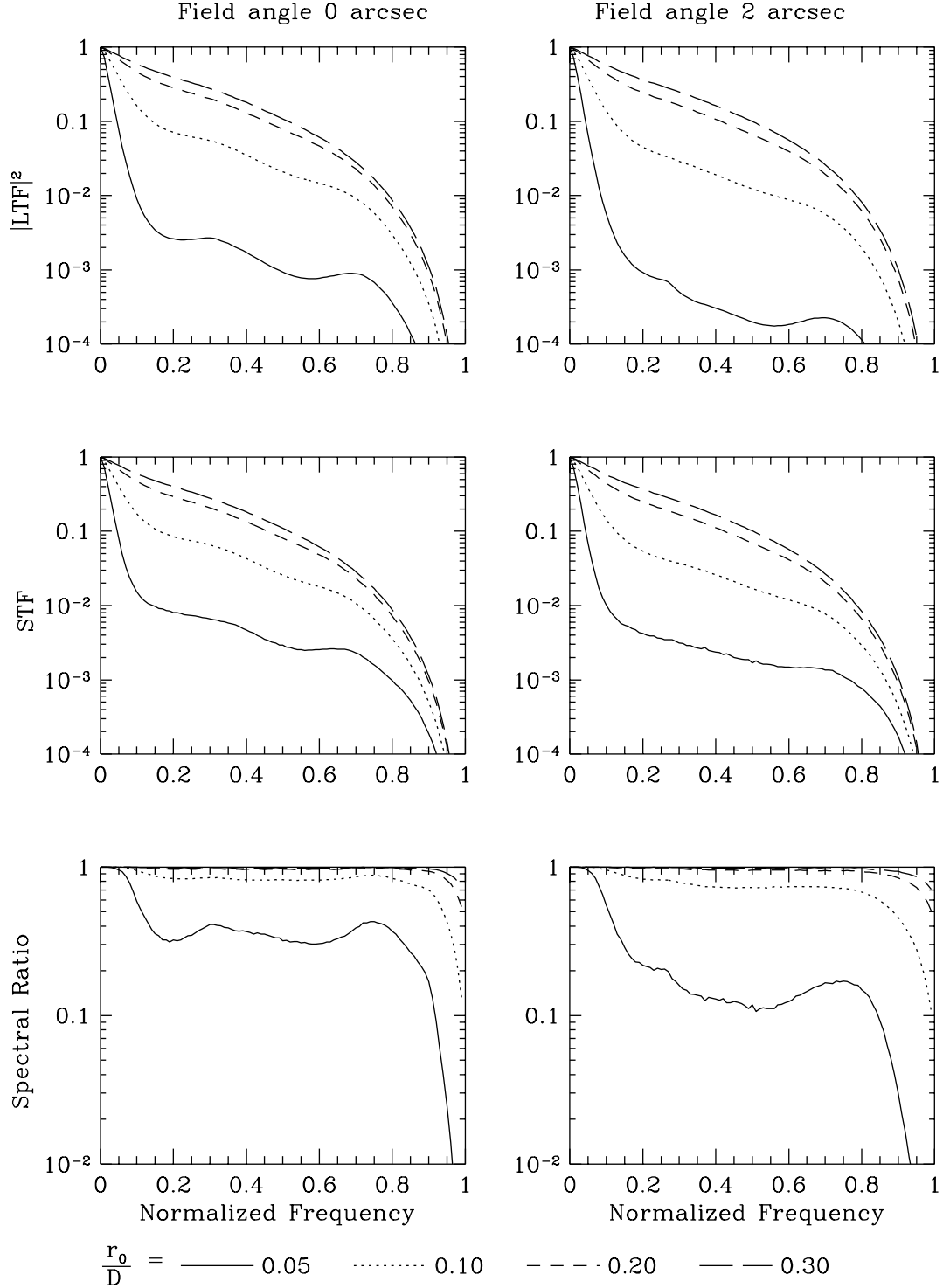


Figure 3.2: Models for $|LTF|^2$ (top panels), STF (middle) and spectral ratio (bottom) for different values of r_0 and the field angles of 0 arcs (left) and 2 arcs (right).

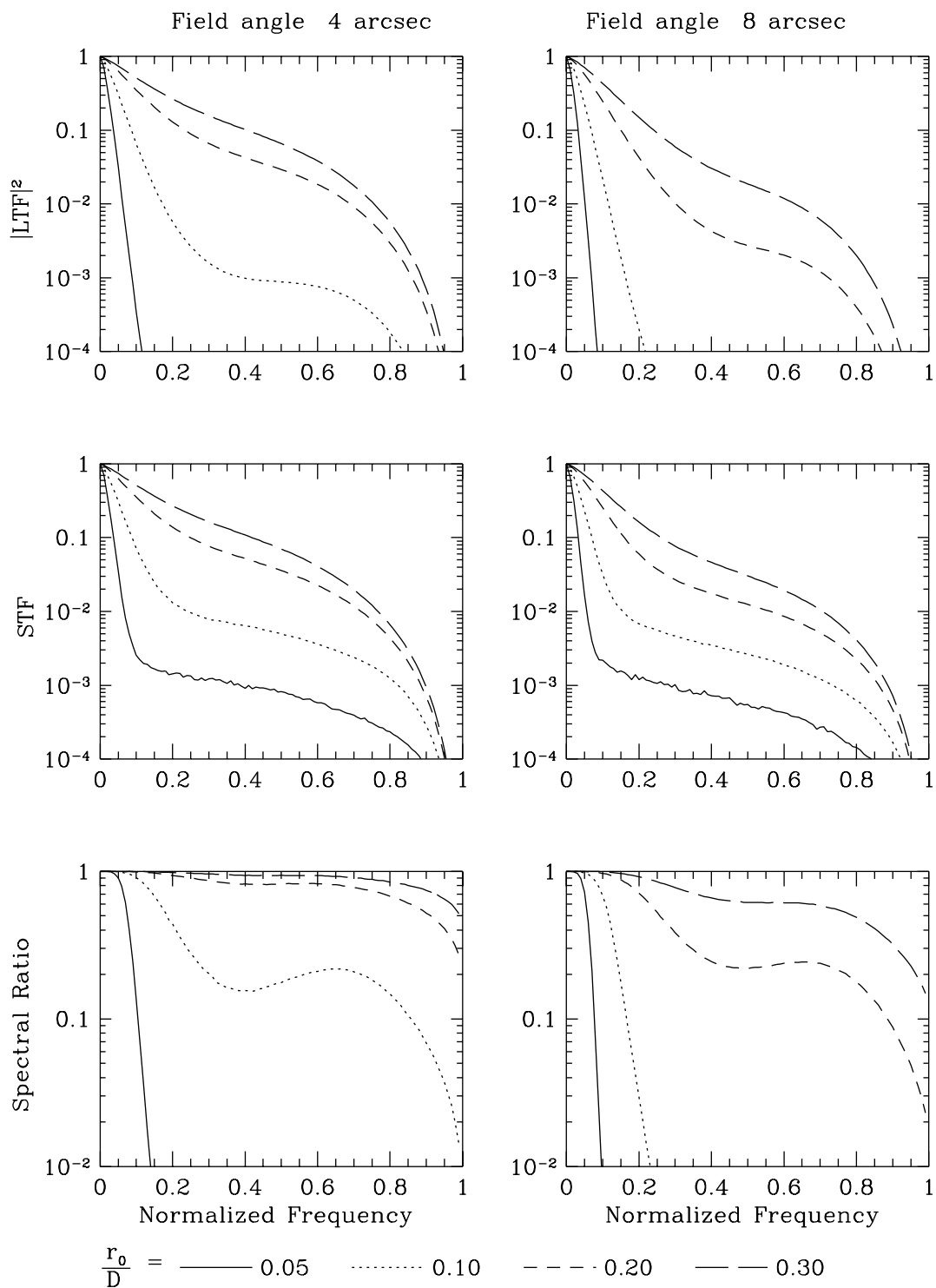


Figure 3.3: Same as in Fig. 3.2 for the field angles of 4 arcs and 8 arcs.

3. SPECKLE INTERFEROMETRY USING ADAPTIVE OPTICS CORRECTED DATA

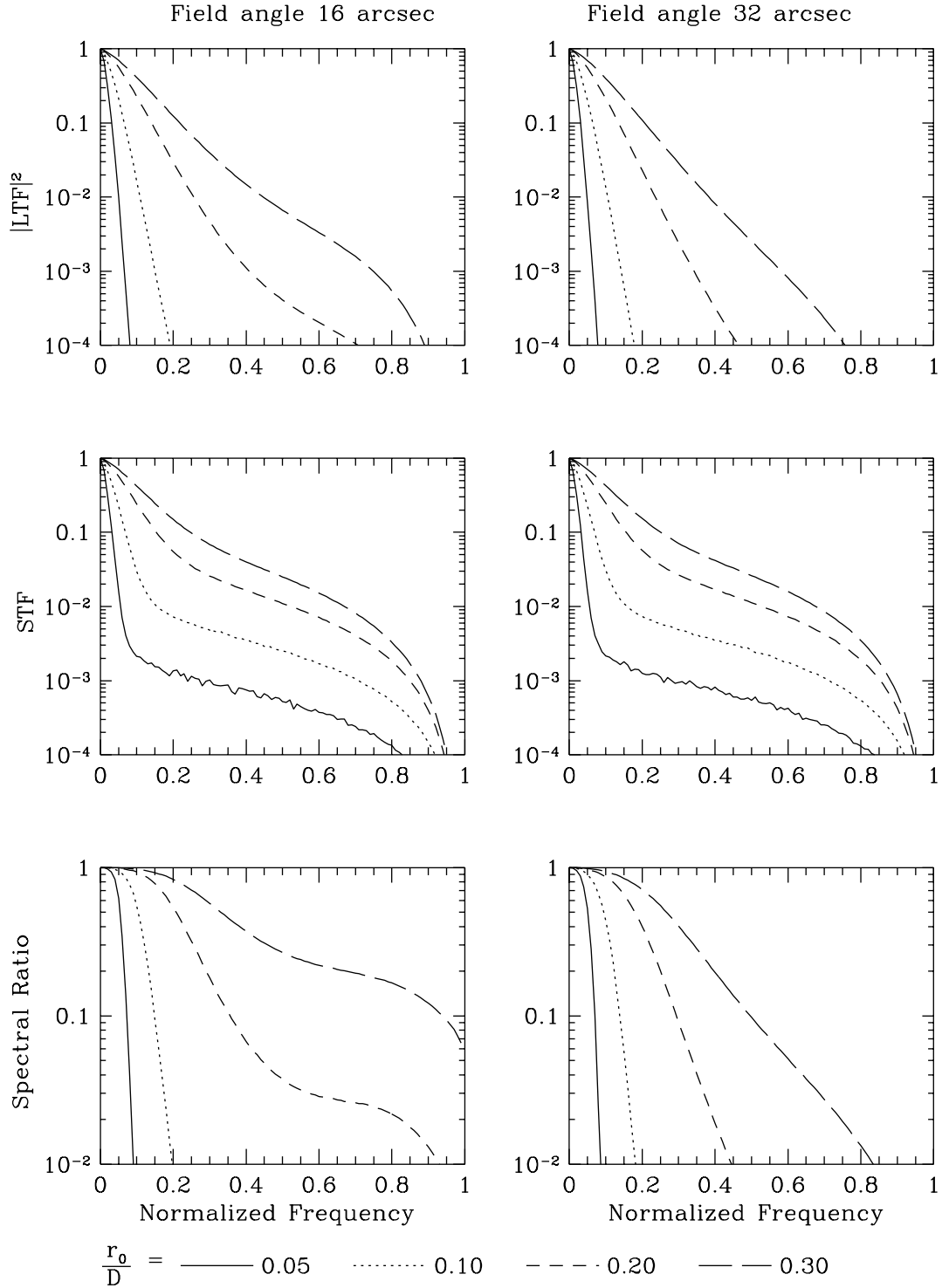


Figure 3.4: Same as in Fig. 3.2 for the field angles of 16 arcs and 32 arcs.

2. The greater the angular distance between lockpoint and line-of-sight, the lower the high-frequency tails.
3. The typical shape of an adaptive optics transfer function can be seen in the squared long exposure transfer function, $|\text{LTF}|^2$, at the lockpoint. A diffraction limited core, represented by the high-frequency tail, and a seeing limited halo, represented by the fast drop-off at low frequencies. In excellent seeing conditions, the diffraction limit is almost reached.
4. The STF high-frequency tails are always higher than the $|\text{LTF}|^2$ high frequency tails.

3.5.2 Comparison to observed transfer functions

A comparison of models with observed data is only possible with observations of a star. A data set taken at the 3.6 m telescope of the ESO with the adaptive optics system ADONIS (Bonaccini *et al.*, 1997) in February, 1996 was used in this case. The observed object was α -Orionis, which is resolved with this telescope. The squared visibility function describes the attenuation of the power spectrum due to the fact that the the star was resolved, and is for a uniform disc equal to (Weiner *et al.*, 2000)

$$V(x) = \frac{2J_1(2\pi r x)}{(2\pi r x)}, \quad (3.38)$$

in one dimension. Here, J_1 is the Bessel function of first order, r is the radius of the star in arcs and x is the spatial frequency in arcs^{-1} . The visibility function for this particular observational run was theoretically calculated and taken into account in the models. Unfortunately, little is known about the actual performance of the ADONIS system in this particular case. This is the reason why the AO performance parameters β_i , which are necessary as input for equations (3.19) and (3.30), had to be estimated from Fig. 3 in Harder & Chelli (2000).

The result is presented in Fig. 3.5. One possible reason for inaccuracies present is that the central obscuration of the telescope had to be taken into account. This could only be done in the first order approximation that the atmospheric covariances $\langle a_j a_{j'} \rangle$ as computed by Noll (1976) do not change. His computations

3. SPECKLE INTERFEROMETRY USING ADAPTIVE OPTICS CORRECTED DATA

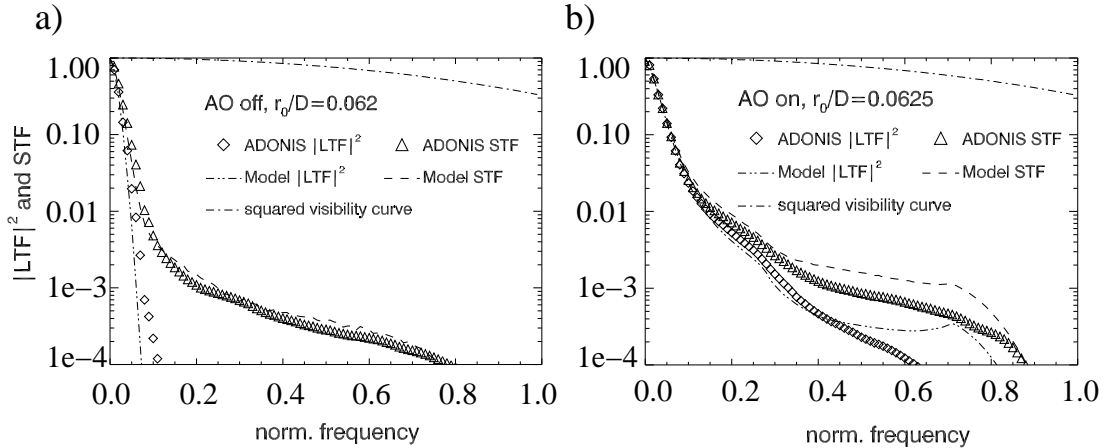


Figure 3.5: The result of a direct comparison between measured and modeled data. In figure a), ADONIS was turned off. The atmospheric conditions have been estimated to a value of $r_0/D = 0.062$. In b), ADONIS had been turned on.

assumed an unobstructed, annular apertures on which Zernike polynomials are orthonormal functions. However, Zernike polynomials are not orthonormal on an aperture with a large central obscuration such as that present at the 3.6 m telescope of the ESO, so that presumably the coefficients cannot be easily calculated. Nevertheless, the fit of the calculated model for the long exposure and the speckle transfer functions of ADONIS to the observational data is satisfactory, if one takes into account that the β_i were only estimated.

3.5.3 Speckle imaging of solar data

The modeled STFs were applied to speckle images of the solar granulation, taken in the Fraunhofer G-Band (430.5nm) at the German vacuum tower telescope at the Observatorio del Teide in Spain. The data were acquired using KAOS.

The calibration of Fourier amplitudes must be done within subfields of the size of the isoplanatic angle. Additionally, the knowledge of the viewing angle of the wavefront sensor is needed, which is marked as rectangle in Fig. 3.6. The reason is the need to know the angular distance of each subfield from the lockpoint in order to apply the correct model for the STF (see Sect. 2.4.1).

The value of r_0 was approximately 16 cm and is estimated by computing a weighted least-squares fit of model to data spectral ratio within two iterations

(see Sect. 2.4.2). The model for the spectral ratio was created by calculation of the quotient in equation (2.35) using the transfer functions as calculated from equations (3.19) and (3.30). The fit can be seen in Fig. 3.7 for different angular distances from the lockpoint. Deviations at higher frequencies become apparent because the measured transfer functions (both $|LTF|^2$ and STF) drop off at low frequencies in most cases. This behavior makes the spectral ratio sensitive to noise and a fit at high frequencies somewhat uncertain. This is negligible because it is the drop-off at low frequencies that delivers the necessary information about the values of r_0 .

3.6 Conclusions

New analytical models for transfer functions of AO systems have been presented in this Chapter. These models are capable to describe the long exposure transfer function and the speckle transfer function of an arbitrarily correcting AO system. The necessary parameters can be extracted from the data that the wavefront sensor can record automatically while measuring the wavefront aberrations introduced by Earth's atmosphere. In addition, the models can take into account an arbitrary amount of viewing angles to model the decreasing performance of an AO system with increasing angular field angle from the lockpoint. Furthermore, because of their generality, these models will be capable of generating transfer functions for yet to be seen MCAO systems because of the way the field dependence of the correction was taken into account.

The accuracy of the transfer functions is satisfactory both, when comparing them to the measurements of α -Orionis with ADONIS, the adaptive optics system of the 3.6 m telescope of the ESO, and to the measured spectral ratios computed from images of the solar surface.

3. SPECKLE INTERFEROMETRY USING ADAPTIVE OPTICS CORRECTED DATA

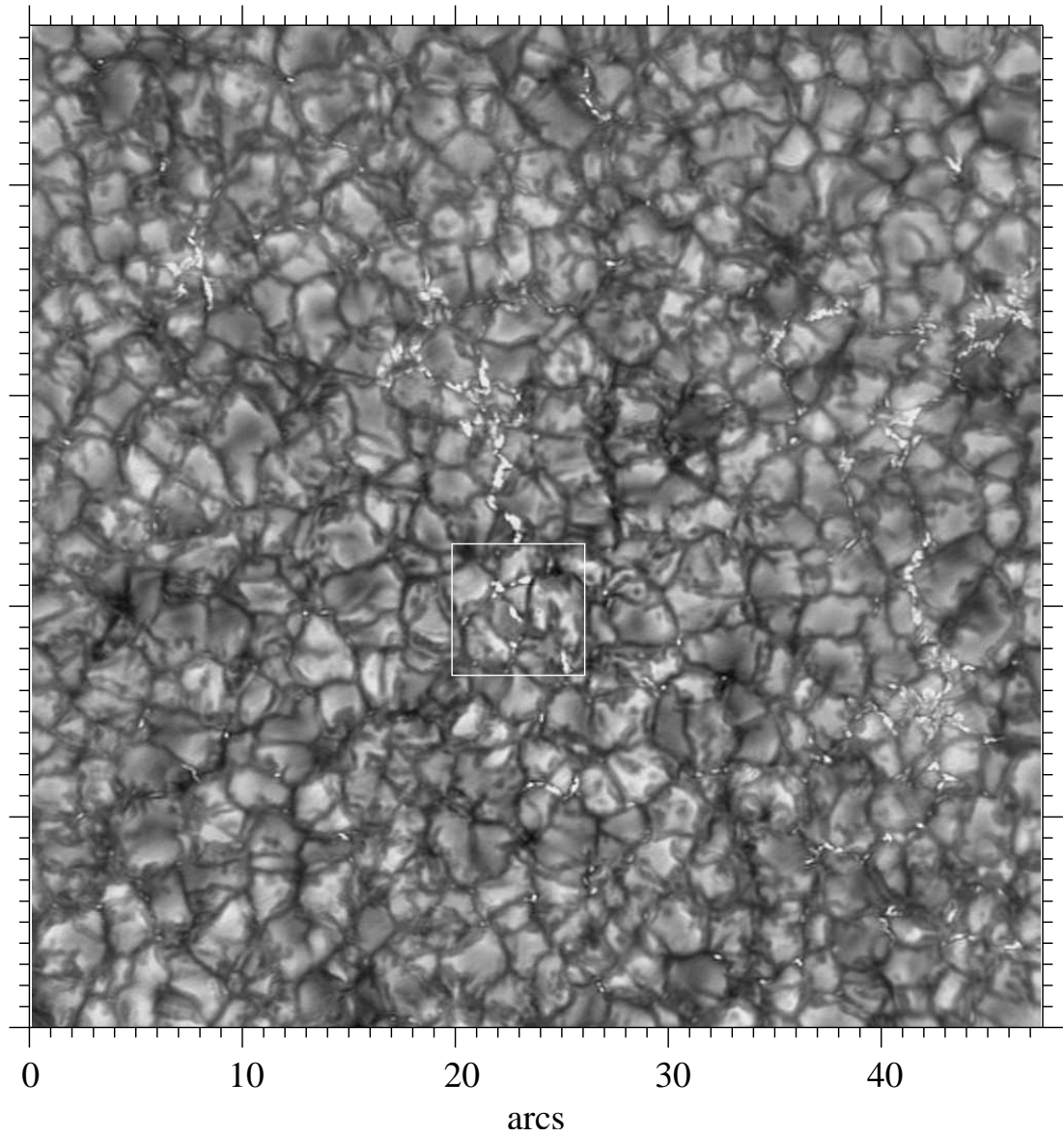


Figure 3.6: Sample speckle reconstruction of solar granulation in the Fraunhofer G-Band. The relevant short exposed speckle images were acquired using KAOS. The lockpoint has been indicated by the rectangle.

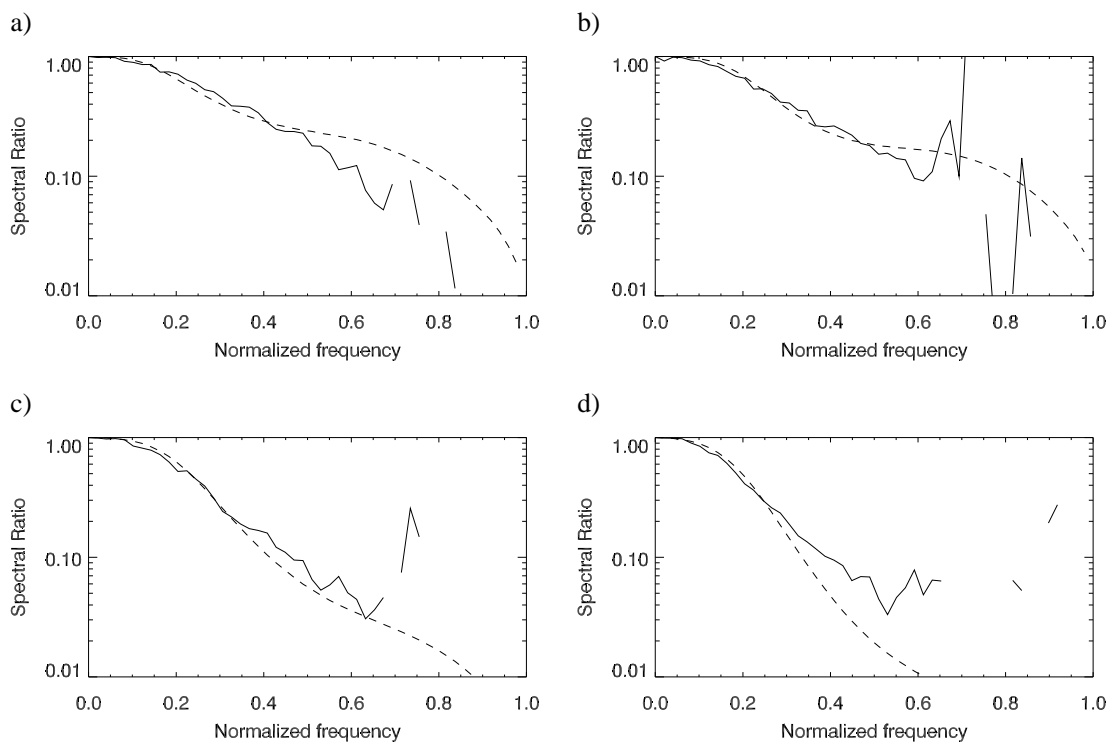


Figure 3.7: The spectral ratio at different viewing angles. In all curves, the solid curve is the measured data, the dashed curve its best fit using the fitting algorithm described in Sect. 2.4.2. The viewing angles are a) 0'', b) 4'', c) 12'' and d) 36''.

3. SPECKLE INTERFEROMETRY USING ADAPTIVE OPTICS CORRECTED DATA

Chapter 4

PSF reconstruction and image deconvolution

Although the optical setup to gather the data necessary to use speckle interferometry is often very simple, there can be reasons why a reconstruction using these algorithms cannot be done. This is the case if there is not enough light to expose the camera only a few milliseconds in order to freeze one realization of the atmosphere. Long exposures are very difficult to handle but yet can also be reconstructed if the instantaneous point spread function of the system is known, a process known as deconvolution. In this Chapter, the following situation is considered: simultaneously with a long exposed image a number of very short exposed images is acquired at a nearby wavelength. The 'true' object intensity can be reconstructed using the short exposed images by means of speckle interferometry. It serves as a 'key' to estimate the PSF of the optical system including atmosphere and telescope. Under these conditions, the reconstruction of the PSF can be achieved by an iterative process the details of which are presented in this Chapter.

4.1 Reconstruction of the PSF from a speckle reconstruction

The estimation of a PSF from data poses a difficult problem because even slight inaccuracies in the PSF can have a big effect in a deconvolution process. Real data suffers from noise which makes a straight forward approach impossible. However, under the assumptions that

1. the static PSF of the system is well known.
2. the PSF is positive semi-definite.
3. the width of the PSF of the optical system is approximately r_0/λ

an iterative procedure to estimate the system's PSF can be formulated.

Again, the starting point is equation (2.5). The OTF could be estimated by a division in the Fourier domain:

$$\text{OTF}(\vec{s}) = \frac{\tilde{I}(\vec{s})}{\tilde{O}(\vec{s})}. \quad (4.1)$$

Using a single short exposed frame of the speckle burst, the Fourier transformation of the quotient in equation (4.1) leads to the instantaneous PSF if no noise or zero points are in the Fourier transform of the object.

In general, especially when noise is present, very small values or even zero points can and do occur and lead to large or undefined values in the OTF and thus an oscillatory PSF. This is the reason why care must be taken to exclude potentially problematic values, i.e. values which are strongly biased by noise. The signal-to-noise ratio (SNR) for each frequency point proved to be a useful tool to create a mask $M(\vec{s})$ with

$$M(\vec{s}) = \begin{cases} 1 & \text{if } \text{SNR}(\vec{s}) > 2 \\ 0 & \text{if } \text{SNR}(\vec{s}) \leq 2 \end{cases} . \quad (4.2)$$

The noise was estimated from the average value of the power spectrum at those frequency points that lie beyond the diffraction limit D/λ .

4.1 Reconstruction of the PSF from a speckle reconstruction

Further constraints can be applied in order to regularize the PSF. The use of physical constraints is common in blind deconvolution algorithms (e.g. [Jefferies & Christou \(1993\)](#)). On the one hand, one can make an assumption about the telescope itself. The modulation transfer function $MTF = |OTF|$ delivers a measure for the maximum power at each frequency that can be transferred by the specific telescope. This gives the possibility to limit the Fourier amplitudes to reasonable values in the spatial frequency domain. On the other hand, the value of r_0 plays a major role for the size of the PSF and can be applied as support constraint in the spatial domain. As seen in equation (2.31), the OTF is limited by the fast drop-off due to the exponential term. In the spatial domain this leads to a broadening of the long exposure PSF, which can be approximated by a Gaussian. The width of the long exposure PSF is related to r_0 and delivers a constraint in the spatial domain. Additionally, the PSF must be positive semi-definite.

With these constraints, the PSF estimation algorithm proceeds as following.

1. Estimation of the Gaussian which approximates best the long exposure PSF and thus set up the spatial constraint.
2. Set up frequency domain constraint by loading telescope MTF.
3. Calculation of $\tilde{I}(\vec{s})$ and $\tilde{O}(\vec{s})$.
4. Calculation of $OTF(\vec{s})$ according to equation (4.1) at frequency values for which $M(\vec{s}) = 1$. Set the values at the remaining frequencies to zero.
5. Compute the $PSF(\vec{x})$ by Fourier transforming $OTF(\vec{s})$.
6. Apply spatial domain constraints.
7. Compute the $OTF(\vec{s})$ by Fourier transforming $PSF(\vec{x})$.
8. Apply frequency domain constraints.
9. Repeat (5)-(8) until the number of zero points detected in the spatial domain is constant.

The algorithm typically converges after 3-4 iterations, and yields the estimate for the instantaneous PSF representing the optical system 'atmosphere and telescope'.

4. PSF RECONSTRUCTION AND IMAGE DECONVOLUTION

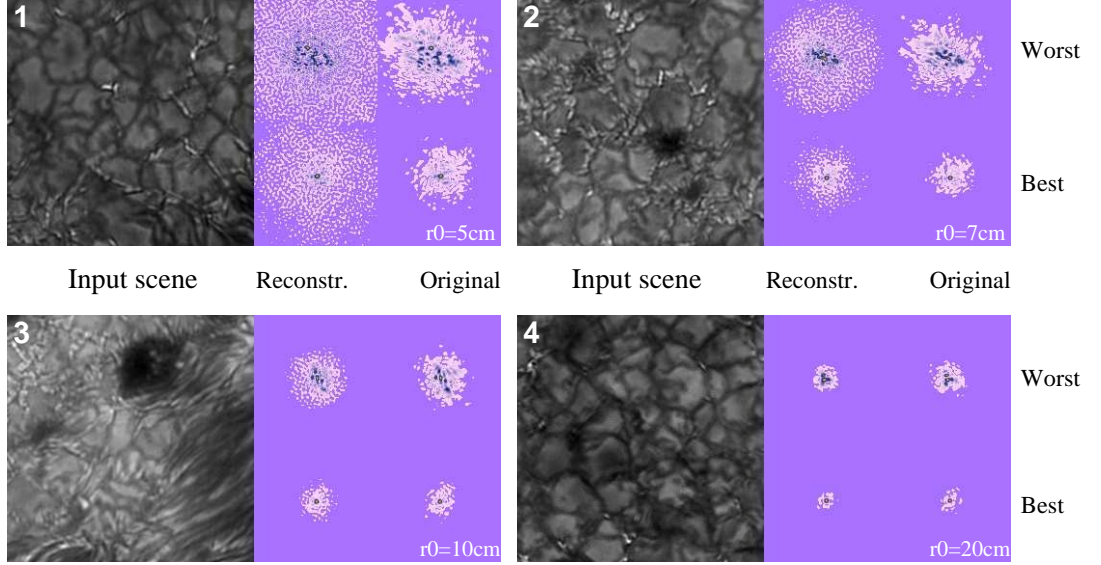


Figure 4.1: Sample PSF reconstructions. Different scenes of the solar surface were used: 1. granulation with bright points 2. pore 3. penumbra of a sunspot 4. quiet granulation. The best and worst cases of a reconstruction for the indicated Fried parameters r_0 are shown in combination with the relevant input PSF.

4.1.1 Tests on simulated data

The algorithm was tested using data showing different scenes on the solar surface (see Fig. 4.1). The images were convolved with simulated atmospheric PSFs and biased with noise. The PSFs were generated assuming Kolmogorov statistics and using values of r_0 that vary in the range between 5 and 20 cm. The simulated exposure time was 10 ms. In Fig. 4.1 for each simulated r_0 the best and worst PSF reconstruction is shown. The error metric is η , the least squares distance of reconstruction to original, which were normalized to the maximum intensity in each image:

$$\eta = \frac{1}{P} \sum_{n=0}^P (\|\text{Reconstruction}_n\|_{\max} - \|\text{Original}_n\|_{\max})^2 \quad (4.3)$$

where P is the total number of pixels in the image and "Reconstruction" and "Original" are in this case the reconstructed PSF and the original PSF used to distort the image, respectively. The maximum norm, indicated with $\|\cdot\|_{\max}$,

4.1 Reconstruction of the PSF from a speckle reconstruction

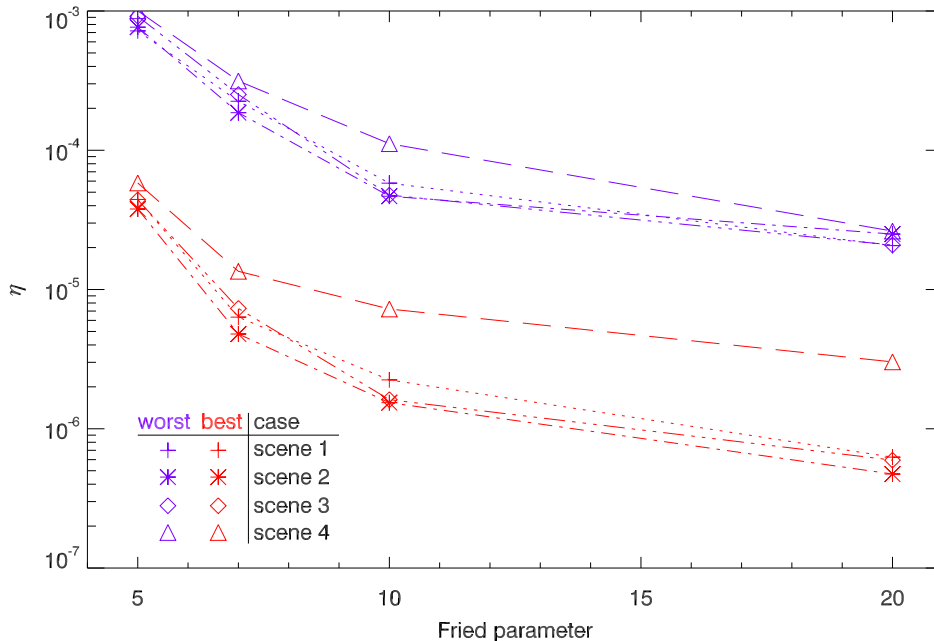


Figure 4.2: Best and worst values for η for different scenes and values of r_0 .

was used because in this case the sum of squared relative deviations as error metric is more sensitive to the fine structure in images than the sum of squared absolute deviations. The measure η is equivalent, although slightly different, to the measure D^2 used in the work of Mikurda & Von Der Lühe (2006). It cannot be expected that the PSF can be reconstructed with full photometric accuracy in the presence of noise. However, the fine structure of the PSF is important in order to be able to deconvolve the image to obtain the highest possible resolution. In Fig. 4.1, the major part of the fine structure is recovered, whereas especially for bad seeing (small values of r_0), the halo structure is not reconstructed well, showing noise in the outer parts. These deviations from the original PSF will reduce the accuracy of a deconvolution.

The values of η for the best and the worst cases are shown in Fig. 4.2 for each r_0 . It can be seen that with increasing r_0 the reconstruction accuracy becomes better. Additionally, from the accuracy for the different scenes one can see that the lower the high frequency signal in the image (scene 4) the worse the recon-

4. PSF RECONSTRUCTION AND IMAGE DECONVOLUTION

struction, which can be attributed to the lower SNR at higher frequencies. Thus, the PSF estimation yields better results on scenes which contain high frequency information.

4.2 Deconvolution using the maximum entropy method

Looking at the image creation process, a deconvolution is theoretically simply the division of the observed image and PSF in the Fourier domain:

$$\tilde{O}(\vec{s}) = \frac{\tilde{I}(\vec{s})}{\text{OTF}(\vec{s})} \quad (4.4)$$

However, problems like oscillatory behavior of the solution will occur if noisy data is treated this way. The reason are small values or even zeros in the OTF which lead to an over-amplification of the according frequency according to equation 4.4. Many approaches have been suggested to overcome this problem. A straight forward linear approach to deconvolution is the application of a Wiener filter which is usually defined as

$$\text{WF}(\vec{s}) = \frac{O(\vec{s}) - \text{Noise}(\vec{s})}{O(\vec{s})} \quad (4.5)$$

in combination with the division in equation (4.4) to simultaneously reduce the noise $\text{Noise}(\vec{s})$ in the data. Here, $\text{Noise}(\vec{s})$ could be estimated as the average value of power beyond the diffraction limit or from a power spectrum of flat data, which yields frequency dependent noise information. However, a Wiener filter is sometimes not optimal in the sense that information can get lost that could be retained because of a coarse noise estimation. For this reason, other methods have been developed for the deconvolution of data, one of which is the maximum entropy method (MEM). Here, a brief introduction is given based on [Narayan & Nityananda \(1986\)](#) and [Hollis *et al.* \(1992\)](#). The MEM inverts the convolution in equation (2.4) under constraints. The convolution can be expressed for the

4.2 Deconvolution using the maximum entropy method

discrete case without noise as

$$I_k = \sum_{i=1}^N O_i \text{PSF}_{k,i} \quad k = 1, \dots, M. \quad (4.6)$$

M corresponds to the number of pixels on the detector and N is used to approximate the convolution integral. Without loss of generality, it can be assumed that

$$\sum_{i=1}^N O_i = 1. \quad (4.7)$$

These are in fact $M + 1$ constraints. If $M + 1 < N$, the problem is ill-conditioned and a solution is not unique. The MEM chooses from the set of images which fulfill the constraints in equations (4.6) and (4.7) the one non-negative image, which shows the maximum number of ways this image could have arisen. This is achieved by maximizing the entropy function

$$S(0) = - \sum_{i=1}^N O_i \ln(O_i). \quad (4.8)$$

The particular distribution of intensity O_i (which is now interpreted as a probability distribution) can be found by use of Lagrange multipliers. The result is the Maxwell-Boltzmann distribution which arises in the same way as in statistical mechanics; the multiplicity of all states is one. In combination with the constraint in equation (4.6) this leads to

$$\sum_{i=1}^N (\text{PSF}_{k,i} - I_k) \exp \left(- \sum_{s=1}^M \lambda_s \text{PSF}_{s,i} \right) = 0 \quad k = 1, \dots, M. \quad (4.9)$$

Here, the λ_s are the Lagrange multipliers. Obviously, the M equations for the λ_s are implicit and nonlinear and require an efficient algorithm. Several methods come into mind like fixed point or gradient methods (Press *et al.*, 1992). Here, a MEM algorithm suggested by Hollis *et al.* (1992, and references therein) for the use of data obtained with the Hubble space telescope is applied to and tested for its performance on solar data.

The original and reconstructed PSFs from the test data used in Sect. 4.1.1

4. PSF RECONSTRUCTION AND IMAGE DECONVOLUTION

were used as input for the algorithm, in particular the PSFs displayed in Fig. 4.1. In addition, the Wiener filtered images are calculated for comparison. The results are shown in Fig. 4.3. In most cases, the MEM algorithm recovers the structure of the original image quite well, most of the time even better than the Wiener filter according to η . However, the value of η is not a good measure to analyze the similarity of two images. The reason is that both absolute intensity and morphology play a role in the assessment of the similarity of two images. However, all metrics based upon squared distances like η are more or less sensitive to deviations in intensity only. The lack of a measure for similarity in morphology in η permits ambiguous results for the quality of a reconstruction.

4.2 Deconvolution using the maximum entropy method

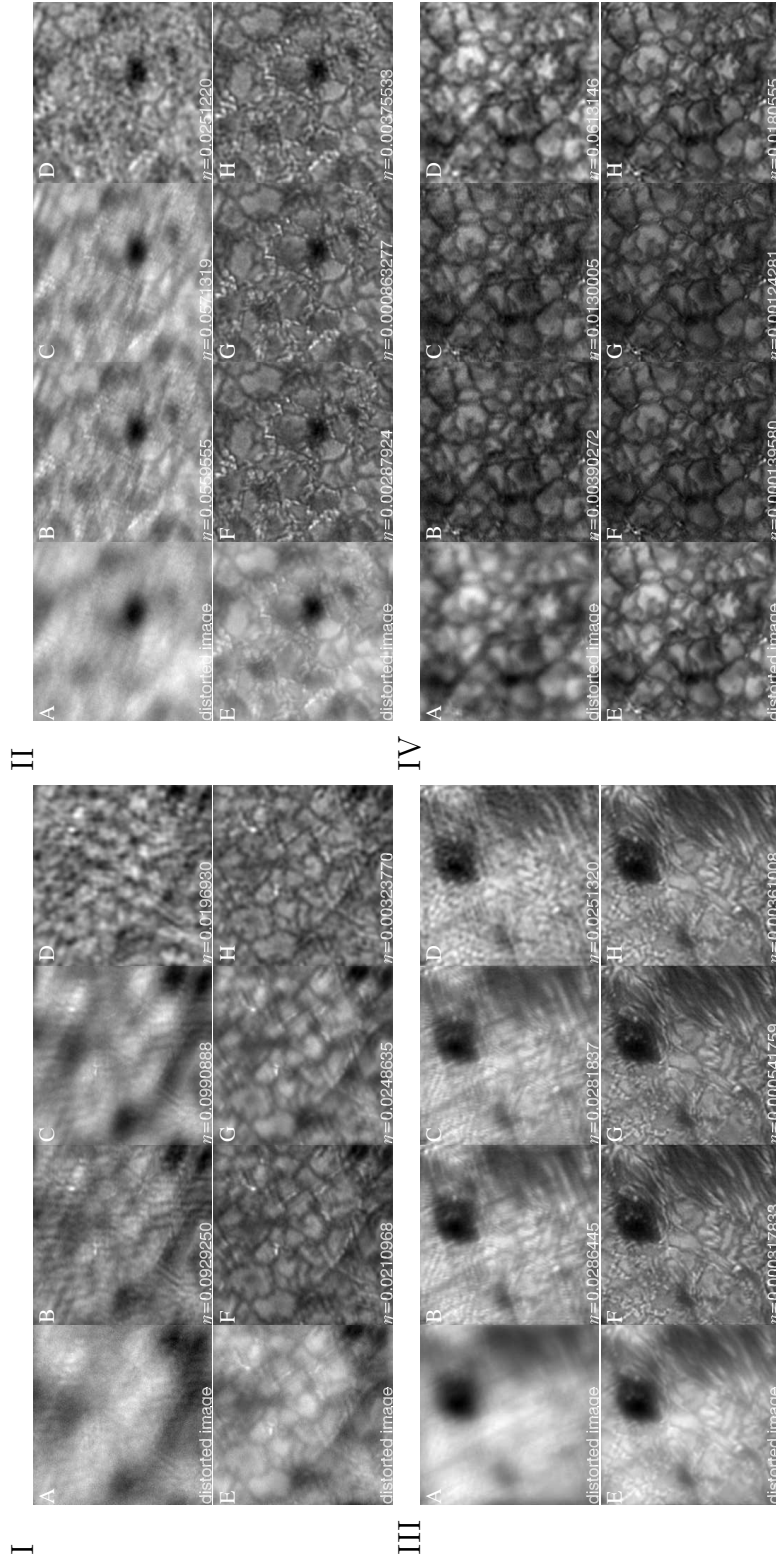


Figure 4.3: Sample data for the worst (A-D) and best cases (E-H) of PSF recovery (see Fig. 4.1) for $r_0 = 5$ cm (I), $r_0 = 7$ cm (II), $r_0 = 10$ cm (III), and $r_0 = 20$ cm (IV). Images A and E are the distorted input images, B and F show the MEM deconvolution using the original PSFs, while C and G show the reconstructions using Wiener filtering. For comparison with the MEM deconvolved images, D and H show the reconstructions using Wiener filtering. The values of η are displayed in the lower left of each image.

4. PSF RECONSTRUCTION AND IMAGE DECONVOLUTION

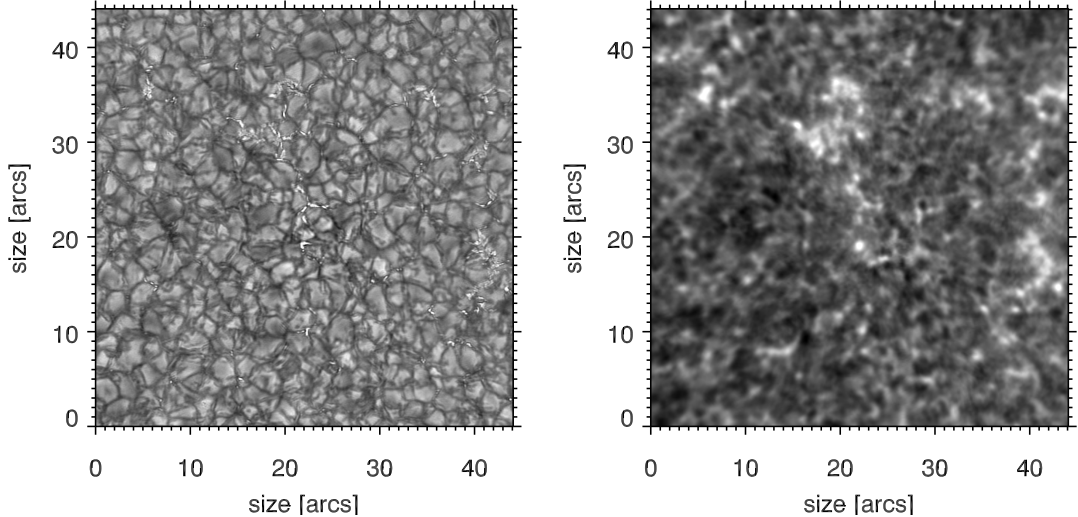


Figure 4.4: Sample of the observational data. Left: speckle reconstructed filtergram of the data acquired at 430.5 nm using 10 ms integration time. Right: filtergram at 393.3 nm using an exposure time of 2 s.

4.3 Application to observational data

The image reconstruction procedure suggested in this Chapter was applied to the observational data gathered at the Vacuum Tower Telescope of the Kiepenheuer-Institut für Sonnenphysik at the Observatorio del Teide on Tenerife, Spain. The data set consists of two simultaneously observed series of filtergrams. One series was taken at the wavelength of 430.5 nm using an exposure time of 10 ms. This suffices to record a series of 100 images within 18 s which was speckle reconstructed later. The other series was observed at the wavelength of 393.3 nm using an exposure time of 2 s, which was necessary because of the low light level in this channel (see Sect. 5.4 for a more detailed description).

To illustrate the quality of the data, a speckle reconstructed image and the simultaneously acquired long exposed image are displayed in Fig. 4.4. The Fried parameter was estimated to $r_0 \approx 13$ cm using the spectral ratio method (see Sect. 2.4.2), and thus sufficiently high to guarantee proper conditions for the reconstruction of the PSF.

For one subfield at the lockpoint and one subfield at the edge of the field-of-

4.3 Application to observational data

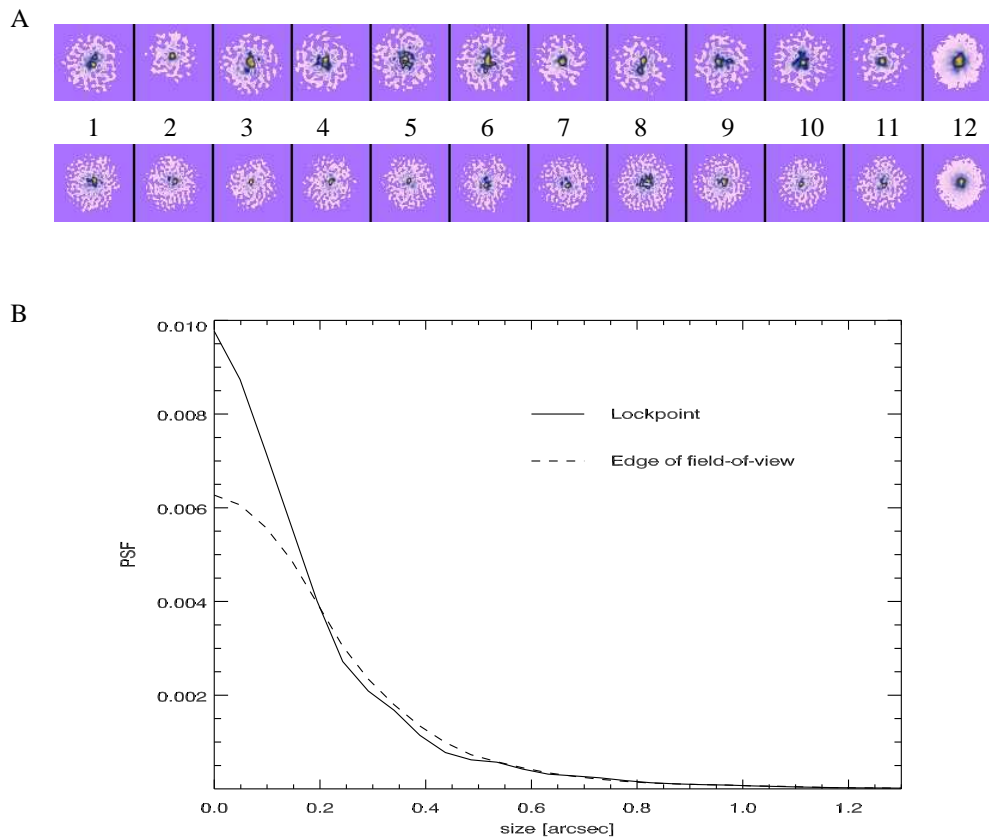


Figure 4.5: A: Instantaneous PSFs (1-11) as reconstructed and mean PSF (12) as used for the deconvolution, at different locations in the field-of-view: edge of the field (top) and lockpoint (bottom). B: The different widths of the mean PSFs. The flatter profile of the PSF at the edge of the field-of-view (FOV) indicates less correction of the adaptive optics in this part of the image.

4. PSF RECONSTRUCTION AND IMAGE DECONVOLUTION

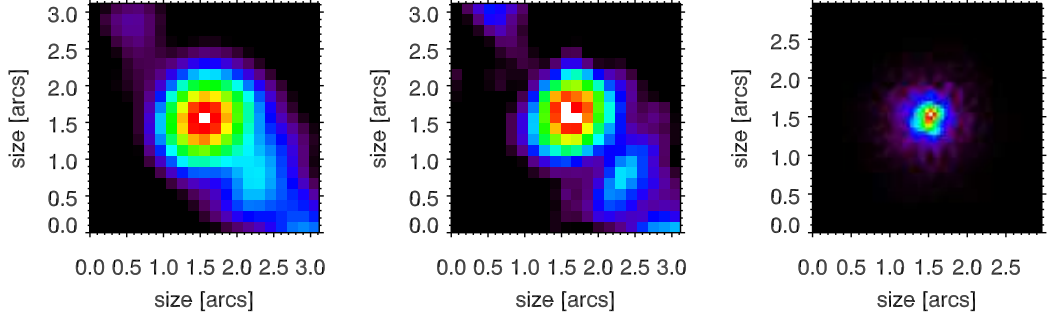


Figure 4.6: Images of a bright point near the lockpoint before (left) and after deconvolution (middle). On the right, the PSF that was used for deconvolution is displayed.

view the reconstructed instantaneous PSFs are displayed in Fig. 4.5, along with their temporal mean used for the deconvolution of the long exposed image (covering 2 s). The radial average of the mean PSF also displayed here demonstrates that the PSFs show the expected behavior: the mean PSF at the well corrected lockpoint of the adaptive optics has a diffraction limited core and a seeing limited halo (e.g. Hardy, 1998). The PSF at the edge of the field-of-view is much flatter, indicating less correction at the edge of the field-of-view. The reason is anisoplanatism (discussed in Chapt. 2.3).

The result of the deconvolution of the long exposed filtergram image is displayed in Fig. 4.6. Here, a point-like structure close to the lockpoint of the adaptive optics system was isolated in original and deconvolved image for comparison. The images show that the resolution of the image is enhanced without introduction of artificial signals. The diameter taken at the position, where the bright point intensity was reduced by a factor of two (FWHM), dropped from $1''.07$ to $0''.90$, the maximum intensity of the deconvolved image was enhanced by about 39%. For comparison, the PSF, which is also displayed, shows a FWHM of $0''.265$.

4.4 Conclusions

The reconstruction of the instantaneous PSF using speckle data is sensible to the quality of the input data, which mainly depends on Fried parameter r_0 and the SNR in the images. Using the algorithm described in this Chapter, the form of the PSF can be recovered well, if favorable conditions are met. These are

1. a high-resolution, noise-free speckle reconstruction,
2. a high SNR at high spatial frequencies, and
3. a Fried parameter of $r_0 = 10$ cm and above.

The accuracy of a PSF reconstruction might be enhanced by a more detailed analysis of signal attenuated by noise. In order to do so, it is important to include additional information regarding the noise distribution in the images during the reconstruction process. This noise may be measured separately because it mainly depends on camera and setup. If the above conditions are met, a deconvolution of the images using Wiener filtering or MEM techniques is feasible and leads to an enhancement of the resolution. It has to be noted again that detailed photometric accuracy is not guaranteed using this method especially when bad seeing was encountered.

However, for morphological studies as they are carried out in this work, the use of these methods is justified as the resolution plays the major role. The processing of the data with the methods described above is used to enhance the small scale structure which is analyzed in the following Chapter.

4. PSF RECONSTRUCTION AND IMAGE DECONVOLUTION

Chapter 5

The connection of photosphere and chromosphere

5.1 Introduction

In this chapter, the data observed with the Vacuum Tower Telescope at the Observatorio del Teide on Tenerife, Spain are analyzed with regard to morphology and dynamics of the small-scale structure encountered in chromosphere and photosphere. Furthermore, the correlation of the fine structure of both layers is investigated. The data consist of short-exposed images in the photosphere and long exposed images in the chromosphere, and have been processed using the methods described in the previous chapters (see Sect. 5.4 for a more detailed description of the data).

The results of the analysis will be compared to recent models for these layers, which have a long history and reached a new level with three-dimensional hydrodynamical and magneto-hydrodynamical models. *Vernazza et al. (1981)* established a static, semi-empirical model of the chromosphere which was rather hot everywhere. However, later, with improving telescope resolution, it became clear from observations that this static model described only the average properties of the chromosphere because it did not include the dynamics of the chromosphere. Time dependent, one-dimensional, radiation hydrodynamical models of the chromosphere could already reproduce certain aspects of the dynamical behavior as

5. THE CONNECTION OF PHOTOSPHERE AND CHROMOSPHERE

present in observations. However, it was a surprise that they showed a cool chromosphere on average disturbed by very hot, intermittent shock waves (Carlsson & Stein, 1992, 1994, 1995). The new three-dimensional non-magnetic radiation hydrodynamical models by Wedemeyer *et al.* (2004) also show a very dynamic and structured temperature distribution in the chromosphere because of interfering shock waves; their model-chromosphere itself is – similar to the one-dimensional model of Carlsson & Stein (1992) – mostly cool.

In recent years, there have been ongoing discussions about what role the acoustic shocks present in the models are playing for the heating of the chromosphere. While the above mentioned models can explain certain aspects of the non-magnetic chromosphere and its dynamical properties, it remains unclear whether the acoustic shocks present in these models are the main driver for the energy transfer from the photosphere upwards to the chromosphere and corona (Fossum & Carlsson, 2005).

It is evident that radiation hydrodynamical models do not reflect the whole reality on the Sun: shocks occurring in the models often produce high temperature peaks that are not observed, and a major physical entity is not taken into account in these models: magnetism¹. It can be argued that the solar chromosphere is partly non-magnetic, so that for those regions there is no need to include magnetic field in the models. However, the models of Carlsson & Stein (1992) and Wedemeyer *et al.* (2004) were criticized because of the unobserved temperature peaks (e.g. Ulmschneider *et al.*, 2005). Wedemeyer *et al.* (2004) model assume *local thermodynamic equilibrium* and a mean ("gray") opacity. In the regions where LTE is valid, the temperature suffices to describe the local ratio of emission to absorption of radiation; the source function is the Kirchhoff-Planck function. The validity of LTE is given if the thermalization length – the distance over which a photon has undergone enough absorption/emission processes to be indistinguishable within the respective distribution – is small compared to the distance over which the gas temperature changes markedly. In the chromosphere, the particle density is so small that LTE cannot be assumed anymore ("Non-LTE"). In atmospheric regions where LTE can still be assumed observations are well in line with the models in question (Leenaarts & Wedemeyer-Böhm, 2005). Observations

¹This situation has improved lately (Schaffenberger *et al.*, 2005).

which support the view of the non-magnetic chromosphere as highly intermittent phenomenon dominated by shock waves will be described in this chapter.

The role of magnetic fields in the heating of the chromosphere is still unclear, but there are many considerations which lead to the impression that they could considerably attribute to the energy transfer (e.g. [Jefferies *et al.*, 2006](#)). In this chapter, the connection of small photospheric magnetic elements, manifested as bright features in the Fraunhofer G-Band, to their chromospheric counterparts is analyzed in order to shed some light on the possible mechanisms which are involved to heat the chromosphere.

The first two sections will inform about the most recent observations and models for the fine structure in photosphere and chromosphere. In the third section, the observational data gathered and evaluated in this work are described. The last section contains the results of the analysis regarding the connection between both atmospheric layers.

5.2 Fine structure in the photosphere

The solar photosphere has been and still is subject to intense research. The most obvious small-scale pattern is a cell like structure called granulation, with cell sizes of on average 1300 km and a life time of about 6 min ([Stix, 2002](#), and references therein). It is the intensity signature of solar convection. The small-scale structures of interest for this work, called photospheric bright points, belong to the smallest detectable objects with solar telescopes of the current generation. Bright points were discovered first in the photospheric continuum by [Dunn & Zirker \(1973\)](#). Many observations followed to investigate their behavior, especially with regard to their connection to small-scale patches of magnetic field that were detected earlier and show strengths of one kilo-Gauß ([Beckers & Schröter, 1968](#)). The bright points seem to accumulate at the boundaries of cells that are several times larger than normal granulation ([Muller & Roudier, 1984](#)). The large cells are known as *supergranules* ([Leighton *et al.*, 1962](#)); their internal flows advect magnetic fields that are concentrated at the cell boundaries by this mechanism. The cell boundaries show up as the so-called magnetic network ([Chapman & Sheeley, 1968](#); [Livingston & Harvey, 1969](#)), while the cell interiors are largely

5. THE CONNECTION OF PHOTOSPHERE AND CHROMOSPHERE

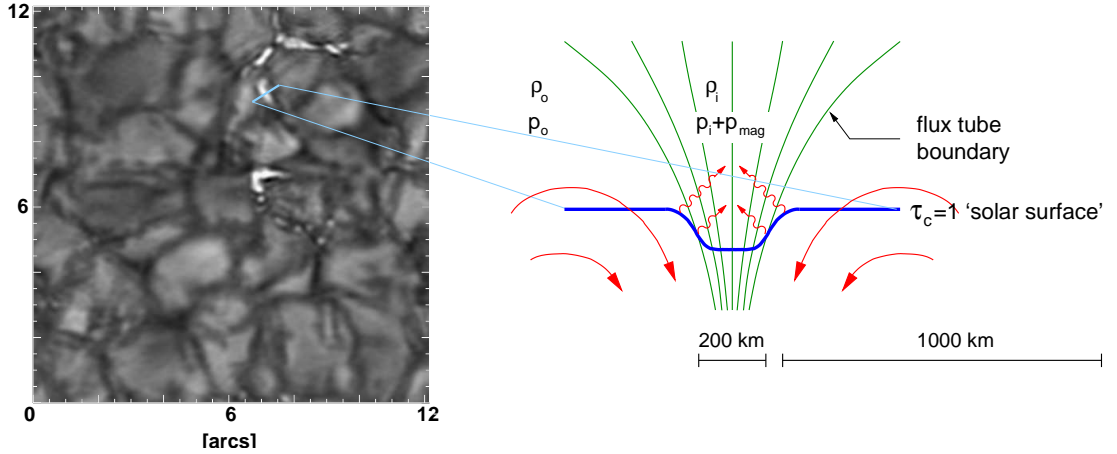


Figure 5.1: Observations of G-band bright points. The sketch shows the model structure of a magnetic flux tube (courtesy of O. Steiner).

non-magnetic because of this 'flux expulsion'. The same mechanism takes place on the smaller scale of the granulation, so that the photospheric bright points are found in the vast majority within intergranular lanes. Muller & Roudier (1984) found that the bright points can be detected especially well in the Fraunhofer G-band (430.5 nm), a fact that initiated extensive observations at this wavelength up to the present time (recent works are e.g. Rouppe van der Voort *et al.*, 2005; Wiehr *et al.*, 2004). Fig. 5.1 shows several photospheric bright points.

Today, it is widely accepted that the origin of photospheric bright points are probably small, strong-field magnetic elements. These can be modeled in connection with flux tubes embedded in the convective flow (e.g. Steiner *et al.*, 1996). The reason for their enhanced brightness is the magneto-hydrostatic equilibrium of the flux tube interior and the surrounding medium: if z denotes the geometrical height increasing with increasing radial distance from the solar core, in equilibrium the total pressure must be equal inside and outside. due to magnetic field strength $B(z)$ and gas pressure $p_i(z)$ inside the flux tube must be equal to the gas pressure $p_o(z)$ in the vicinity outside of the flux tube at all heights (Fig. 5.1),

$$B(z)^2/8\pi + p_i(z) = p_o(z). \quad (5.1)$$

The magnetic field inside the tube hampers the convection and thus the energy

5.2 Fine structure in the photosphere

transport upwards, resulting in a decreased interior temperature. However, the temperature equilibrium with the surroundings of the tube is quickly reinstated in thin tubes (< 500 km) because of lateral radiative energy transport. Thus, keeping in mind the ideal gas equation, the reduced gas pressure inside the flux tube at height z stems from a decreased density because of the temperature equilibrium. The reduced density results in a reduced opacity within the tube with respect to the opacity outside. This leads to a (geometrical) depression Δz of the optical depth isosurface $\tau_c(z) = 1$ in the tube¹. This so called *Wilson depression* means that photons escape from geometrical deeper, hotter layers. A *hot wall* at the circumference of the flux tube becomes exposed and radiates into its interior, a process that can be observed especially well at the limb due to the inclined viewing angle with respect to the flux tube (e.g. [Carlsson et al., 2004](#)). Further details are described in [Spruit \(1976\)](#).

The reason for the enhanced visibility of the photospheric bright points in the G-band lies mainly in the dissociation of CH that "weakens the CH-lines within the magnetic element, thus acting as a leverage for the contrast" ([Steiner et al., 2001](#)). The dissociation is most likely due to the hot wall radiation ([Langhans et al., 2004](#)). However, it has been found that not every magnetic element has a bright point as counterpart in the G-band, and that there exist brightenings on the edges of certain bright, rapidly expanding granules ([Berger & Title, 2001](#)). In any case, [Berger & Title \(2001\)](#) state that "all G-band bright points, properly distinguished from granulation brightening, are magnetic in nature" within the best spatial resolution of their magnetograms (≈ 0.3 arcs).

The size of the photospheric bright points have been found to be between 100-300 km ([Wiehr & Puschmann, 2005](#); [Wiehr et al., 2004](#)) and show horizontal motion that is on average 1.4 km/s, although velocities of up to 3 km/s can be reached ([Muller et al., 1994](#)).

The significance of the photospheric bright points is that their horizontal movement could explain the radiative losses (and thus its temperature) in the chromosphere and corona, which is most likely due to dissipation of magneto-hydrodynamic waves generated by photospheric plasma motion perturbing mag-

¹ $\tau_c(z) = 1$ is the isosurface at which the emerging intensity has dropped to $1/e$ times its original value.

5. THE CONNECTION OF PHOTOSPHERE AND CHROMOSPHERE

netic flux tubes (Jefferies *et al.*, 2006, e.g.). The details of the processes involved are unclear, and there is an ongoing discussion up to today about whether the main contribution to chromospheric heating comes from solely hydrodynamic or rather *magneto*-hydrodynamic waves (Fossum & Carlsson, 2005; Socas-Navarro, 2005; Ulmschneider *et al.*, 2005). Other theories concerning the open question of the heating of the chromosphere have been ruled out lately by Socas-Navarro (2005), such as dissipation of magnetic field reconnection as suggested by Parker (1988) or electric currents (Goodman, 2000, e.g.).

5.3 Fine structure in the chromosphere

The name chromosphere ('colored sphere') derives its name from the colorful view that can be seen just after the beginning and before the end of a total eclipse. Because of the obscured Sun, one sees e.g. the H α line (656.3 nm) or the Ca II K line (393.3 nm) in emission. At these wavelengths, the solar atmosphere is still opaque at a geometrical height where it is transparent in the continuum – even for a tangential line of sight. For this reason, the hot solar chromosphere can be seen in the lines whereas only the dark and cool space to the continuum wavelengths. Taking images at the wavelength of the Ca II K emission feature (see Fig. 5.2) reveals a structured chromosphere: a chromospheric emission network can be seen, whose cell boundaries coincide with the cell boundaries of the supergranular cells in the photosphere (Simon & Leighton, 1964).

However, deducing the thermal structure of the solar chromosphere remains complicated by the limited number of diagnostics and the difficulties in interpreting them. Unfortunately the simplifying assumption of LTE is not valid for the emission peaks in the cores of these lines. Rather, non-LTE effects must be taken into account for a realistic description of chromospheric plasma and radiation fields. This is not only a problem for the interpretation of observations of these spectral features, but also for the numerical modeling of the chromosphere.

Filtergrams with low spatial resolution in the Ca II K_{2v} emission show a "bifurcated" chromosphere, featuring a net-like pattern which, when observed at high spatial resolution, falls apart into mostly circular bright points, also called grains or network bright points (NBP). This can be seen in Fig. 5.3 (middle).

5.3 Fine structure in the chromosphere

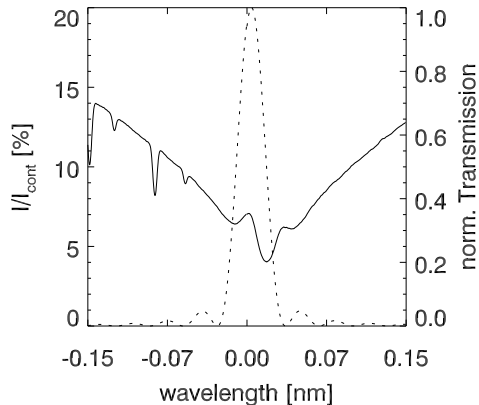


Figure 5.2: The calcium line around 393.35 nm (Neckel, 1999) (thin solid), plotted together with a theoretical Lyot filter transmission curve with 0.03 nm FWHM. The Ca II K emission features express in the local maxima around 0 nm (K_{2V}) and 0.035 nm (K_{2R}).

At this wavelength, the grains, that are located at the edges of supergranular cells, are substantially brighter than the cell interior, the inter-network. The structures have a very long life time: a supergranular cell can even survive up to 15-30 h (DeRosa & Toomre, 2004; Stix, 2002), and network grains can live for hours. The reason for their enhanced brightening is important to understand chromospheric heating. Several suggestions have been made, however, the most likely energy source is of magneto-hydrodynamic (MHD) nature. The candidates of MHD waves are kink (transverse), longitudinal or torsional waves of or within the magnetic flux tube, and acoustic waves penetrating the flux tube (e.g Hasan *et al.*, 2005, and references therein).

Inter-network structures are, compared to network structures, rather short-lived. Progress has been made to model the intermittent inter-network bright points (IBP) as acoustic waves which form shocks in the chromosphere (Carlsson & Stein, 1992). The recent three-dimensional radiation hydrodynamics model by Wedemeyer *et al.* (2004) shows a mesh-like pattern at chromospheric heights in non-magnetic inter-network regions, consisting of cool regions and hot filaments that are a product of propagation and interaction of oblique shock waves and adiabatic expansion of post-shock regions. The authors argue that the amplitude

5. THE CONNECTION OF PHOTOSPHERE AND CHROMOSPHERE

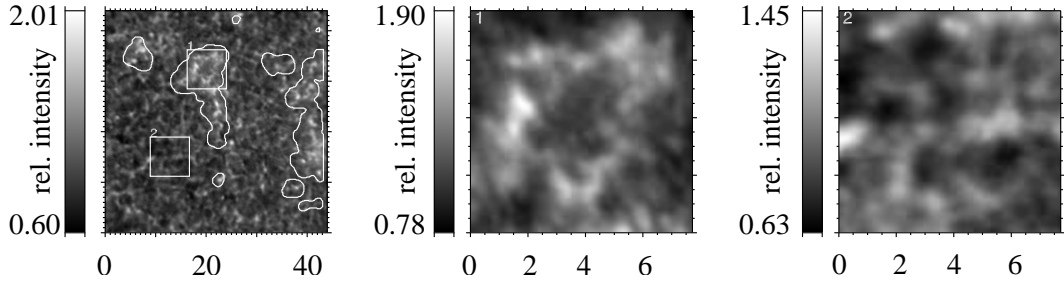


Figure 5.3: A Ca II K image (left) with superimposed network mask M2 (see text) and close-up of the network area 1 (middle) and inter-network area 2 (right). The axes are in arcs.

of the temperature variations in the model chromosphere is somewhat uncertain due to the too simple radiative transfer (gray, LTE). But the pattern is nevertheless representative as it is a product of acoustic waves that are excited in the lower well-modeled layers. The spatial scales of the pattern are comparable to the underlying granulation but the dynamical time scales are much shorter. The IBPs show up at the vertices of these cells and are considered an integral part of the pattern. Collision of two neighboring wave fronts results in compression and heating of the gas at the contact region which shows up as a band of enhanced intensity, making up the "strings" of the mesh-like pattern. At a mesh vertex, however, more than two wave fronts meet, resulting in stronger compression and thus in an intensity higher than the remaining pattern. This behavior is seen in Fig. 5.3 (right).

Mapping the chromospheric small-scale structure of inter-network regions requires both high spatial and temporal resolution. The following analysis will be conducted with a dataset that shows an extraordinary combination of high spatial and spectral resolution.

5.4 Observations and data reduction

A high-resolution image sequence was obtained with the German Vacuum Tower Telescope (VTT) at the Observatorio del Teide on Tenerife, Spain, during UT 8:25–10:21 on April 18, 2005. The telescope was pointed at a quiet area near the disk-center. The field of view is $49'' \times 49''$, showing the chromospheric network and

5.4 Observations and data reduction

inter-network. The dataset consists of images observed in the G-band (430.5 nm) using an interference filter with a FWHM of 1 nm, and, using Lyot filters, in Ca II K (393.3 nm) and H α (656.3 nm) with FWHMs of 0.03 nm and 0.025 nm, taken simultaneously. A sample Ca II K image together with close-ups of a network and an inter-network region is shown in Fig. 5.3. The filter curve of the Ca filter is displayed in Fig. 5.2. The image sequence was taken at a cadence of 10 s and a pixel scale of 0''.1485/px in the Calcium channel and 0''.0486/px in the G-band.

There was a need for telescope adjustments at UT 9:00, separating the sequence into two parts with a gap of 2 min; only the second half of the sequence is evaluated because of its longer duration. The transmission of the Lyot filter is rather poor, thus the light level of the Ca II K line core – being by itself less than 5% of the continuum intensity – was reduced even further, leading to an exposure time of 2 s. The exposure time in the G-band channel was 10 ms which suffices to reconstruct the data using speckle reconstruction techniques (see Chapt. 2 & 3).

All images were corrected for hot pixels and calibrated using the standard procedure of flat-fielding. Additionally, the Ca II K sequence was corrected for the change in mean intensity in each image due to the increasing solar elevation and scaled to the mean intensity of the time series. Finally, the images were deconvolved using the G-band speckle images according to the procedure described in Chapt. 4 resulting in a spatial resolution of 0''.6 and better according to the mean spatially integrated power spectrum. No subsonic filtering was applied to the data sequence.

To analyze the correlation of bright points in the photosphere, the Ca II K and G-band filtergrams were aligned using a target image placed in the primary focus of the telescope. For this purpose the Ca II K target image was scaled to the same scale of the G-band image. It was then rotated and shifted with pixel accuracy to best fit the G-band target image using the least squares difference of the images. The thus determined rotation angle and shift value was then subsequently applied to the whole series of Ca II K filtergrams.

5. THE CONNECTION OF PHOTOSPHERE AND CHROMOSPHERE

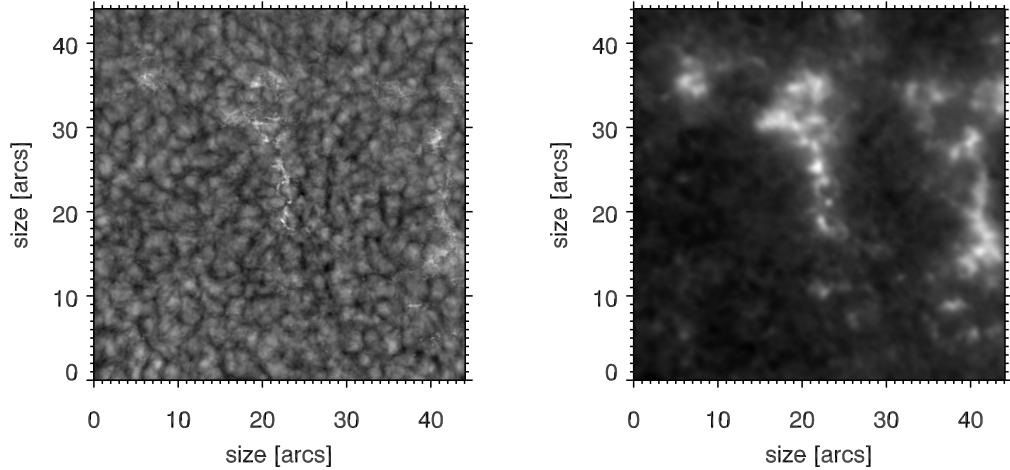


Figure 5.4: The intensity of G-band (left) and Ca II K (right) filtergrams when averaged over time.

5.5 Data analysis

5.5.1 Separation of network and inter-network

As discussed above, the magnetic/non-magnetic nature of network/inter-network motivates the separate analysis of their properties. The temporal average of the observed speckle reconstructed dataset covering about 75 min in the G-band shows that in the network the position of the bright points is rather stable as they do not average out (Fig. 5.4). On the other hand, in the inter-network regions of the average image virtually no bright point is present as their intensity signatures have been smeared out by the averaging process. The Ca II K filtergrams show the same behavior with an even higher contrast (Fig. 5.4).

This observation was the motivation to suggest a new method to separate network and inter-network regions. Commonly, the average image of a time series of filtergrams in a chromospheric line – like Ca II K filtergrams – is used to create a mask for the network by facilitating the temporally stable, enhanced intensity of the network: an intensity threshold is found to separate network from inter-network cells (e.g. Rutten *et al.*, 2004). For the data presented here, such a threshold was determined to $I = 1.029$. A morphological operation to remove

isolated pixels led to a mask M1. However, as this method is based solely on intensity information, proceeding like this can lead to mismatches, because of the existence of very bright IBPs and dark network structures.

The method suggested here is based on the discrete two-dimensional autocorrelation function $\mathcal{A}_F(\tau)$. If $F(x, y, t)$ is a two-dimensional and time-dependent signal sampled with N_T time steps, then $\mathcal{A}_F(\tau)$ is defined as

$$\mathcal{A}_F(\tau) = \frac{\sum_{i_t=0}^{N_T-\tau-1} \langle (F(i_x, i_y, i_t) - \bar{F}) \cdot (F(i_x, i_y, i_t + \tau) - \bar{F}) \rangle_{x,y}}{\sum_{i_t=0}^{N_T-1} \langle (F(i_x, i_y, i_t))^2 \rangle_{x,y}} \quad (5.2)$$

In this case, $\langle \cdot \rangle_{x,y}$ represents the average over the horizontal elements and $\bar{F} = \langle F(x, y, t) \rangle_{x,y,t}$ represents the average of all elements. It should be noted, that two images with time lag τ_0 are identical if $\mathcal{A}_F(\tau_0) = 1$ or perfectly anti-correlated for $\mathcal{A}_F(\tau_0) = -1$. In case $\mathcal{A}_F(\tau_0) = 0$, two images with time lag τ_0 show no correlation at all and the scene has changed completely so that no structure related to the first image is present anymore. It is common to define the pattern evolution time scale ζ_e as the time at which the autocorrelation has dropped to a value of $1/e$.

To obtain the evolution time scales of the structures seen in the Ca II K filtergrams, $\mathcal{A}_F(\tau)$ is calculated within subfields of $1''.485 \times 1''.485$ size, which overlap by half of their field size in both directions. From these autocorrelations, the values for ζ_e were derived by interpolation to the first occurrence of a value of $1/e$. An example is given in Fig. 5.5 (left).

Plotting the time scale against mean intensity for each subfield results in a distribution that exhibits a gap in ζ_e between 100 s and 200 s (see Fig. 5.5 (right)). This gap is a clear evidence of the different temporal behavior of network and inter-network. Taking a temporal threshold at $\zeta_e = 150$ s leads to a mask M2.

The two thresholds leading to the masks M1 and M2 are indicated in Fig. 5.5 (right) as lines. They show the difference between both methods. They divide the plot in four regions: in the lower left part of the plot those subfields are displayed which show the dark and short lived structures of the inter-network, while the upper right part displays those that show bright and long lived structures of the network. The effect of the thresholds can be seen in Fig. 5.6, where both M1

5. THE CONNECTION OF PHOTOSPHERE AND CHROMOSPHERE

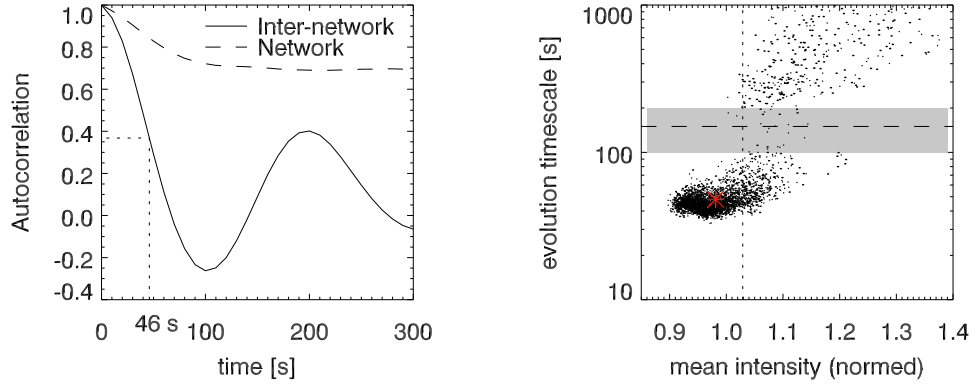


Figure 5.5: Left: Sample of two 2D autocorrelation functions, one of an inter-network region and one of a network region. For the network region, ζ_e is longer than the displayed axis range. Right: Time scale versus mean intensity. For each subfield, ζ_e was plotted against the mean intensity in the subfield. The dotted line is the threshold used for the creation of mask M1, the dashed the one that led to mask M2. The red star marks the position of the barycenter of inter-network points.

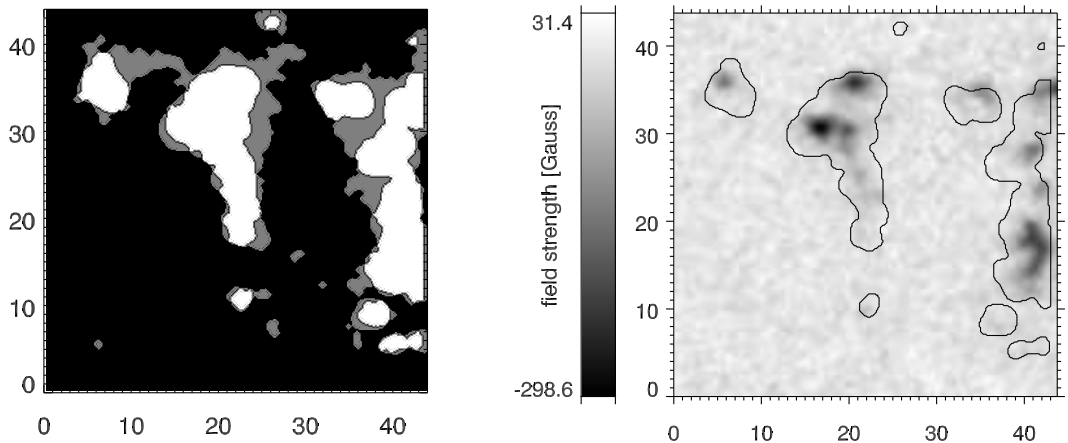


Figure 5.6: Left: The differences between mask M1 and M2. The dark gray area belongs to M1 but not M2, while the white areas show their common points. Right: MDI magnetogram of the region observed, with M2 overlaid as contour. The regions of magnetic flux are contained well within M2.

and M2 are overlaid. M2 is completely contained within M1. The pixels that are attributed to the network according to M1 but not M2 belong to the subfields that contribute to the lower right quadrant in Fig. 5.5 (right). This quadrant contains subfields that are bright on average and exhibit short time scales. Apparently, there are many structures which belong to the inter-network even though they are brighter than average. The good coincidence of magnetic flux and mask M2 is demonstrated by the MDI magnetogram in Fig. 5.6 (right). The mask covers the regions of magnetic flux without extending too much into regions of no magnetic flux.

5.5.2 Morphology

5.5.2.1 Separation and analysis of G-band and Ca II K network bright points

In order to analyze the fine structure of photospheric and chromospheric network in further detail, the structures have to be separated from the remaining structure in the image. This is a difficult task which has been addressed by an algorithm described in Berger *et al.* (1995) to find round structures within a size range that is specified by an input parameter. Using this algorithm, the bright points appear with enhanced contrast allowing to separate them from the surrounding by thresholding. However, to exclude structures which have erroneously been separated, brightenings that only have a life time of only one image and are smaller than the resolution of the image were eliminated. This technique was applied to both the G-band and the Ca II K filtergrams.

After the separation was accomplished to a satisfactory degree, *network* bright points were found by applying the network mask described in Sect. 5.5.1 to the bright point mask. The radii along the major and minor axes were estimated in the following way. Under the assumption of a near elliptic shape of the bright points, the size of the area in one bright point is roughly

$$A = \pi ab \tag{5.3}$$

5. THE CONNECTION OF PHOTOSPHERE AND CHROMOSPHERE

where a and b are the major and minor axes of the ellipse respectively. The application of a morphological distance algorithm (e.g. Jain, 1989) using the euclidean distance metric yields the distance of each point to its closest boundary. Thus, if the structure is an ellipse, the minor axis b can be retrieved as the maximum value of the distance transform of the bright point mask. This is automatically the outcome of the distance algorithm. Once the minor axis is known, the major axis can easily be calculated from equation 5.3 and the calculated area covered by the bright point.

G-band bright points often build chains, also called *filigree*, within the intergranular lanes. In case these chains of bright points cannot be resolved and separated into single bright points, they appear as elliptic or oddly shaped structures in the bright point masks. In order to reduce mismatches due to the chain-like arrangement of the bright points, the local maxima within one patch of the bright point mask were computed. If more than one local maximum was detected, the bright point mask was split with a line perpendicular to the connecting line of the maxima.

Histograms of major and minor axes sizes of the Ca I K and G-band network bright points detected are displayed in Fig. 5.7. For both wavelengths, the histograms for the major and minor half axes roughly show the same peak position. The fit of a log-normal distribution to the G-band bright point histograms of the distribution of major and minor axes diameters, motivated by the fact that this particular distribution describes the statistics of fragmentation processes (Berger *et al.*, 1995), delivers values for the mean diameter of $0''.19$ and $0''.24$ for the minor and major axes, respectively. This conforms with the works of Wiehr & Puschmann (2005); Wiehr *et al.* (2004). However, the G-band bright points might still not be resolved, because the fall-off in the histogram of Fig. 5.7 is close to the resolution limit of the VTT.

Especially for the Ca I K bright points, the histogram for the diameters of major axis is broader, indicating that even though the points were segmented after detection, the bright points showed an elliptical or otherwise oddly shaped structure. Here, the mean diameters are $0''.53$ and $0''.77$ for the minor and major axes, respectively. An explanation for the differences in size of minor and major axes could be that the resolution of the filtergrams might still not suffice to resolve

the finest structure, especially in the Ca II K line, even after the post-processing of the masked patches. The even larger difference in the chromospheric channel can be attributed to the fact that the structure in the chromosphere is web-like, making it generally more difficult to separate intrinsic bright fine-structure within the detected bright patches. Thus, the remaining, not segmented structures are oddly shaped and lead to the differences seen in the histograms.

The sizes of the bright points in photospheric and chromospheric network differ greatly. The fact that the chromospheric network bright points have a larger diameter in general is not very surprising. This can be shown with the following calculation, which is accomplished under very simplifying approximations. Under the assumption of a thin flux tube, whose inside-temperature does not differ from the one outside of the flux tube, one can carry out the following small calculation (after [Steiner \(1990\)](#)). Considering the two pressure stratifications $p_i(z)$ and $p_o(z)$ inside and outside the flux tube at height z :

$$p_i(z) = p_i^0 \cdot \exp(-z/H_p) \quad (5.4)$$

$$p_o(z) = p_o^0 \cdot \exp(-z/H_p) \quad (5.5)$$

where p_i^0 and p_o^0 are the pressures at height $z = 0$ inside and outside of the tube, respectively, and H_p is the pressure scale height. As already explained in [Sect. 5.2](#), the pressure difference is equal to

$$p_o(z) - p_i(z) = (p_o^0 - p_i^0) \cdot \exp(-z/H_p) = B^2/8\pi. \quad (5.6)$$

Referring to the magnetic field strength at height $z = 0$ with B_0 , one gets with [equation \(5.1\)](#)

$$B_0^2/8\pi \cdot \exp(-z/H_p) = B^2/8\pi. \quad (5.7)$$

Because the magnetic flux is conserved at all heights within a flux tube with radius $R(z)$, one has

$$\pi R_0^2 B_0 = \pi R^2(z) B. \quad (5.8)$$

Combining [equations \(5.7\) and \(5.8\)](#), this eventually yields

$$R(z) = R_0 \exp(z/4H_p). \quad (5.9)$$

5. THE CONNECTION OF PHOTOSPHERE AND CHROMOSPHERE

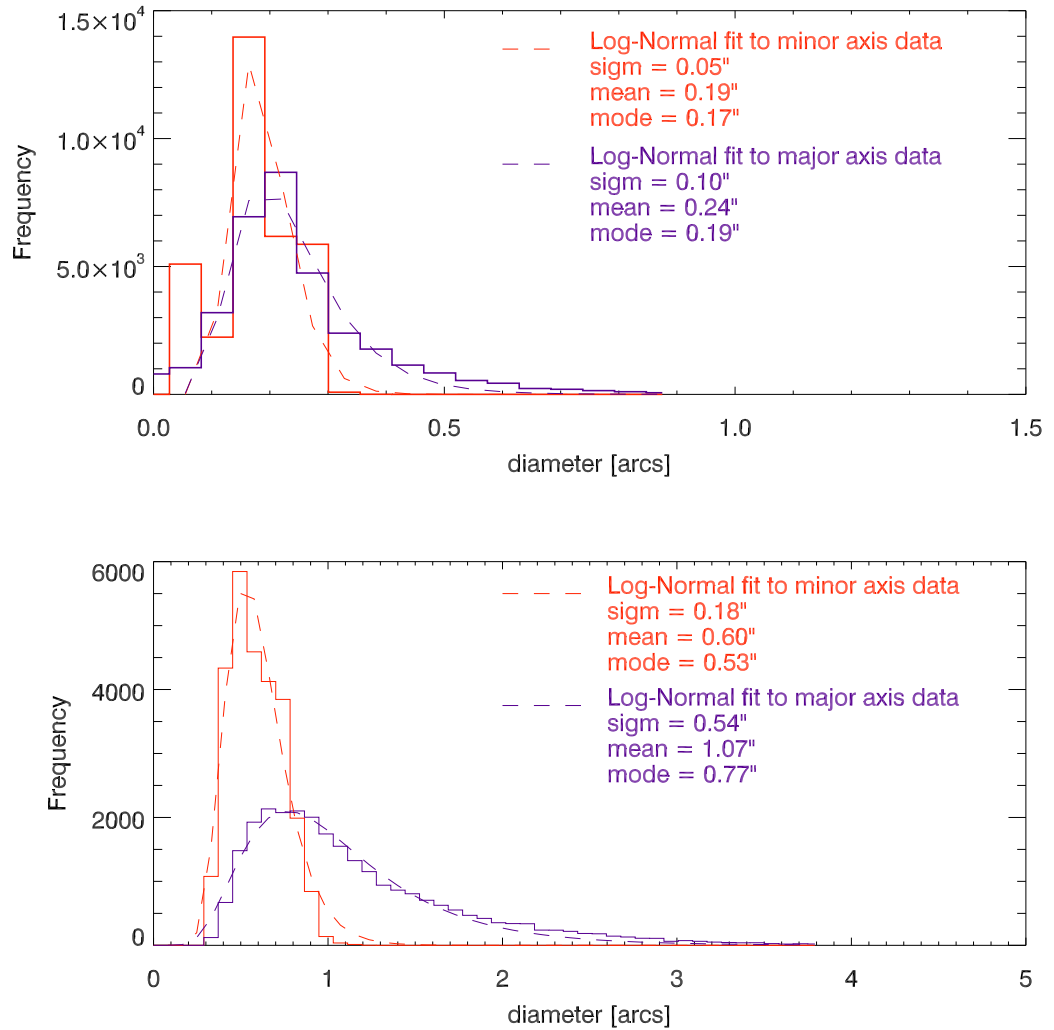


Figure 5.7: Histograms of the sizes of network bright points in G-band (top) and Ca II K (bottom) for the minor (solid) and the major (dashed) axes. A fit of a log-normal distribution is plotted in red.

Using this very rough approximation, a radius for a typical flux tube of $R_{0\text{ km}} = 100\text{ km}$ and a pressure scale height of $H_p = 120\text{ km}$ (Steiner, 1990), one would expect a radius of the magnetic flux tube at a height of $z = 1000\text{ km}$ to be $R(1000\text{ km}) \approx 800\text{ km}$, i.e. the tube's radius increases by a factor of 8. Several things have to be kept in mind here: (1) the simplifying assumption of a thin flux tube, which implies further approximations about the magnetic field, might not be valid for the flux tube at the height at $z = 1000\text{ km}$. (2) The temperature inside the flux tube might differ from the outside temperature, leading to a faster increase in radius of the tube. (3) The approximation deals with the radius of a *magnetic* flux tube; however, the data only consist of intensity measurements. The processes behind the radiative losses in the chromosphere are not fully understood, especially not the role of the magnetic field. Because of this, it is difficult to compare magnetic field to intensity in the in the chromosphere. Ultimately, however, models of the magnetic chromosphere need to be able to reproduce the measurements presented here.

To analyze the ratio of radii of Ca II K to G-band bright points in the dataset, 25 G-band and Ca II K bright point pairs exhibiting typical sizes (Fig. 5.7) were selected manually for a deeper analysis (see Fig. 5.8). In this analysis, not the relative position but rather the relative radii of G-band to Ca II K brightening were of interest. The average ratio of Ca II K to G-band bright point size for the 25 pairs was determined to $\langle R_{Ca\ II\ K}/R_{G\text{-band}} \rangle = 3.0$ with a standard deviation of 0.7. This is much smaller than the ratio of $R_{1000\text{ km}}/R_{0\text{ km}} \approx 8$ that was calculated above for the widening of *magnetic flux tubes* with height. Reasons for this behavior include the questionable validity of the assumptions in the calculation above and the possibility that the Ca II K bright point intensity stems from geometrically lower layers. Furthermore, from Fig. 5.7 one can see that the G-band bright points might still not be resolved.

5.5.2.2 Short-lived pattern in the inter-network

The inter-network is of special interest in this work, because the high spatial resolution of the data presented enables the analysis of the small-scale structures present in this region. The data show a cell-like pattern of granular size which

5. THE CONNECTION OF PHOTOSPHERE AND CHROMOSPHERE

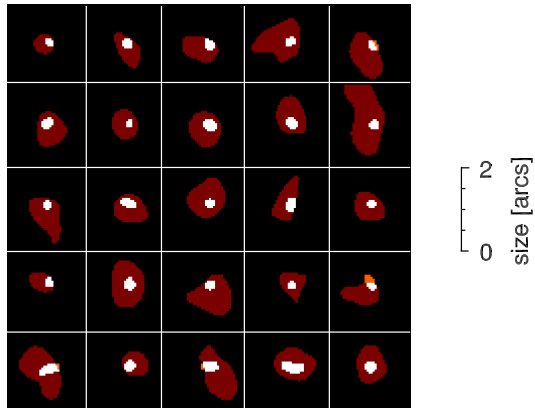


Figure 5.8: Selected network bright points in the G-band (white) and Ca II K (dark red) images. The few areas, where there was a G-band brightening without a co-spatial Ca II K intensity increase are marked in orange.

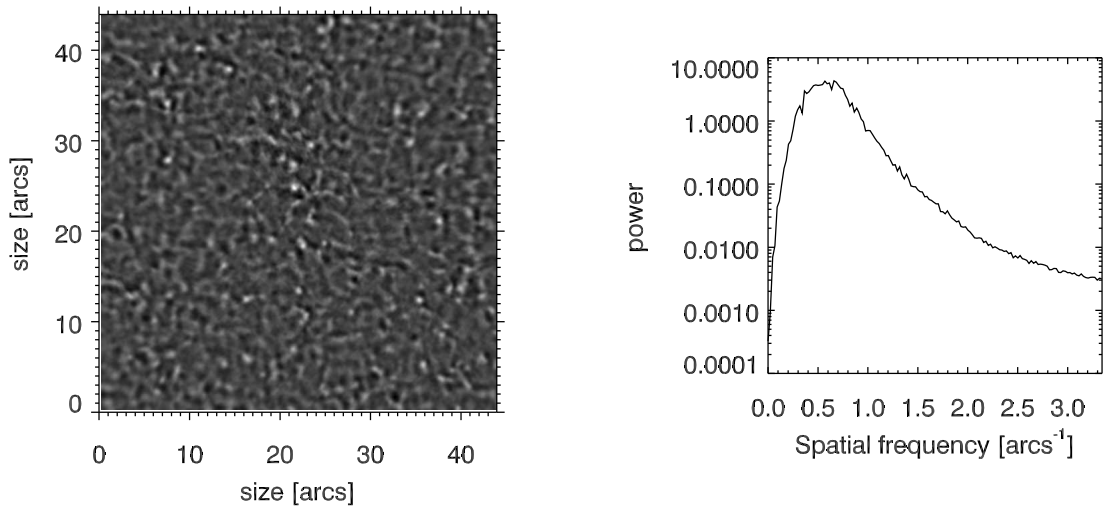


Figure 5.9: Left: Short lived pattern in the chromosphere as enhanced by an unsharp-mask operation applied to a single Ca II K image. Right: Its spatial power spectrum.

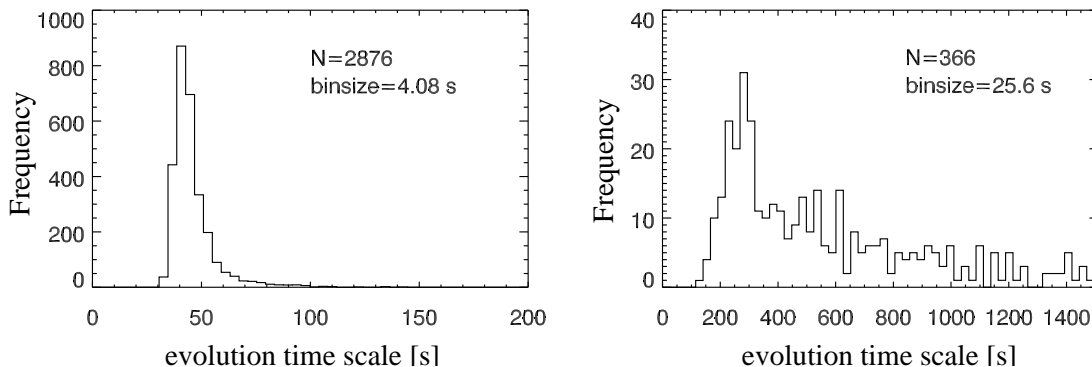


Figure 5.10: Histograms of the distribution of time scales ζ_e for structures in Ca II K filtergrams attributed to the network (left) and inter-network (right).

changes rapidly. To enhance the small-scale nature of the pattern of interest, an unsharp-masked image was subtracted from the data. The two-dimensional power spectrum of the resulting image (displayed in Fig. 5.9 (left)) was then azimuthally integrated. The one-dimensional power spectrum is shown in Fig. 5.9 (right). The barycenter of power is at $f_h = 0.65 \text{ arcs}^{-1}$ corresponding to a spatial scale of $1''.5$, which conforms to granular sizes.

To quantitatively demonstrate the difference of life times between network and inter-network structures, histograms of the time scales ζ_e are displayed for network (Fig. 5.10 (left)) and inter-network (Fig. 5.10 (right)). There is a peak in the histogram of life times of network structures around $\zeta_e = 300 \text{ s}$. Some structures even lived as long as the duration of the data sequence. For inter-network structures, the peak of the histogram is well below $\zeta_e = 50 \text{ s}$. This is better illustrated by Fig. 5.5. The barycenter of the subfields of the inter-network regions lies at $\bar{\zeta}_e = 48 \text{ s}$ and a mean intensity of 0.981. The standard deviation in time scale is 10.1 s and the minimum value is $\zeta_{e,min} = 33 \text{ s}$. These time scales are much shorter than those of the granules or reversed granulation which are almost a factor of two larger. This indicates that the pattern is not directly connected to the photospheric granulation.

To verify the chromospheric origin of the detected inter-network pattern, its spatial scale and evolution time scale is compared to the recent 3D model by [Wedemeyer *et al.* \(2004\)](#). The temperature amplitudes of the model chromosphere might be somewhat uncertain due to the simplified treatment of the atmosphere

5. THE CONNECTION OF PHOTOSPHERE AND CHROMOSPHERE

(gray, LTE), whereas the excitation of the waves occurs in realistically modeled lower layers, making the dynamics and related time scales more reliable. A direct comparison with synthetic intensity maps for Ca II K_{2v} is not possible yet as the model chromosphere is dominated by strong shocks that cause numerical problems for the Ca II K_{2v} intensity synthesis. One can, however, perform a qualitative comparison with horizontal slices of gas temperature from the model chromosphere. The cuts at a geometrical height around 1000 km above $\tau_c = 1$ exhibit a pattern of granular size, which rapidly evolves with time scales of around $\zeta_e = 20 - 30$ s. The pattern is quite similar to the one observed, but the evolution time scale is still almost a factor of two shorter than the observational value. This can be explained as follows: First of all, the correlation between gas temperature at $z = 1000$ km and intensity in the Ca II K_{2v} spectral feature might be poor as the assumption of LTE is not valid in this strongly scattering line. In LTE local changes in temperature are instantaneously translated into changes of the source function and thus intensity changes although the intensity response is non-linear in amplitude. In contrast to the temperature slices at a well-defined geometrical height, the emergent intensity (at a given wavelength) is a non-local quantity that has contributions from an extended height range. For the line core, the main contribution of intensity originates from chromospheric heights around 1000 - 1500 km above $\tau_c = 1$ (cf. Vernazza *et al.*, 1981), but already at 0.15 Å off-core, considerable contributions to the filtergram intensity from lower geometrical heights have to be expected (Rammacher, priv. comm.). The emergent intensity is the result of integration along the line of sight over many layers that individually would show different pattern evolution time scales (decreasing with height, see Wedemeyer, 2003). The integrated pattern is consequently smoothed so that the relative intensity variations become smaller and result in longer evolution time scales. This effect is enhanced by the fact that the observed intensity refers to corrugated surfaces of constant optical depth instead of plane horizontal cuts as used for the model. The intensity pattern will be smoothed even more compared to the fine structure in the temperature cuts. Wedemeyer *et al.* (2004) calculate a time scale of $\zeta_{e,z} > 120$ s for changes in gas temperature in a horizontal plane cut at the bottom of the photosphere, whereas the emergent intensity (under the assumption of LTE, which reflects conditions at the bottom of the photosphere),

yields an increase of the typical time scale to $\zeta_{e,\tau_c} = 200$ s. This is due to the fact that variations tend to be smaller on surfaces of constant optical depth because they are shaped by inhomogeneities themselves. In addition, seeing and instrumental effects lead to a spatial smearing of the intensity signal and thus to longer time scales. Smoothing the temperature cuts to the spatial resolution encountered in our data increases the time scales by about 25%. The simulations of [Wedemeyer *et al.* \(2004\)](#) do not include magnetic field. The existence of inter-network fields (with intrinsic field strengths varying from 1 kG down to ≈ 20 G) is undisputed as they have been recently measured with high polarimetric precision (see [Khomenko *et al.*, 2005](#); [Sánchez Almeida, 2006](#), and references therein). The contribution of possibly unresolved magnetic elements in inter-network regions tends to lengthen the effective evolution time scale. A preliminary analysis of temperature cuts from the 3D magnetohydrodynamics model by [Schaffenberger *et al.* \(2005\)](#) results in a slightly higher value of $\zeta_{e,MHD} = 27$ s at the same height ($z = 1000$ km) compared to 24 s in the purely hydrodynamical model by [Wedemeyer *et al.* \(2004\)](#). Consideration of all these effects leads to a reasonable agreement between observation and numerical model.

5.5.3 Oscillations

Solar oscillatory motions have been discovered in 1960 by [Leighton *et al.* \(1962\)](#). The discovery that a large number of these motions have a spectrum of discrete frequencies between 1-9 mHz (according to periods between 2-15 minutes) led to the development of a new branch of solar research. The restoring force for most oscillations is due to pressure gradients, hence they are referred to as p-modes. The signature of the p-modes can be found not only by observation of plasma motion but also by observation of line intensity. Measurements have shown that the maximum amplitude of the oscillations in the photosphere lies at periods of around 5 min and is shifted towards shorter periods of around 3 min in the chromosphere ([Stix, 2002](#)).

A tool to analyze temporal and spatial frequency as well as power of oscillations simultaneously is the $k_h - \nu$ -diagram. The power spectral density (power

5. THE CONNECTION OF PHOTOSPHERE AND CHROMOSPHERE

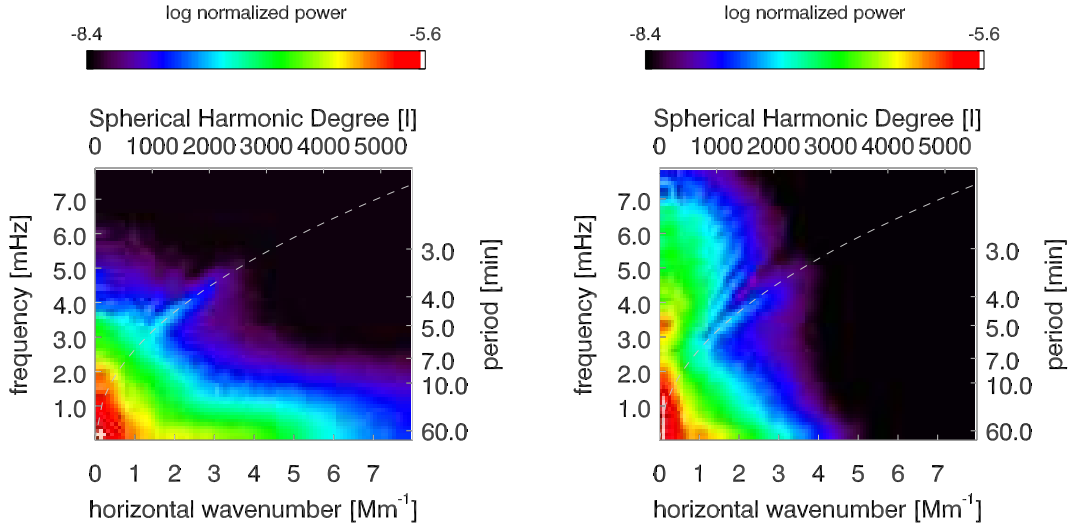


Figure 5.11: $k_h - \nu$ -diagram of the photospheric G-band data (left) and the chromospheric Ca II K data (right). The dashed line denotes the f-mode (see text).

spectrum) of a signal $I(x, y, t)$ is defined as

$$P_I(k_x, k_y, \nu) = |\tilde{I}(k_x, k_y, \nu)|^2, \quad (5.10)$$

where $\tilde{I}(k_x, k_y, \nu)$ is the Fourier transform of $I(x, y, t)$, k_x and k_y are the spatial wavenumbers in x- and y-direction, and ν is the temporal frequency. In case of no preferred horizontal direction, P_I is only dependent on the horizontal spatial wavenumber $k_h = \sqrt{k_x^2 + k_y^2}$. In any case, the average of P_I may be calculated as

$$P_I(k_h, \nu) = \frac{1}{2\pi} \int_0^{2\pi} d\phi P(k_x \cos \phi, k_y \sin \phi, \nu), \quad (5.11)$$

where $\phi = \arctan \frac{k_y}{k_x}$. $P_I(k_h, \nu)$ is plotted in color code in a $k_h - \nu$ -diagram.

Fig. 5.11 shows two $k_h - \nu$ -diagrams, one based on the photospheric G-band, the other on the chromospheric Ca II K filtergram sequence. As already mentioned before, the main contribution of power in the photosphere (G-band data) is from frequencies lower than 5 mHz (corresponding to periods of 3.5 minutes). The diagram for the G-band data in Fig. 5.11 clearly shows this behavior. In contrast, the chromospheric $k_h - \nu$ -diagram of the Ca II K data also shows high relative

power at frequencies higher than 5 mHz. The differences in the photospheric and chromospheric diagrams come from the fact that at chromospheric levels the pressure variations of the p-modes result in much stronger temperature increases than at photospheric levels. This leads to an enhanced signal in intensity. The dashed line depicts the fundamental mode, for which $\nu = \frac{1}{2\pi} \sqrt{g \cdot k_h}$, where g is the gravitational constant at the solar 'surface' ($g = 273.5$ m/s). The fundamental mode (f-mode) represents the surface wave on deep water. It divides the diagram into two regions. The region in the upper part contains the p-modes (Stix, 2002).

It is worthwhile to note, that as can be seen in both diagrams of Fig. 5.11, the power is not evenly distributed in the $k_h - \nu$, but rather follows *ridges*. One can show that each ridge corresponds to a fixed number of wave nodes in radial direction. These ridges are typical for the p-modes (Stix, 2002) and many more are present on the sun (Chou *et al.*, 1995). Here about seven ridges can be seen; because of the limited duration of the data sequence, further ridges cannot be resolved. However, it is an interesting fact that the f-mode has about the same power as p-mode oscillations which is in contrast to observations with lower spatial resolution (e.g. Chou *et al.*, 1995), where the f-mode shows the weakest power and is thus usually difficult to detect.

In Fig. 5.12, two $k_h - \nu$ -diagrams of the Ca II K line are displayed to the same scale. The difference between both diagrams is that one $k_h - \nu$ -diagram is based on a sequence depicting the chromospheric network, whereas the other shows the properties of the chromospheric inter-network.

The main contribution to the power of the p-mode oscillations thus come from inter-network regions, for the following reasons:

- The frequency band around 5.5 mHz shows a decreased power for network regions (Fig. 5.12, C)), a fact that is supported by Fig. 5.12, D).
- In the $k_h - \nu$ -diagrams (Fig. 5.12, A) and B)), there is a distinct difference at temporal frequencies higher than 4.5 mHz. The relative power at frequencies higher than 4.5 mHz is much smaller for network than for inter-network regions.
- Fig. 5.11 shows in the $k_h - \nu$ -diagram for the Ca II K data that the p-mode oscillations produce signal to frequencies much higher than 4.5 mHz.

5. THE CONNECTION OF PHOTOSPHERE AND CHROMOSPHERE

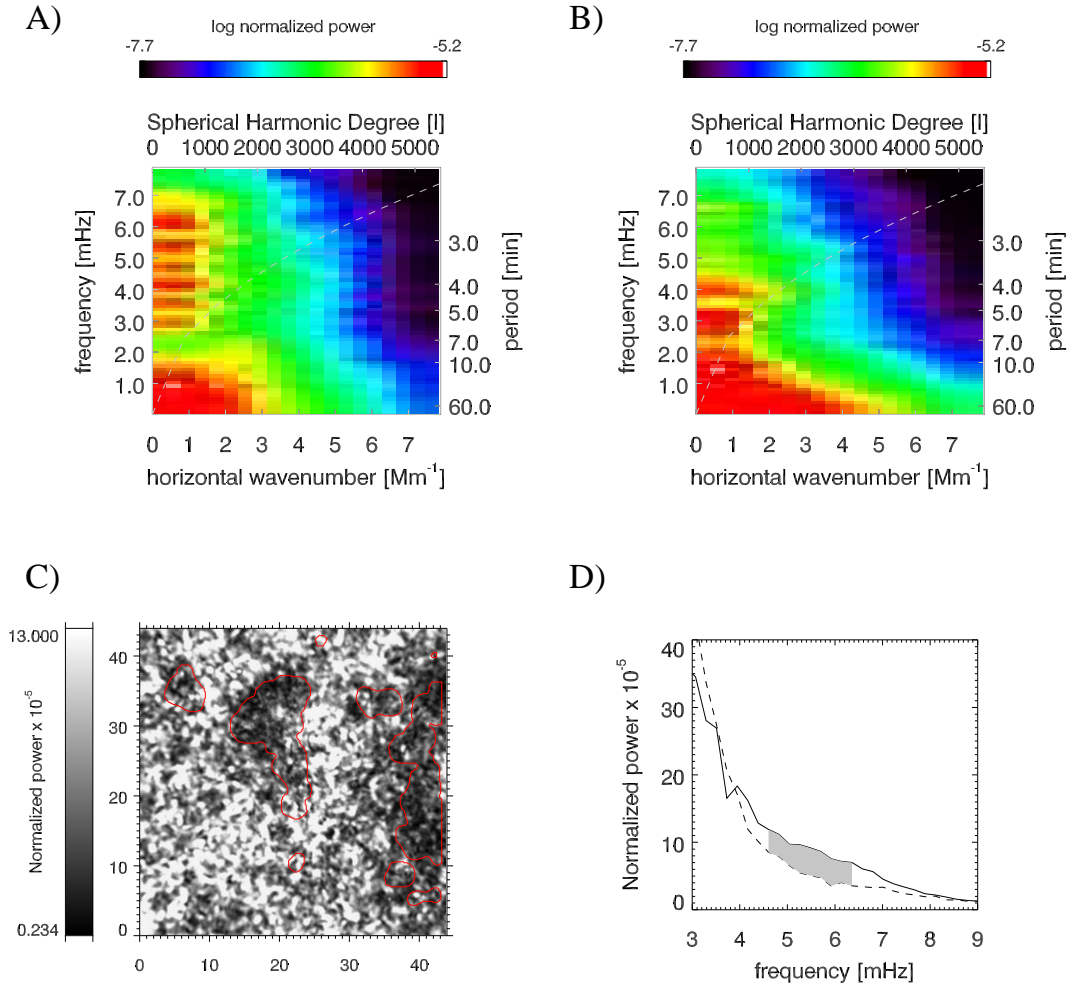


Figure 5.12: A) $k_h - \nu$ -diagram of the Ca II K data in inter-network and B) network. The dashed line denotes again the f-mode (see text). C) Powermap at the frequency band around 5.5 mHz with a width of 0.9 mHz with overlaid mask M2 (red contour). D) Temporal power, averaged over network and inter-network pixels according to mask M2. The average inter-network power (solid line) is enhanced relative to the network power (dashed). The shaded region displays illustrates the width of the frequency band used in C).

The last two points show that the oscillatory behavior in the inter-network is substantially different from that in the network. The contribution to the ridges in Fig. 5.11 must be mainly due to the inter-network because Fig. 5.12 A) and B) show that in the network, as opposed to the inter-network, frequencies higher than 4.5 mHz have almost no contribution.

5.5.4 Correlation with the photosphere

An analysis of the correlation between photospheric and chromospheric network bright points is important for the understanding of the connection between these two layers. A first impression is given in Fig. 5.13 (left), where for each pixel the intensity of the temporal average of the G-band sequence was plotted versus the temporal average of the Ca II K channel displayed in Fig. 5.4). The plot shows a large scatter. The reason is that the G-band images show much finer structure than the Ca II K images, because either the structure is not present in the chromosphere or the resolution of the Ca II K filtergrams is still not high enough.

A trend for the pixels that are attributed to the network by mask M2 shows that increased network intensity in the G-band channel also is related to increased intensity in the Ca II K channel Fig. 5.13 (left, blue line). Increased intensity in the time averaged Ca II K channel again occurs only in the network. Thus, there is an indication for a connection between bright network structures in photosphere (G-band) and chromosphere (Ca II K).

As can be seen in Fig. 5.4 (left), the temporal average shows still structure in inter-network regions of the photosphere; a longer time sequence would be needed to average out all of the granular structure. This is in contrast to inter-network regions of the chromosphere, where the structures are more dynamic than in the photosphere (see Sect. 5.5.2.2): here, the short-lived pattern has disappeared because of the temporal averaging process. The result is the 'reversal' in the tail at Ca II K intensities with $I_{Ca} \leq 0.9$ (Fig. 5.13 (left, yellow line)).

5. THE CONNECTION OF PHOTOSPHERE AND CHROMOSPHERE

5.5.4.1 Distance between maxima in intensity

Within each detected G-band and Ca II K network bright point patch, the maximum intensity was determined. The distance and angular direction between each detected G-band network bright point maximum and the nearest Ca II K network bright point maximum was measured. The results of the measurements were combined in a two-dimensional histogram displayed in Fig. 5.13 (right). The irregular pattern ('holes' in the distribution) is due to an insufficient number of bright point samples and could be avoided by a coarser binning. The histogram shows a distribution that is well fitted by a two-dimensional, elliptical Gaussian equation

$$G(x, y) = A + B \cdot \exp(-C/2), \text{ where } C = [(x - x_0)/\sigma_x]^2 + [(y - y_0)/\sigma_y]^2. \quad (5.12)$$

A fit yields for the parameters of interest yields $(x_0, y_0) = (-0.16, -0.10)$ and $(\sigma_x, \sigma_y) = (0.35, 0.37)$, where the units are arcs. The fit is displayed in Fig. 5.13 (right) as contour lines and shows that the distribution is isotropic. The data were observed at solar disc center and therefore no significant deviations from isotropy because of line-of-sight effects due to the spherical character of the Sun are expected. an offset between G-band and Ca II K network brightenings would be indicated by a value of $(x_0, y_0) \neq (0, 0)$. However, the numbers given above are not conclusive because they are too close to the limit set by the size of one resolution element, seeing not included (see Sect. 5.4). The fitted values for (x_0, y_0) indicate that there is no vertical offset implying that if there *is* a Ca II K network bright point located above a G-band bright point, it is placed co-spatially. This implies again strong spatial correlation between bright network structures in the photosphere and chromosphere. In Sect. 5.2, the connection between G-band bright points and underlying magnetic field was pointed out. This connection is supported as well when looking at Fig. 5.6 (right) in combination with Fig. 5.4 (left). The obviously stable network structures in the temporally averaged G-band image are coinciding with mask M2, which covers almost all of the significant flux in the magnetogram. Taking this into account, it seems probable that Ca II K network bright points are the intensity signature of flux tubes that extend from the photosphere into the chromosphere. The expanding radii are attributed to

the pressure equilibrium in the stratified solar atmosphere (see Sect. [5.5.2.1](#)). In the following, two individual cases are displayed showing the typical behavior of network and inter-network brightenings in the photosphere and chromosphere.

5. THE CONNECTION OF PHOTOSPHERE AND CHROMOSPHERE

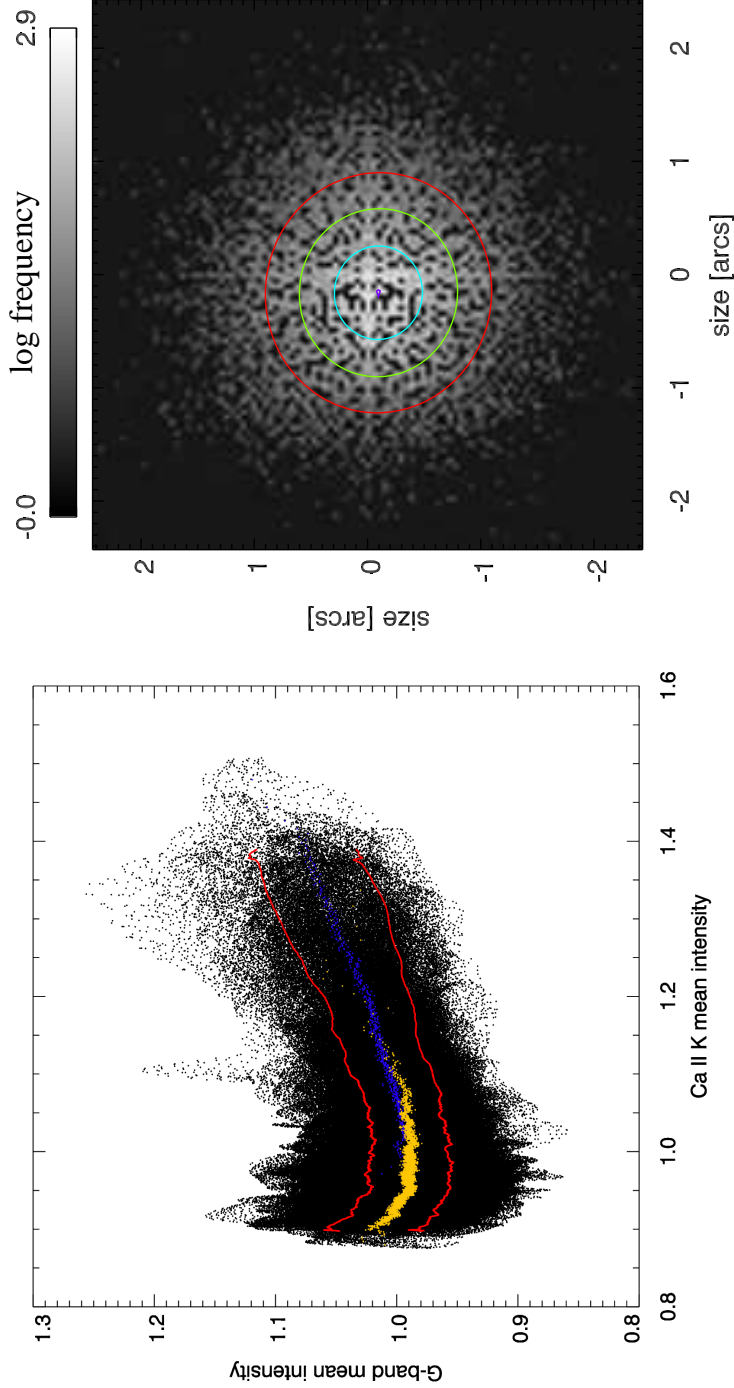


Figure 5.13: Left: Time-averaged intensities of G-band versus Ca II K for each pixel. The colored points are average values calculated within bins defined by the binning of the x-axis (Ca II K intensity). The values were calculated separately for inter-network (yellow) and network points (blue) according to mask M2. The red lines indicate the standard deviation within each bin. Right: Two-dimensional histogram of the distance between the location of maximal intensity of each G-band bright point and the maximum intensity of the nearest Ca bright point. The circles represent the distance from the peak (violet) of 1σ (blue), 2σ (green) and 3σ (red), where $\sigma = 0.36$ arcs.

5.5.4.2 Individual case 1: network fine-structure

In Fig. 5.14, an example for the temporal evolution of a network bright point in the G-band and the corresponding brightening in the chromosphere are displayed. In order to achieve this analysis, a subfield of the G-band and Ca II K image sequence was selected, and followed throughout the whole sequence. A data analysis tool (Clyne & Rast, 2005) was used to visualize the brightest pixels in three dimensions, the third dimension being time. Only pixels within an intensity range of $1.429 \leq I_{Ca,net} \leq 1.805$ in Ca II K and $1.511 \leq I_{Gb,net} \leq 2.051$ in G-band filtergrams were rendered opaque with a color table extending from blue to violet for the Ca II K intensity and yellow to green for the G-band intensity. All pixels below the minimum threshold were rendered transparently. In a second step, the two resulting images were overlaid, each with 50% transparency. The images are able to demonstrate the close connection in location and temporal behavior of both features. All movements of the G-band network brightening are followed closely, visually without temporal lag. Almost each network brightening in the photospheric G-band has a counterpart in chromospheric emission in the Ca II K filtergram which has an increased diameter. As already mentioned in the previous section, this could be explained by a flux tube extending upwards.

5.5.4.3 Individual case 2: inter-network fine-structure

In this example, an inter-network region was separated in the same way as in case 1 above. Here, the thresholds for opaque rendering were $1.044 \leq I_{Ca,inet} \leq 1.302$ for Ca II K and $1.275 \leq I_{Gb,inet} \leq 1.583$ for G-band filtergrams, where the color table was the same as before. The field of view was increased with respect to case 1 (see Sect. 5.5.4.2) in order to show more than one G-band brightening in the field of view. Although Ca II K emission can be noted close to the G-band bright point at the beginning, there is no strong relationship between these two phenomena as there was for the network bright point in case 1 (Sect. 5.5.4.2). The Ca II K intensity quickly decreases. A correlation of G-band to Ca II K intensity later on is doubtful. Another interesting feature of this plot is the fact that almost all intensity is continuously propagating. When plotting the temperature cuts of the model of Wedemeyer *et al.* (2004) in a similar way (here $6180 \leq T_{model} \leq$

5. THE CONNECTION OF PHOTOSPHERE AND CHROMOSPHERE

6975 K), the cuts show a very similar behavior (Fig. 5.16 (left)), because of the nature of the phenomenon: the propagating shock waves run into each other in a spatially and temporally continuous way (see Fig. 5.16 (right)). At the border of two interfering shock fronts, a temperature increase beyond the normal shock temperature occurs which propagates with the moving shock fronts. The strong increase in temperature could result in an enhanced emission that would have a point like shape, similar to the Ca II K inter-network grains. It must be stressed again, though, that the temporal temperature evolution that is displayed here does not easily translate into intensity evolution because of non-LTE effects (see Sect. 5.5.2.2).

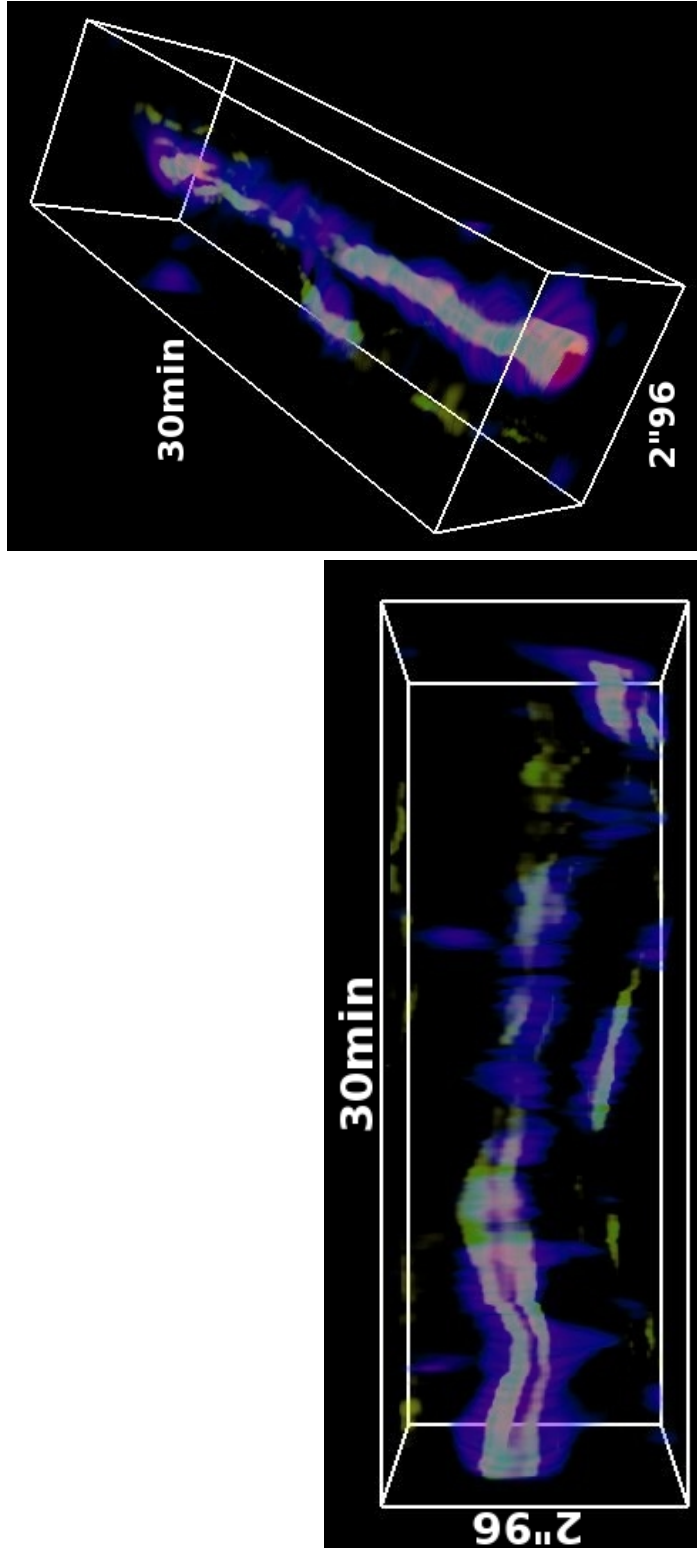


Figure 5.14: Study of the temporal behavior of an especially prominent but otherwise typical network G-band bright point (yellow to green) and the corresponding Ca brightening (blue to violet). The size of the box is $2''.96 \times 2''.96 \times 30$ min. Both images show the same data cube at a different angle. The close relation between the brightenings at both layers, i.e. the co-spatial movement of the structures, can be seen very well.

5. THE CONNECTION OF PHOTOSPHERE AND CHROMOSPHERE

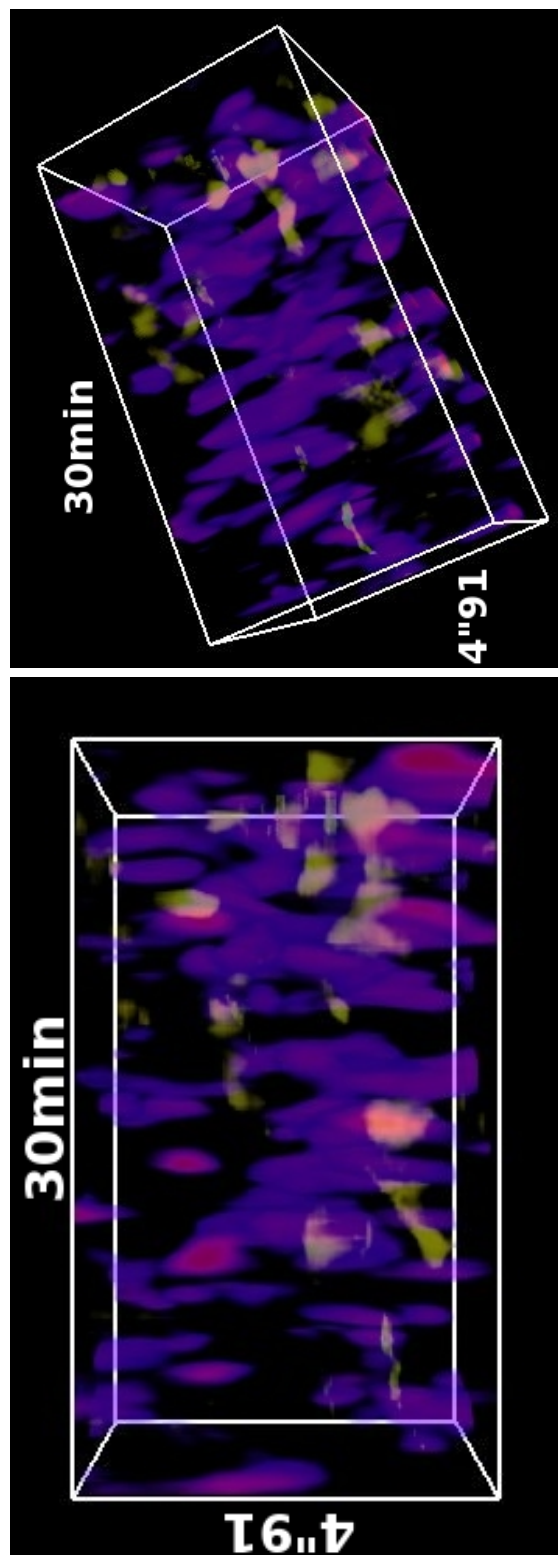


Figure 5.15: Study of the temporal behavior of an inter-network G-band bright point (yellow) and the corresponding Ca brightening (blue). The size of the box is $4''91 \times 4''91 \times 30$ min. In contrast to Fig. 5.14, there does not seem to be a relation between intensity in G-band and Ca IIK. Various patches in G-band intensity (yellow to green) can be attributed to bright edges of granules.

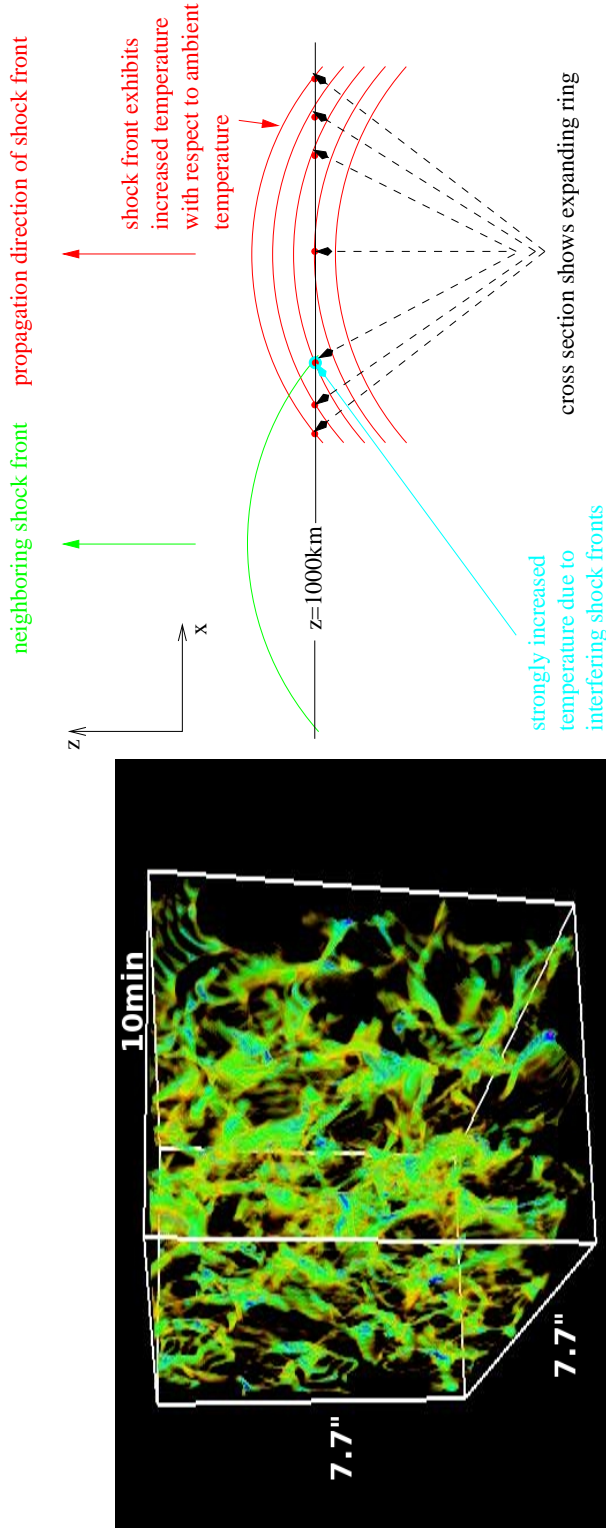


Figure 5.16: Left: Temporal evolution of temperature cuts at the height of 1000 km above $\tau_c = 1$ of the model of [Wedemeyer et al. \(2004\)](#) displayed in a similar way as in Fig. 5.14. The shocked plasma shows increased temperature. Because the continuously upwards propagating waves interfere at different times and places, the increase in temperature is continuously propagating (data courtesy of Sven Wedemeyer-Böhm). The size of the box is $7.7'' \times 7.7'' \times 10 \text{ min}$. Right: Sketch that illustrates the origin of the small-scale pattern exhibited by the temperature distribution. Within a cut at a certain geometrical height (here $z = 1000 \text{ km}$) a spherical shock front first appears as single point of increased temperature that transforms into an expanding circle while it propagates, because post-shock regions are cooled because of adiabatic expansion of the gas. If the shock front encounters a neighboring shock front, the temperature is increased even further.

5. THE CONNECTION OF PHOTOSPHERE AND CHROMOSPHERE

5.6 Conclusion

In this chapter, the observed data have been analyzed under the aspects of morphology, dynamics, and correlation of small scale structure encountered in the photosphere and chromosphere.

In the course of this analysis, a new method to distinguish between network and inter-network has been suggested (Sect. 5.5.1). Compared to masks created by intensity thresholding, masks created using the new method allow to distinguish between these two regions more accurately.

The analysis of network bright points detected in G-band and Ca filtergrams is in line with other works regarding the sizes of these structures (Berger & Title, 2001; Wiehr & Puschmann, 2005; Wiehr *et al.*, 2004) (Sect. 5.5.2.1).

The observed ratio of Ca II K to G-band network bright point diameters of $\langle R_{Ca\ II\ K}/R_{G\text{-band}} \rangle = 3.0$ with a standard deviation of 0.7 which deviates from the ratio of 8 as calculated for the expansion of the radius of magnetic fluxtubes by a simple model (Sect. 5.5.2.1). This could be a sign that the assumptions of the model are not fulfilled. Another reason could be that the emission of the network bright points stems from regions below the assumed height of 1000 km because of a reduction of opacity due to the magnetic field. However, further analysis shows that network bright points in the G-band and Ca II K network grains are spatially well correlated as was shown by the histogram of measured distances between G-band and Ca II K bright point maxima (Sect. 5.5.4). The individual case of the network bright point in photosphere and chromosphere (Sect. 5.5.4.2) shows the co-spatial movement of G-band and Ca II K bright point. The behavior of inter-network bright points in photo- and chromosphere is fundamentally different. G-band and Ca II K inter-network brightenings show no obvious connection (Sect. 5.5.4.3).

The analysis of oscillations present in the G-band and Ca filtergrams shows no real surprise (Sect. 5.5.3) because they have been analyzed in great detail in the past (e.g. Kneer & von Uexkull, 1993). An exception is the high power of the f-mode. A reason for this could be the unprecedented combination of high spatial and spectral resolution of the data presented here. In the photosphere, oscillations with frequencies of 3.3 mHz are predominant and the relative power

at higher frequencies is very low. This is different in the chromosphere, where the relative power at frequencies above 4.5 mHz, corresponding to periods below 3.7 min, is high.

However, the high spatial sampling of the observed dataset allows to analyze a time series in the chromospheric network and compare it to one for the inter-network. The result, in combination with power maps and one-dimensional power spectra averaged over network and inter-network pixels separately, strongly indicates that the major contribution to the well known 3 min oscillations originates in the inter-network. Network regions, on the other hand, show a high relative power at periods of 5 min, indicating a closer connection to the photosphere. This is in line with the theory of *magnetic portals* as suggested by [De Pontieu *et al.* \(2005\)](#), which proposes the tunneling of low frequency waves to high chromospheric regions. A necessary condition for this model is that the flux tubes show an inclination angle other than 90 degrees with respect to the surface. The data presented here, however, clearly exhibit a close spatial connection between the position of network G-band and Ca II K bright points, implying an almost vertical orientation of the flux tubes that are likely to be responsible for the co-spatial brightenings. The theory of magnetic portals is thus not supported by the data and other mechanisms for the energy transport to the chromosphere must still be considered.

It has become evident that chromospheric network bright points are usually by far more stable than their inter-network counterparts, also called Ca II K grains (see also [Carlsson & Stein, 1997](#)). These are probably part of the small scale inter-network pattern that has been detected in the data. An interpretation of this pattern as reversed granulation is inappropriate as the corresponding time scale is much longer than the 53 s found here. [Leenaarts & Wedemeyer-Böhm \(2005\)](#) state 120 s and 90 s for observed and synthetic Ca II H line wing intensities, respectively, which clearly originate from the mid-photosphere (see also [Wedemeyer, 2003](#)). These values are in line with the time scale of the order of 90 s for the reversed granulation pattern observed in the Fe I line core at 709.0 nm by [Janssen & Cauzzi \(2006\)](#). To conclude, it is found that the small-scale inter-network pattern reported here evolves too fast to be due to reversed granulation. Given the finding of [Wedemeyer \(2003\)](#) that the time scale decreased with height,

5. THE CONNECTION OF PHOTOSPHERE AND CHROMOSPHERE

the faster evolving pattern presented here is thus of chromospheric origin. The pattern is very likely the intensity signature of the mesh-like, fast evolving pattern found in recent 3D hydrodynamical models of the solar chromosphere. It is presumably a product of the propagation and interaction of shock waves (Wedemeyer *et al.*, 2004) that are excited below the observed layer. The same is true for the Ca II grains in the inter-network that is considered as an integral part of the pattern. Collision of two neighboring wave fronts results in compression and heating of the gas at the contact region that shows up as a band of enhanced intensity, making up the "strings" of the mesh-like pattern. At a mesh vertex, however, more than two wave fronts meet, resulting in stronger compression and thus in an intensity higher than the remaining pattern. Due to the limitations of earlier observations (especially regarding the combination of high spectral and spatial resolution), only the brightest components have been detected as grains, whereas the pattern itself remained undetected. The results presented here are the base for the conclusion that inter-network bright points are a prominent but integral part of the small-scale pattern produced by interaction of chromospheric shock waves.

Chapter 6

Conclusions

In this work, the morphology, dynamics and relation between the small-scale structure of the photosphere and chromosphere were investigated. The detection of this fine structure is difficult, as atmospheric turbulence reduces the resolution of all earthbound observations.

In order to reduce the effect of atmospheric turbulence in the observed data, a parallelized image reconstruction package based on the theory of speckle interferometry was developed. Parallelization is needed in order to analyze in the immense amount of data that is collected during one observational run. From tests on different processor architectures and operating systems it can be seen that the code scales almost linearly with the amount of computing processors used, until a saturation due to limited network bandwidth is reached.

The package implements algorithms which are ready to reconstruct data observed with an AO system. It thus combines the two most powerful techniques to overcome image degradation due to atmospheric turbulence: in-situ adaptive optics correction with speckle interferometric post-processing of the data. This was achieved by modifying well-known analytical models of atmospheric transfer functions that take into account the correction of an AO system. These new models for AO transfer functions can be easily adapted to any specific system when analyzing their wavefront sensor data. The validity of the models has been verified using several approaches, resulting in a good agreement to observed data.

The Ca II K images were exposed for 2 s, because of the small width of the Lyot filter used (0.03 nm), its poor transmission and the limited camera sensitivity at

6. CONCLUSIONS

393.3 nm. Such long exposed images cannot be processed using speckle interferometry. Therefore, an algorithm was developed to estimate the point spread function from simultaneously observed speckle data. With the use of these functions, a post-facto deconvolution of the long exposed images using well-known deconvolution algorithms becomes possible. The method was tested on synthetic data which were artificially aberrated equivalent to atmospheric conditions of Fried parameters of $r_0=5,7,10,20$ cm. The application of the algorithm to the synthetic data demonstrated the ability to reconstruct the morphological structure of the original images. It was found that the results are acceptable if the atmospheric conditions were good enough ($r_0 > 10$ cm) to allow for an accurate reconstruction of the point spread function.

The data taken at the Vacuum Tower Telescope of the Kiepenheuer-Institut für Sonnenphysik at the Observatorio del Teide on Tenerife, Spain were observed under good atmospheric conditions ($r_0 \approx 15$ cm most of the time). This allowed the reconstruction of the data using the algorithms developed for this thesis. The dataset included filtergrams in the Fraunhofer G-band and the Ca II K line at 430.5 nm and 393.3 nm, respectively. While the G-band data shows the photosphere and its fine-structure especially well, the Ca II K intensity comes mostly from the chromosphere. The analysis of morphology, dynamics and correlation revealed new information about these two atmospheric layers:

- The size of network G-band bright points is on average a factor of 3 smaller than their counterparts in the chromosphere, the Ca II K network bright points.
- Network G-band and Ca II K bright points show a high spatial correlation. An individual case study shows that their movement is tightly connected.
- The lifetimes of network and inter-network structures based on their temporal auto-correlation differ greatly. While inter-network structures are very short lived with lifetimes that are on average around 50 s, network structures have lifetimes starting around 150 s and more. This allows a discrimination between both regions based on lifetime.

-
- Morphology and lifetime of the inter-network pattern observed fits well to the three-dimensional hydrodynamical models of the chromosphere to [Wedemeyer *et al.* \(2004\)](#).
 - Analysis of the oscillations show that the major contributions to the chromospheric 5.5 mHz oscillations (corresponding to periods of 3 min) originate from inter-network structures, whereas network structure show highest power at 3.3 mHz, the frequency of photospheric oscillations (periods of 5 min).

This information indicates that the chromospheric structure is diverse, and that especially network structures have a close connection to photospheric magnetic elements. Considering the close vertical correlation of bright points in photosphere and chromosphere, there are no indications for an inclination of the flux tubes.

The pattern in the inter-network detected in this work seems to be the product of the propagation and interaction of shock waves that are excited in the photosphere as an acoustic phenomenon.

In future observations, it is necessary to include simultaneous measurements of the magnetic field vector together with a dataset as the one presented here. The additional information on the magnetic field will enable a more detailed look on the inclination of the flux tubes and possibly the flux in the chromosphere. Using such a dataset, one might be able to resolve the question on how intensity and magnetic field in the chromosphere are related which might give the answer to the question of the mechanism responsible for the energy transport to the higher layers of the Sun's atmosphere.

6. CONCLUSIONS

Nomenclature

Roman Symbols

D telescope diameter

W telescope pupil

Greek Symbols

λ observed wavelength

τ correlation time

τ_c optical depth at continuum wavelength

θ_{iso} isoplanatic angle

Other Symbols

$\mathcal{A}_F(\tau)$ Autocorrelation of function F

O^* Complex Conjugate of O

\tilde{O} Fourier transform of O

Acronyms

AO Adaptive Optics (System)

FWHM Full Width at Half Maximum

LTF Long-Exposure Transfer Function

6. CONCLUSIONS

MEM Maximum Entropy Method

MTF Modulation Transfer Function

OTF Optical Transfer Function

PSF Point Spread Function

SNR Signal to Noise Ratio

STF Speckle Transfer Function

VTT Vacuum Tower Telescope

Appendix A

Code comparison and performance

The phase recovery is computationally highly expensive. In the course of this work, two different algorithms described in Sect. 2.4.3 were ported to a parallelized ANSI-C code to improve the speed of the reconstruction. With a multiprocessor machine it is possible to reach near real-time image reconstruction. The performance of reconstruction and computational time of the two phase reconstruction algorithms has been evaluated.

Modern scientific cameras achieve frame rates of about 30 frames per second with CCD chip sizes of 2000 by 2000 pixels. When observing speckle burst with these cameras the data rate explodes and can achieve terabytes in one single observing day. Even with relatively cheap storage systems like magnetic tapes this amount of data is not handled easily. Therefore the data is preferably reduced at the telescope requiring fast processing. This was the reason for writing a parallelized computer code to reconstruct large amounts of data as fast as possible. The parallelized ANSI-C computer code was tested with simulated data to compare the convergence properties of the iterative phase reconstruction algorithms. In a second step, the computer code was tested with measured data on different architectures to provide information about the performance of the code in

A. CODE COMPARISON AND PERFORMANCE

different UNIX environments.

A.1 Parallelization

The computer code was parallelized using the Message Passing Interface (MPI) standard (MPI Forum, 1997) for compatibility and performance. This ensures the functionality of the program on various architectures and also enables the program to run on a single processor machine. The parallelization was achieved as follows. One process, called *master* is used to divide and distribute the task to the processors (*slaves*). The flow diagram is presented in Fig. A.1. There are several things that need to be mentioned. Data cubes of subimages are sent twice to the slave. This is necessary to minimize edge effects because of image shifting. The shifting is especially important for the Knox-Thompson phase reconstruction because the cross-spectrum is not shift invariant. Additionally, it can be seen that the Fourier amplitudes are reconstructed using the *master* process. The reason is that, when an adaptive optics is used for the acquisition of the data, the knowledge of the spectral ratios of all subfields is necessary to choose the correct speckle transfer function.

A.2 Convergence properties

In order to compare the convergence properties of the algorithms described in Sect. 2.4.3 in a fair manner, the number of averaged cross- and bispectrum values must be approximately the same. This is controlled by the shift parameters $\vec{\delta}$ in the Knox-Thompson case and \vec{u}, \vec{v} in the triple correlation case. While it is fairly easy to control $\vec{\delta}$ by restricting its length further (equation (2.39)), the control of \vec{u} and \vec{v} is more complicated since a wrong restriction in equation (2.44) could result in an ill-posed problem for the reconstruction because not all spatial frequencies were covered in bad cases. This has been discussed further e.g. by Pehlemann &

A.2 Convergence properties

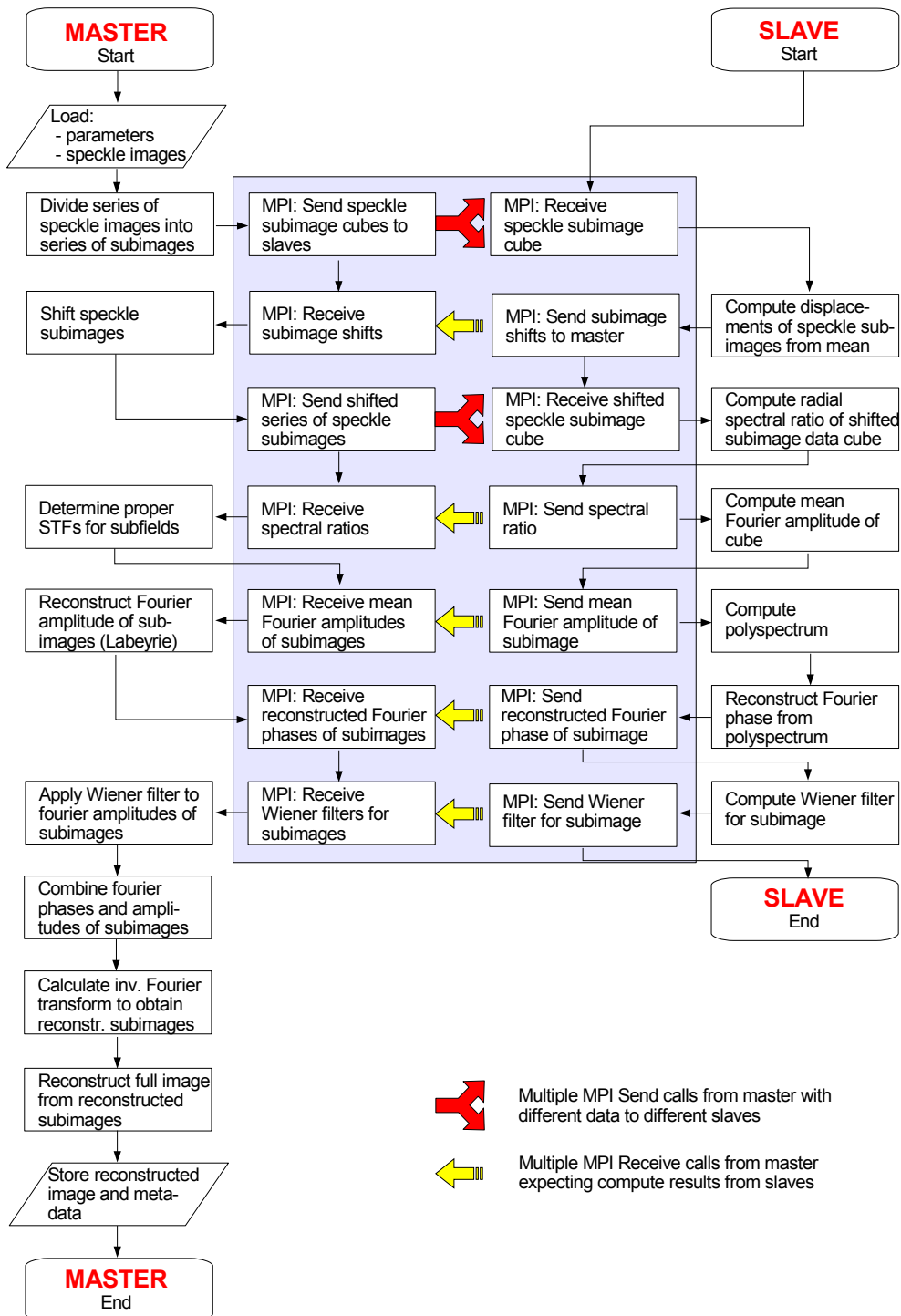


Figure A.1: The flow diagram of the implemented speckle program.

A. CODE COMPARISON AND PERFORMANCE

von der Lühe (1989). In the presented algorithm, the following subset is used:

$$\begin{aligned}
 \hat{\Pi}(a, b, c) = & \{ \vec{u} = (u_x, u_y), \vec{v} = (v_x, v_y) : \\
 & 0 \leq u_x \leq b \quad \wedge \quad -a \leq u_y \leq a \\
 & \wedge u_x \leq v_x \leq a \wedge \left\{ \begin{array}{l} -a \leq v_y \leq a \quad , \text{if } u_x \neq v_x \vee u_y = 0 \\ -a \leq v_y \leq -|u_y| \\ \vee |u_y| \leq v_y \leq a \quad , \text{if } u_x = v_x \wedge u_y \neq 0 \end{array} \right. \quad (A.1) \\
 & \wedge |\vec{v}| \leq a \wedge |\vec{u} + \vec{v}| \leq a \wedge (|\vec{u}| \leq c \vee |\vec{v}| \leq c \vee |\vec{u} + \vec{v}| \leq c) \\
 & \}.
 \end{aligned}$$

The first two major restrictions in the subset $\hat{\Pi}(a, b, c)$ ensure that all spatial frequencies are taken into account and thus can be reconstructed. The third restriction sets the part of bispectrum to be used. A restriction of cross- or bispectrum values greatly improves the reconstruction speed of the algorithm. However, if the restriction is too stringent, there are not enough bispectrum values to compute a reliable phase estimation.

The test environment for the convergence test was a computer cluster consisting in this case of 8 dual AMD Opteron 244 processor nodes. The test data were 4 cubes of 256x256 pixels with 100 images which were artificially distorted by synthetic PSFs corresponding to Fried parameters of $r_0 = 5, 7, 10, 20$ cm. The reconstruction was done within subfields of 128x128 pixels, a size which is commonly used on observational data. After each iteration step the phase within one selected subfield was calculated, and the squared difference from the phase values of the previous iteration step was computed at each frequency point separately. The sum over all frequency points of the squared difference

$$\kappa = \frac{1}{N} \sum_{\vec{f}} (\Phi_n(\vec{f}) - \Phi_{n-1}(\vec{f}))^2, \quad (A.2)$$

where n represents the n -th iteration step and N is the total number of frequency points, is a measure for the convergence speed and is shown as the color coded surface in Fig. A.2. Both algorithms converge the faster the better the atmospheric

A.2 Convergence properties

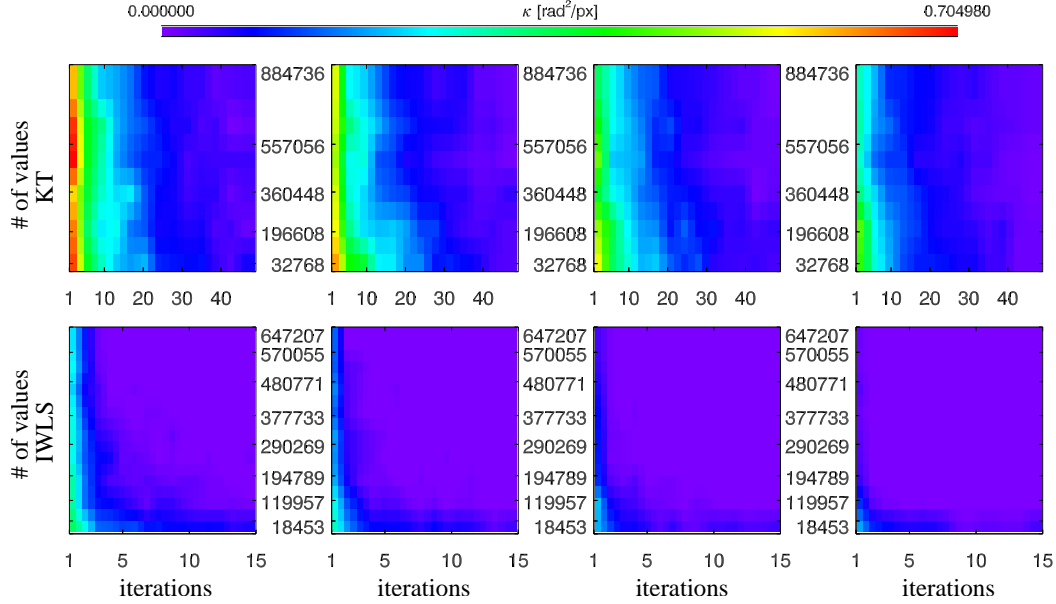


Figure A.2: Convergence properties of the two implemented algorithms. Upper row: Knox-Thompson (KT) algorithm, lower row: Iterative weighted least-squares (IWLS) algorithm. Columns from left to right: $r_0 = 5, 7, 10, 20$ cm. Note that a panel of the IWLS algorithm is a subpanel of a KT panel.

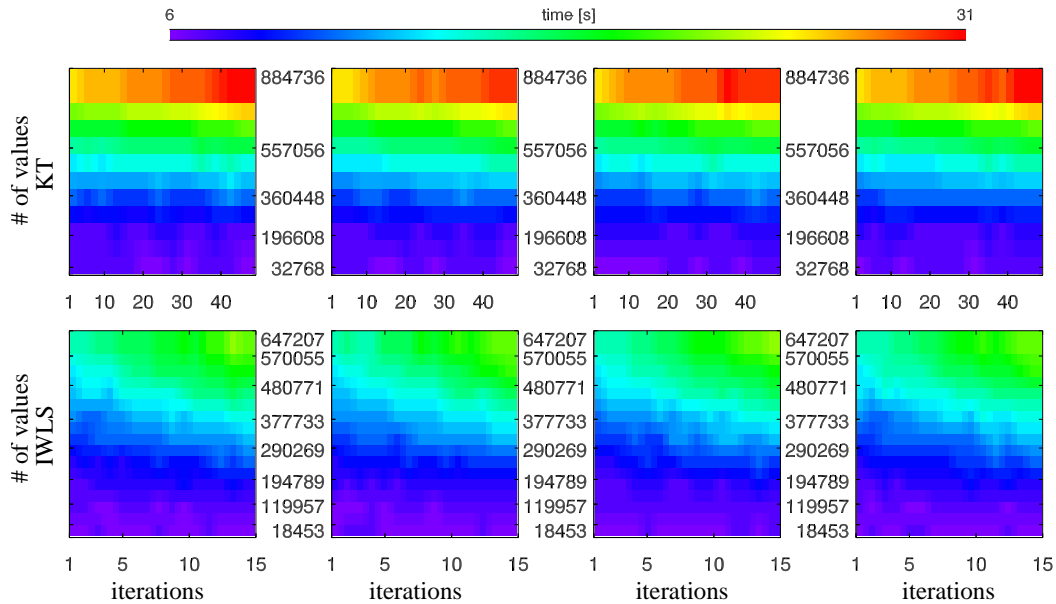


Figure A.3: Time used for one reconstruction using different parameter sets. Upper row: KT algorithm, lower row: IWLS algorithm. The columns are as in in Fig. A.2.

A. CODE COMPARISON AND PERFORMANCE

conditions. The Knox-Thompson algorithm appears to use more iterations and cross-spectrum values to converge to the same squared phase distance value as the iterative weighted least-squares algorithm. One reason for this behavior is that the Knox-Thompson algorithm is currently implemented in a way that it calculates the average cross-spectrum values at *all* frequency positions, i.e. also at frequency positions that lie *beyond* the diffraction limit of the telescope. Because the computation of the average cross- or bi-spectrum is the numerically most costly part of the algorithms, the calculation of unused values slows down the reconstruction process while convergence properties are not improved.

A.2.1 Code performance

In a first step, the time was measured to compute a reconstruction of the synthetic data cubes described in Sect. A.2 using different combinations of cross- or bispectrum values averaged and number of iterations. The result is presented in Fig. A.3. As expected there is no dependence on the Fried parameter this time. It is interesting to see that both algorithms use approximately the same amount of time to compute a reconstruction, with small advantages for the Knox-Thompson algorithm, which is not surprising because it is numerically less complex. However, the difference is small considering the much better convergence properties of the iterative weighted least-squares algorithm described in Sect. A.2. In a second step, the linearity of the computer code with the amount of processors used was tested for two different environments. On the one hand, the code was evaluated on a 8 dual-core processor SUN Sun-Fire V890 machine running SunOS 10. Each processor ran at 1.35 GHz. The machine had 32GB of random access memory (RAM). On the other hand, a Gentoo Linux cluster with 16+1 nodes, each having 2 Opteron 244 with 1.8 GHz, was used for comparison. Each node had 2GB of RAM. In this particular test, the data consisted of a cube of 100 images with 1024x1024 pixels. The result is presented in Fig. A.4.

A.2 Convergence properties

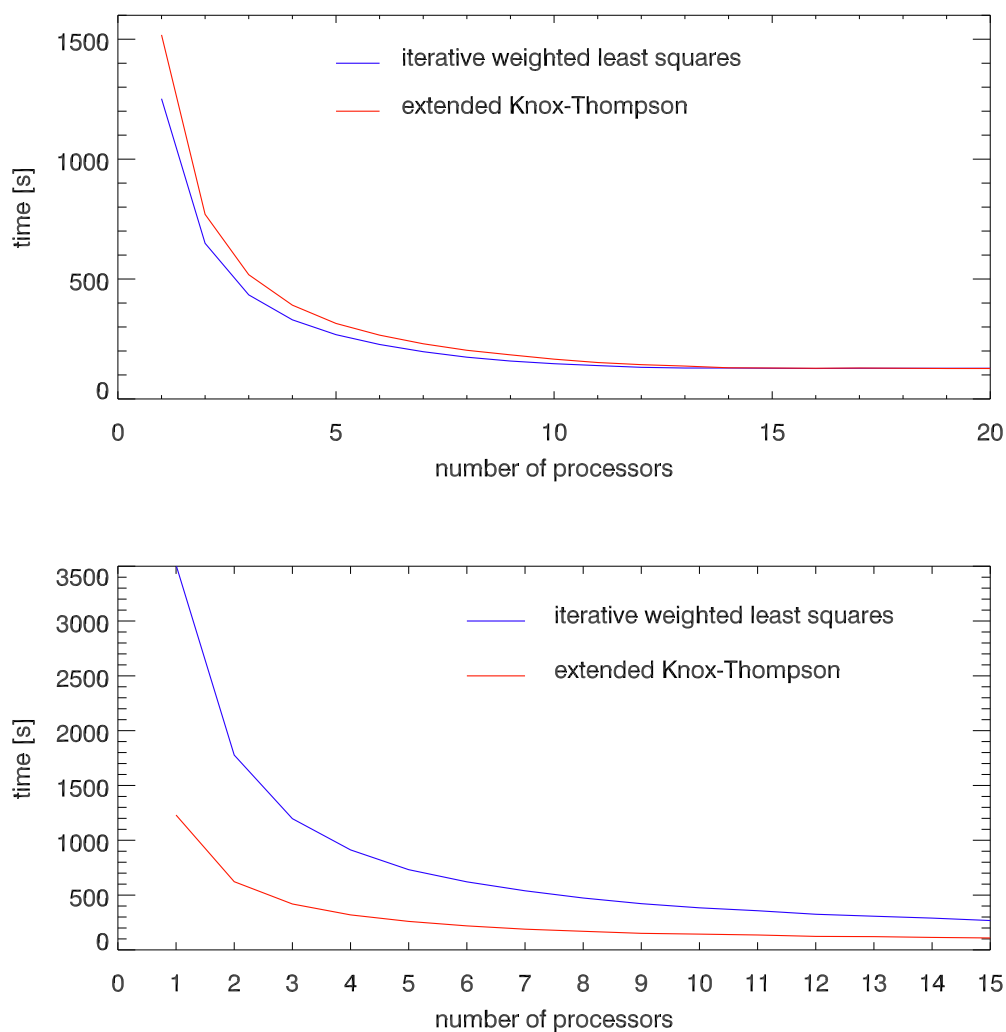


Figure A.4: Time used for one for one reconstruction versus numbers of computation nodes used. Top graphs: Opteron Cluster with Gentoo Linux. Bottom graphs: Sun-Fire V890 machine running SunOS 10. Both, the Knox-Thompson and the triple correlation algorithm, were used with approximately the same number of cross-spectrum (360448) and bispectrum (374190) values for averaging.

A. CODE COMPARISON AND PERFORMANCE

Appendix B

Zernike polynomials

Zernike polynomials form an orthonormal basis on a circle. Here, the definition according to [Noll \(1976\)](#) is given:

$$Z_n^m(r, \alpha) = \sqrt{2(n+1)} \cdot R_n^m(r) \cdot \begin{cases} \cos(m\alpha), & \text{if } m > 0 \\ \sin(m\alpha), & \text{if } m < 0 \end{cases} \quad (\text{B.1})$$
$$Z_n^0(r, \alpha) = \sqrt{(n+1)} \cdot R_n^0(r)$$

where

$$R_n^m(r) = \sum_{l=0}^{(n-m)/2} \frac{(-1)^l (n-l)!}{l! \left(\frac{n+m}{2} - l\right)! \left(\frac{n-m}{2} - l\right)!} r^{n-2l} \quad (\text{B.2})$$

and the conditions for radial order n and azimuthal order m

$$\begin{aligned} n &\in \mathbb{N}, \\ m &\in [-n, n], \text{ and} \\ (n-m) &\equiv 0 \pmod{2} \end{aligned} \quad (\text{B.3})$$

[Noll \(1976\)](#) suggested a new ordering index j , that numbers the modes with increasing m and $|n|$, and the condition, that $j \equiv 0 \pmod{2} \Leftrightarrow m \geq 0$. The lowest modes are presented in [Fig. B.1](#).

B. ZERNIKE POLYNOMIALS

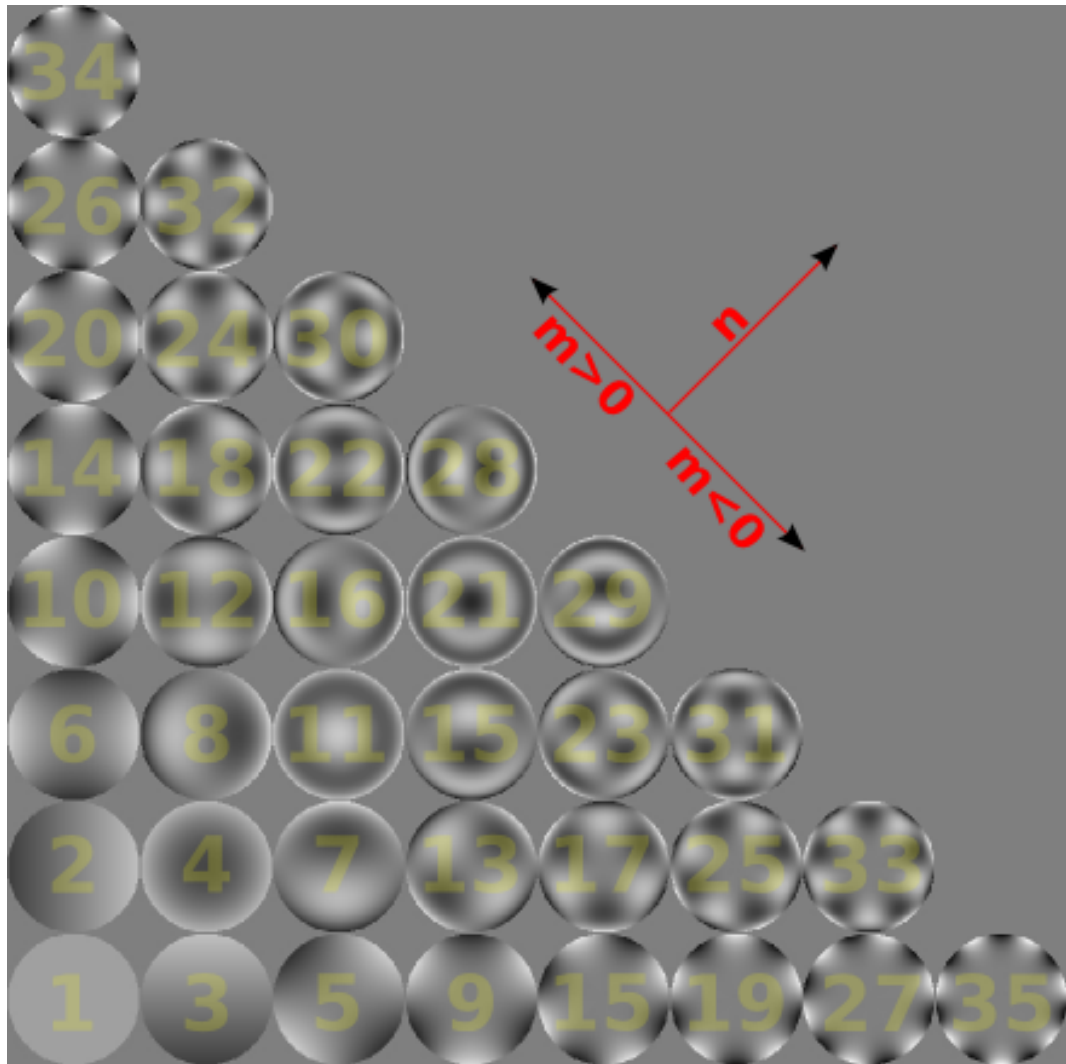


Figure B.1: The lowest Zernike modes. Imprinted in yellow are the indexes according to Noll. The coordinate system symbolizes the radial and azimuthal indexing.

References

- AYERS, G.R., NORTHCOTT, M.J. & DAINTY, J.C. (1988). Knox-Thompson and triple-correlation imaging through atmospheric turbulence. *J. Opt. Soc. Am. A*, **5**, 963–985. [24](#), [25](#)
- BABCOCK, H.W. (1953). The Possibility of Compensating Astronomical Seeing. *Proc. Astron. Soc. Pac.*, **65**, 229–+. [14](#)
- BECKERS, J.M. (1988). Increasing the Size of the Isoplanatic Patch with Multi-conjugate Adaptive Optics. In M.H. Ulrich, ed., *Very Large Telescopes and their Instrumentation, ESO Conference and Workshop Proceedings, Proceedings of a ESO Conference on Very Large Telescopes and their Instrumentation, held in Garching, March 21-24, 1988, Garching: European Southern Observatory (ESO), 1988, edited by Marie-Helene Ulrich., p.693*, 693–+. [15](#)
- BECKERS, J.M. & SCHRÖTER, E.H. (1968). The Intensity, Velocity and Magnetic Structure of a Sunspot Region. I: Observational Technique; Properties of Magnetic Knots. *Solare Physics*, **4**, 142–+. [65](#)
- BERGER, T.E. & TITLE, A.M. (2001). On the Relation of G-Band Bright Points to the Photospheric Magnetic Field. *Astrophysical Journal*, **553**, 449–469. [67](#), [96](#)
- BERGER, T.E., SCHRIJVER, C.J., SHINE, R.A., TARBELL, T.D., TITLE, A.M. & SCHARMER, G. (1995). New Observations of Subarcsecond Photospheric Bright Points. *Astrophysical Journal*, **454**, 531–+. [75](#), [76](#)

REFERENCES

- BERKEFELD, T., SOLTAU, D. & VON DER LÜHE, O. (2006). Multi-conjugate solar adaptive optics with the VTT and GREGOR. In *Proceedings of the SPIE, Volume 6272, pp. 627205 (2006)*. [15](#)
- BONACCINI, D., PRIETO, E., CORPORON, P., LE MIGNANT, D., PRADO, P., GREDEL, R., HUBIN, N. & CHRISTOU, J. (1997). Performance of the ESO AO system, Adonis, at La Silla 3.6 M telescope. In B.S. Dunn, J.D. MacKenzie, E.J. Pope, H.K. Schmidt & M. Yamane, eds., *Conference Paper, SPIE Proceedings, Vol. 3126, p. 589-594*, 589–594. [43](#)
- CARLSSON, M. & STEIN, R.F. (1992). Non-LTE radiating acoustic shocks and CA II K2V bright points. *Astrophysical Journal*, **397**, L59–L62. [64](#), [69](#)
- CARLSSON, M. & STEIN, R.F. (1994). Radiation shock dynamics in the solar chromosphere - results of numerical simulations. In M. Carlsson, ed., *Chromospheric Dynamics*, 47–+. [64](#)
- CARLSSON, M. & STEIN, R.F. (1995). Does a nonmagnetic solar chromosphere exist? *Astrophysical Journal*, **440**, L29–L32. [64](#)
- CARLSSON, M. & STEIN, R.F. (1997). Formation of Solar Calcium H and K Bright Grains. *Astrophysical Journal*, **481**, 500–+. [97](#)
- CARLSSON, M., STEIN, R.F., NORDLUND, Å. & SCHARMER, G.B. (2004). Observational Manifestations of Solar Magnetoconvection: Center-to-Limb Variation. *Astrophysical Journal*, **610**, L137–L140. [67](#)
- CHAPMAN, G.A. & SHEELEY, N.R., JR. (1968). The Photospheric Network. *Solar Physics*, **5**, 442–+. [65](#)
- CHOU, D.Y., SUN, M.T., HUANG, T.Y., JIMENEZ, A., LAI, S.P., CHI, P.J., OU, K.T., WANG, C.C., LU, J.Y., CHU, A.L., NIU, C.S., MU, T.M., CHEN, K.R., CHOU, Y.P., RABELLO-SOARES, M.C., AI, G.X., WANG, G.P., ZIRIN, H., MARQUETTE, W. & NENOW, J. (1995). Taiwan oscillation network. *Solar Physics*, **160**, 237–243. [85](#)

REFERENCES

- CLYNE, J. & RAST, M. (2005). A prototype discovery environment for analyzing and visualizing terascale turbulent fluid flow simulations. In *Proceedings of Visualization and Data Analysis 2005*, 284–294. [91](#)
- DE PONTIEU, B., ERDÉLYI, R. & DE MOORTEL, I. (2005). How to Channel Photospheric Oscillations into the Corona. *Astrophysical Journal*, **624**, L61–L64. [97](#)
- DEROSA, M.L. & TOOMRE, J. (2004). Evolution of Solar Supergranulation. *Astrophysical Journal*, **616**, 1242–1260. [69](#)
- DUNN, R.B. & ZIRKER, J.B. (1973). The Solar Filigree. *Solar Physics*, **33**, 281–+. [65](#)
- FOSSUM, A. & CARLSSON, M. (2005). High-frequency acoustic waves are not sufficient to heat the solar chromosphere. *Nature*, **435**, 919–921. [64](#), [68](#)
- FRIED, D.L. (1966). Optical resolution through a randomly inhomogeneous medium for very long and very short exposures. *J. Opt. Soc. Am.*, **56**, 1372–1379. [13](#), [14](#), [22](#)
- G. MOLODIJ, G.R. (1997). Angular correlation of zernike polynomials for a laser guide star in adaptive optics. *J. Opt. Soc. Am. A*, **14**, 1949–1966. [36](#)
- GOODMAN, J.W. (1985). *Statistical optics*. New York: Wiley, 1985. [13](#)
- GOODMAN, M.L. (2000). On the Mechanism of Chromospheric Network Heating and the Condition for Its Onset in the Sun and Other Solar-Type Stars. *Astrophysical Journal*, **533**, 501–522. [68](#)
- GSL (2006). Gnu scientific library. <http://www.gnu.org/software/gsl/>. [38](#)
- HARDER, S. & CHELLI, A. (2000). Estimating the point spread function of the adaptive optics system ADONIS using the wavefront sensor measurements. *Astronomy and Astrophysics*, **142**, 119–135. [43](#)
- HARDY, J.W., ed. (1998). *Adaptive optics for astronomical telescopes*. [15](#), [16](#), [60](#)

REFERENCES

- HASAN, S.S., VAN BALLEGOIJEN, A.A., KALKOFEN, W. & STEINER, O. (2005). Dynamics of the Solar Magnetic Network: Two-dimensional MHD Simulations. *Astrophysical Journal*, **631**, 1270–1280. [69](#)
- HOLLIS, J.M., DORBAND, J.E. & YUSEF-ZADEH, F. (1992). Comparing restored HST and VLA imagery of R Aquarii. *Astrophysical Journal*, **386**, 293–298. [54](#), [55](#)
- J. Y. WANG, J.K.M. (1978). Modal compensation of atmospheric turbulence phase distortion. *J. Opt. Soc. Am.*, **68**, 78–87. [30](#), [31](#)
- JAIN, A.K. (1989). *Fundamentals of digital image processing*. Prentice Hall Information and System Sciences Series, Englewood Cliffs: Prentice Hall, 1989. [76](#)
- JANSSEN, K. & CAUZZI, G. (2006). Dynamics of the solar photosphere with IBIS. I. Reversed intensity structure in the mid-photosphere. *Astronomy and Astrophysics*, **450**, 365–374. [97](#)
- JEFFERIES, S.M. & CHRISTOU, J.C. (1993). Restoration of Astronomical Images by Iterative Blind Deconvolution. *Astrophysical Journal*, **415**, 862–+. [51](#)
- JEFFERIES, S.M., MCINTOSH, S.W., ARMSTRONG, J.D., BOGDAN, T.J., CACCIANI, A. & FLECK, B. (2006). Magnetoacoustic Portals and the Basal Heating of the Solar Chromosphere. *Astrophysical Journal*, **648**, L151–L155. [65](#), [68](#)
- KHOMENKO, E.V., MARTÍNEZ GONZÁLEZ, M.J., COLLADOS, M., VÖGLER, A., SOLANKI, S.K., RUIZ COBO, B. & BECK, C. (2005). Magnetic flux in the internetwork quiet Sun. *Astronomy and Astrophysics*, **436**, L27–L30. [83](#)
- KNEER, F. & VON UEXKULL, M. (1993). Oscillations of the Sun’s chromosphere. VI. K grains, resonances, and gravity waves. *Astronomy and Astrophysics*, **274**, 584–+. [96](#)
- KNOX, K.T. & THOMPSON, B.J. (1974). Recovery of images from atmospherically degraded short-exposure photographs. *Astrophysical Journal*, **193**, L45–L48. [24](#)

REFERENCES

- KORFF, D. (1973). Analysis of a method for obtaining near-diffraction-limited information in the presence of atmospheric turbulence. *J. Opt. Soc. Am.*, **63**, 971–980. [22](#)
- LABEYRIE, A. (1970). Attainment of Diffraction Limited Resolution in Large Telescopes by Fourier Analysing Speckle Patterns in Star Images. *Astronomy and Astrophysics*, **6**, 85–+. [19](#), [24](#)
- LANGHANS, K., SCHMIDT, W. & RIMMELE, T. (2004). Diagnostic spectroscopy of G-band brightenings in the photosphere of the sun. *Astronomy and Astrophysics*, **423**, 1147–1157. [67](#)
- LEENAARTS, J. & WEDEMEYER-BÖHM, S. (2005). DOT tomography of the solar atmosphere. III. Observations and simulations of reversed granulation. *Astronomy and Astrophysics*, **431**, 687–692. [64](#), [97](#)
- LEIGHTON, R.B., NOYES, R.W. & SIMON, G.W. (1962). Velocity Fields in the Solar Atmosphere. I. Preliminary Report. *Astrophysical Journal*, **135**, 474–+. [65](#), [83](#)
- LEPAGE, G.P. (1978). A new algorithm for adaptive multidimensional integration. *J. Comp. Phys.*, **27**, 192–203. [38](#)
- LIVINGSTON, W. & HARVEY, J. (1969). Observational Evidence for Quantization in Photospheric Magnetic Flux. *Solar Physics*, **10**, 294–+. [65](#)
- LOHMANN, A.W., WEIGELT, G. & WIRNITZER, B. (1983). Speckle masking in astronomy - Triple correlation theory and applications. *Applied Optics*, **22**, 4028–4037. [24](#), [26](#)
- MARSCH, E. (2006). Kinetic Physics of the Solar Corona and Solar Wind. *Living Reviews in Solar Physics*, **3**, 1–+. [3](#)
- MATSON, C.L. (1991). Weighted-least-squares phase reconstruction from the bispectrum. *J. Opt. Soc. Am. A*, **8**, 1905–1913. [27](#)

REFERENCES

- MIKURDA, K. & VON DER LÜHE, O. (2006). High Resolution Solar Speckle Imaging With the Extended Knox Thompson Algorithm. *Solar Physics*, **235**, 31–53. [25](#), [53](#)
- MPI FORUM (1997). The message passing interface standard. <http://www.mpi-forum.org/>. [106](#)
- MULLER, R. & ROUDIER, T. (1984). Variability of the quiet photospheric network. *Solar Physics*, **94**, 33–47. [65](#), [66](#)
- MULLER, R., ROUDIER, T., VIGNEAU, J. & AUFFRET, H. (1994). The proper motion of network bright points and the heating of the solar corona. *Astronomy and Astrophysics*, **283**, 232–240. [67](#)
- NARAYAN, R. & NITYANANDA, R. (1986). Maximum entropy image restoration in astronomy. *Ann. Rev. Astron. Astrophys.*, **24**, 127–170. [54](#)
- NECKEL, H. (1999). Announcement SPECTRAL ATLAS OF SOLAR ABSOLUTE DISK-AVERAGED AND DISK-CENTER INTENSITY FROM 3290 TO 12510 (Brault and Neckel, 1987) NOW AVAILABLE FROM HAMBURG OBSERVATORY ANONYMOUS FTP SITE. *Solar Physics*, **184**, 421. [69](#)
- NIKIAS, C.L. & RAGHUVVEER, M.R. (1987). Bispectrum estimation - A digital signal processing framework. *IEEE Proceedings*, **75**, 869–891. [24](#)
- NOLL, R.J. (1976). Zernike polynomials and atmospheric turbulence. *J. Opt. Soc. Am.*, **66**, 207–211. [30](#), [33](#), [36](#), [43](#), [113](#)
- PARKER, E.N. (1988). Nanoflares and the solar X-ray corona. *Astrophysical Journal*, **330**, 474–479. [68](#)
- PEHLEMANN, E. & VON DER LÜHE, O. (1989). Technical aspects of the speckle masking phase reconstruction algorithm. *Astronomy and Astrophysics*, **216**, 337–346. [106](#)
- PRESS, W.H., TEUKOLSKY, S.A., VETTERLING, W.T. & FLANNERY, B.P. (1992). *Numerical recipes in C. The art of scientific computing*. Cambridge: University Press, —c1992, 2nd ed. [55](#)

REFERENCES

- PUSCHMANN, K.G. & SAILER, M. (2006). Speckle reconstruction of photometric data observed with adaptive optics. *Astronomy and Astrophysics*, **454**, 1011–1019. [29](#)
- RIMMELE, T., RICHARDS, K., ROCHE, J., HEGWER, S. & TRITSCHLER, A. (2006). Progress with solar multi-conjugate adaptive optics at NSO. In *Proceedings of the SPIE, Volume 6272, pp. 627206 (2006)*. [15](#)
- RIMMELE, T.R., RICHARDS, K., HEGWER, S., FLETCHER, S., GREGORY, S., MORETTO, G., DIDKOVSKY, L.V., DENKER, C.J., DOLGUSHIN, A., GOODE, P.R., LANGLOIS, M., MARINO, J. & MARQUETTE, W. (2004). First results from the NSO/NJIT solar adaptive optics system. In S. Fineschi & M.A. Gummin, eds., *Telescopes and Instrumentation for Solar Astrophysics. Edited by Fineschi, Silvano; Gummin, Mark A. Proceedings of the SPIE, Volume 5171, pp. 179-186 (2004)*., 179–186. [16](#)
- RODDIER, F. (1981). The effects of atmospheric turbulence in optical astronomy. In E. Wolf, ed., *Progress in Optics*, 19, 283–376, North-Holland Publishing Company, Amsterdam, Oxford. [13](#), [14](#)
- ROGGEMANN, M.C., ed. (1996). *Imaging through turbulence*. CRC Press. [8](#), [12](#)
- ROGGEMANN, M.C., WELSH, B.M. & FUGATE, R.Q. (1997). Improving the resolution of ground-based telescopes. *Reviews of Modern Physics*, **69**, 437–505. [7](#), [11](#)
- ROUPPE VAN DER VOORT, L.H.M., HANSTEEN, V.H., CARLSSON, M., FOSSUM, A., MARTHINUSSEN, E., VAN NOORT, M.J. & BERGER, T.E. (2005). Solar magnetic elements at 0.1 arcsec resolution. II. Dynamical evolution. *Astronomy and Astrophysics*, **435**, 327–337. [66](#)
- RUTTEN, R.J., DE WIJN, A.G. & SÜTTERLIN, P. (2004). DOT tomography of the solar atmosphere. II. Reversed granulation in Ca II H. *Astronomy and Astrophysics*, **416**, 333–340. [72](#)

REFERENCES

- SÁNCHEZ ALMEIDA, J. (2006). Magnetic flux in the inter-network quiet Sun from comparison with numerical simulations. *Astronomy and Astrophysics*, **450**, 1199–1202. [83](#)
- SCHAFFENBERGER, W., WEDEMEYER-BÖHM, S., STEINER, O. & FREYTAG, B. (2005). Magnetohydrodynamic Simulation from the Convection Zone to the Chromosphere. In D.E. Innes, A. Lagg & S.A. Solanki, eds., *ESA SP-596: Chromospheric and Coronal Magnetic Fields*. [64](#), [83](#)
- SIMON, G.W. & LEIGHTON, R.B. (1964). Velocity Fields in the Solar Atmosphere. III. Large-Scale Motions, the Chromospheric Network, and Magnetic Fields. *Astrophysical Journal*, **140**, 1120–+. [68](#)
- SOCAS-NAVARRO, H. (2005). Are Electric Currents Heating the Magnetic Chromosphere? *Astrophysical Journal*, **633**, L57–L60. [68](#)
- SPRUIT, H.C. (1976). Pressure equilibrium and energy balance of small photospheric fluxtubes. *Solar Physics*, **50**, 269–295. [67](#)
- STEINER, O. (1990). *Ph.D. Thesis*. [77](#), [79](#)
- STEINER, O., GROSSMANN-DOERTH, U., SCHÜSSLER, M. & KNÖLKER, M. (1996). Polarized Radiation Diagnostics of Magnetohydrodynamic Models of the Solar Atmosphere. *Solar Physics*, **164**, 223–242. [66](#)
- STEINER, O., HAUSCHILDT, P.H. & BRULS, J. (2001). Radiative properties of magnetic elements. I. Why are vec G-band bright points bright? *Astronomy and Astrophysics*, **372**, L13–L16. [67](#)
- STIX, M. (2002). *The sun: an introduction*. The sun : an introduction – 2nd ed. /Michael Stix. Berlin : Springer, 2002. QB 521 .S75. [65](#), [69](#), [83](#), [85](#)
- TATARSKII, V.I., ed. (1971). *The effects of the turbulent atmosphere on wave propagation*. Israel Program for Scientific Translations, Jerusalem. [12](#)
- ULMSCHNEIDER, P., RAMMACHER, W., MUSIELAK, Z.E. & KALKOFEN, W. (2005). On the Validity of Acoustically Heated Chromosphere Models. *Astrophysical Journal*, **631**, L155–L158. [64](#), [68](#)

REFERENCES

- VERNAZZA, J.E., AVRETT, E.H. & LOESER, R. (1981). Structure of the solar chromosphere. III - Models of the EUV brightness components of the quiet-sun. *Astrophysical Journal Supplement Series*, **45**, 635–725. [2](#), [3](#), [63](#), [82](#)
- VON DER LÜHE, O. (1984). Estimating fried’s parameter from a time series of an arbitrary resolved object imaged through atmospheric turbulence. *J. Opt. Soc. Am. A*, **1**, 510–519. [23](#)
- VON DER LÜHE, O. (1985). The Speckle Masking Transfer Function. *Astronomy and Astrophysics*, **150**, 229–+. [26](#)
- VON DER LÜHE, O. (1988). Signal Transfer Function of the Knox-Thompson Speckle Imaging Technique. *J. Opt. Soc. Am. A*, **5**, 721–729. [25](#)
- VON DER LÜHE, O., SOLTAU, D., BERKEFELD, T. & SCHELENZ, T. (2003). KAOS: Adaptive optics system for the Vacuum Tower Telescope at Teide Observatory. In S.L. Keil & S.V. Avakyan, eds., *Innovative Telescopes and Instrumentation for Solar Astrophysics. Edited by Stephen L. Keil, Sergey V. Avakyan . Proceedings of the SPIE, Volume 4853, pp. 187-193 (2003).*, 187–193. [16](#)
- WEDEMEYER, S. (2003). PhD Thesis. http://e-diss.uni-kiel.de/diss_764/. [82](#), [97](#)
- WEDEMEYER, S., FREYTAG, B., STEFFEN, M., LUDWIG, H.G. & HOLWEGER, H. (2004). Numerical simulation of the three-dimensional structure and dynamics of the non-magnetic solar chromosphere. *Astronomy and Astrophysics*, **414**, 1121–1137. [64](#), [69](#), [81](#), [82](#), [83](#), [91](#), [95](#), [98](#), [101](#)
- WEIGELT, G.P. (1977). Modified astronomical speckle interferometry ‘speckle masking’. *Optics Communications*, **21**, 55–59. [24](#)
- WEINER, J., DANCHI, W.C., HALE, D.D.S., MCMAHON, J., TOWNES, C.H., MONNIER, J.D. & TUTHILL, P.G. (2000). Precision Measurements of the Diameters of α Orionis and *o* Ceti at 11 Microns. *Astrophysical Journal*, **544**, 1097–1100. [43](#)

REFERENCES

- WIEHR, E. & PUSCHMANN, K.G. (2005). The Size of Small-Scale Solar Magnetic Regions. In D.E. Innes, A. Lagg & S.A. Solanki, eds., *ESA SP-596: Chromospheric and Coronal Magnetic Fields*. 67, 76, 96
- WIEHR, E., BOVELET, B. & HIRZBERGER, J. (2004). Brightness and size of small-scale solar magnetic flux concentrations. *Astronomy and Astrophysics*, 422, L63–L66. 66, 67, 76, 96

Acknowledgements

I am indebted to many people for their support in both professional and personal issues. The first to mention is Prof. Dr. Oskar von der Lühe, giving me the freedom to pursue all research interests while being an understanding advisor and motivator. Many thanks to PD Dr. Wolfgang Schmidt, for many valuable discussions and helpful comments as 'unofficial' advisor.

Special thanks also to Sven Wedemeyer-Böhm, of course, who has told me many, many things about the solar photosphere and chromosphere. Christian Beck, for all his ideas and suggestions about evaluation of observational data (and the cigarettes...). A big thank you to all of the supporting KIS staff, if I could I would name you all!

I would like to thank Markus Sailer in Göttingen for many conversations, be it at the KIS or on Tenerife. Wish you all the best for your future family life!

My stay at the Sacramento Peak Observatory, New Mexico, USA, of the National Solar Observatory (NSO), partially funded by the Association of Universities for Research in Astronomy (AURA) and the KIS, was a great experience. I am indebted to Thomas Rimmele and his family for this wonderful time, and the NSO staff, you know who you are! In addition, I would like to thank Kevin Reardon, Gianna Cauzzi and Katja Janssen for a nice week at the Osservatorio Astrofisico di Arcetri, Florence, Italy.

This thesis would not have been possible without the continuing support of my wife and children, who have been providing me with all the joy needed.